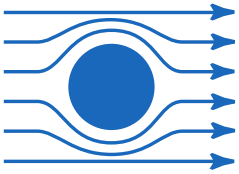

Technische Universität München

Walther-Meißner-Institut für Tief-Temperaturforschung

Bayerische Akademie der Wissenschaften

Coupling Strings, String Networks and Magnon-Phonon Interaction

Master's Thesis by
Thomas Luschmann

Supervisor: Priv.-Doz. Dr. Hans Hübl

Garching, November 2, 2018

Contents

Introduction

Mechanical resonators are ubiquitous in today's world. Aside from well-known, readily available examples like swings, pendulums and musical instruments, mechanical resonators also influence our daily life in ways that are not immediately noticeable or even visible to the human eye. The advances of micro- and nanofabrication in recent decades have allowed the dimensions of mechanical resonators to shrink significantly, leading to a wide range of novel applications in industry and science [1]. Micrometer-sized resonators are used as compact and efficient sensing devices, dubbed MEMS sensors (micro-electromechanical systems), in a variety of consumer electronic devices [2, 3]. Smartphones, for example, rely on MEMS as microphones, altitude sensors and gyroscopes, which detect the rotation of the device [4]. In cars, MEMS are used for electronic stability control, tire-pressure monitoring and navigation systems as well as crash detection and the deployment of air bags [5, 6]. Moreover, MEMS sensors are essential in the advance of the *internet of things* (IoT). They provide the low-cost, low-energy sensors that collect much of the data processed in decentralized wireless sensor networks (WSN) of internet-connected wearables, *smart home* appliances and public infrastructure [7].

The high sensitivity of micromechanical sensors also plays a role in a variety of analytic tools and measurement setups widely used in scientific research. For example, atomic force microscopy (AFM) and surface tunneling microscopy (STM) rely on micromechanical cantilevers, both being essential instruments for the precise investigation of a material's texture, thickness and topography [8, 9]. Similar, cantilever-based techniques have also been used to investigate the dynamics of proteins [10] and manipulate single electronic spins [11]. By further scaling down the dimensions of mechanical resonators to the nanometer-regime, even higher degrees of sensitivity can be achieved. The resulting nanomechanical resonators are often comprised of doubly-clamped strings or tubes fabricated from a tensile stressed material, reaching masses on the order of 10^{-22} kg and resonance frequencies in the MHz to low GHz regime. The systems have been shown to be able to detect the mass of single molecules and atoms attached to the resonators [12, 13], and even higher sensitivities can be reached at low temperatures [14]. Future developments in this direction could eventually lead to the emergence of nanomechanical alternatives in biological or chemical detection, i.e. the precise characterization of trace amounts of substances like drugs or toxins by mass spectroscopy [15, 16].

Additional, interesting fields of research present itself when mechanical modes interact with other degrees of freedom. The integration of mechanical resonators into optical cavities lead to the formation of the field of cavity optomechanics [17], combining the excellent control and readout techniques for optical cavities with the high quality and coherence of mechanical modes. The resulting optomechanical systems allow highly sensitive optical detection of small displacements up to the limit posed by quantum fluctuations [18]. Notably, optomechanical detectors recently gained renewed popular attention for their role in the successful detection of gravitational waves [19], an effort eventually awarded with the Nobel prize in 2017. Apart from sensing applications, optomechanical systems have been employed to manipulate and control mechanical motion using light and vice versa. Thus they have been shown to enable coherent optical wavelength conversion [20] as well as the cooling of mechanical modes to the quantum ground state [21].

Similarly, the integration of mechanical resonators into electronic circuits established the field of circuit electromechanics. In corresponding experiments, nanomechanical resonators are used to modulate the capacitance or inductance of (superconducting) microwave circuits, which in turn can be used to precisely read out the mechanical motion [22, 23]. The interaction of mechanical and electric elements can further be used to control and transfer excitations throughout the circuit, a perk that becomes especially interesting when considering more complex systems including other elements (e.g. qubits) [24, 25]. Furthermore, recent experiments successfully demonstrated quantum phenomena like squeezing [26, 27] and entanglement [28, 29] in mechanical resonators.

Recently, increased attention has been turned towards hybrid systems involving magnetic degrees of freedom. This is due to the fact that magnons, the quantized excitations of magnetization in magnetic materials, offer long lifetimes and good frequency tunability by magnetic fields [30], which are important properties for information carriers. By integrating magnetic insulators with microwave circuits, strong coupling could already be observed between magnons and microwave photons [31–33]. Similarly, light-matter interaction between a magnetic material and optical light was demonstrated, forming the research field of (cavity) optomagnonics [34, 35]. By combining both techniques, magnon-mediated wavelength conversion between microwave and optical frequencies has been realized [36]. Notably, these hybrid systems do not rely on mechanical resonators. However, experiments have demonstrated the introduction of mechanical degrees of freedom into similar systems [37] in order to investigate magneto-mechanical interaction, which will be a subject of this work.

This thesis is divided into two parts:
Part I is dedicated to the investigation of magnetoelastics on a dynamic level, i.e. the coupling between magnonic and phononic degrees of freedom. We build upon successful concepts of cavity optomechanics, in particular *optomechanical crystals* [38], in order to establish a new, nanomechanical platform for the investigation of engineered magnon-phonon coupling. We design and fabricate magneto-mechanical hybrid structures, aiming to couple the magnetization of a magnetic thin film to a nanomechanical resonator and seek to observe the effects of the interaction in ferromagnetic resonance measurements.

In Part II, we investigate the interaction between multiple, high-Q nanomechanical resonators which are mechanically coupled. We design and fabricate strongly coupled multi-resonator systems and demonstrate an all-mechanical protocol for the coherent transfer of phonons between coupled resonators.
Lastly, we conclude the thesis with a brief summary and an outlook on future experimental work and long-term perspectives.

Part I

Magneto-Mechanical Hybrid Systems

Chapter 1

Introduction

In the first part of this thesis, we aim to take essential first steps towards establishing a new platform for the investigation of magnetoelastic interaction on a dynamic level [39, 40]. This engineered magnon-phonon coupling is based on periodic, nanomechanical structures known as phononic crystals [41, 42]. With the emergence of optomechanical crystals [38] in the field of cavity optomechanics [17], it was found that periodicity in nanostructured materials can be exploited to form mechanical analogues to optical Fabry-Perot cavities. These phonon cavities are capable of confining GHz-frequency, high-Q phononic modes to nanomechanical resonators [20, 43, 44]. Here, we attempt to extend the concept of phononic crystals towards magnetic materials and design, fabricate and characterize a magneto-mechanical hybrid structure. As the GHz regime is home to ferromagnetic resonance (FMR) [45] frequencies of most common ferromagnets, localizing mechanical modes of similar frequency in a magnetic material should lead to a strongly enhanced magnetoelastic interaction within the hybrid structure [46, 47]. Ideally, the enhanced interaction should prove strong enough to measurably affect the observed magnetic resonance frequencies.

To this end, we present a theoretical framework for the calculation of acoustic wave propagation in periodic solids in Chapter 2, introducing the concept of *phononic crystals* in the process. We discuss how Finite Element Method (FEM) simulations can be employed to predict a material's elastic properties and how the latter can be deliberately manipulated by careful selection of macroscopic, geometric parameters. Subsequently, we provide a brief overview of the magnetoelastic interaction aimed to observe throughout this part of the thesis. In Chapter 3, we discuss the detailed design process of the fabricated sample structures. In particular, we adapt the established concepts of *phonon cavities* and *phononic shields*, relying on FEM simulations to precisely tailor their elastic properties to our requirements. Chapter 4 is dedicated to a step-by-step summary of the thin film fabrication process employed to produce the previously designed sample structures. Additionally, we show Scanning Electron Microscopy (SEM) images of fabricated samples and evaluate the achieved fidelity to the design. In Chapter 5, we present and discuss first experimental results gathered in broadband ferromagnetic resonance (bbFMR) measurements of two fabricated hybrid structures. Finally, we provide a summary of the findings in Chapter 6.

Chapter 2

Theory

This chapter is dedicated to establish a theoretical framework for the description of mechanical vibrational waves and standing waves in engineered phononic environments. In addition, this chapter provides an introduction to the interaction of said mechanical waves with spin-waves in magnetic materials, called *magnetoelastics*.

2.1 Phononic Crystals

In solid state physics, one commonly refers to a *crystal* as a periodic arrangement of atoms or molecules, repeated throughout a material on a distinct pattern called the *crystal lattice*. By analyzing the periodic potential induced by the crystal's molecules and its effect on electrons propagating through it, insight can be gained into the conductive properties of the crystal and the corresponding material. Similarly, information about the propagation of elastic waves and the dispersion of phonons in the crystal can be gathered (cf. Ref. [48]). It has been found that an arrangement of different macroscopic materials, exhibiting a discrete periodicity through varying dielectric constants, can form an optical analogue, a *photonic crystal*. With carefully constructed designs, photonic crystals allow the control and manipulation of propagating light, including the selective attenuation of desired frequencies (cf. Refs. [49, 50]). Similarly, materials with periodic elastic properties (e.g. density and elasticity) can be constructed in order to control the propagation of acoustic waves through a solid. The resulting structures, called *phononic crystals* [41, 42], offer a wide range of applications from the detection and focusing of sound [51, 52] to the isolation of buildings from external vibrations [53].

In this section, we give an overview of the theoretical background governing the elastic properties of phononic crystals. In particular, we discuss the techniques and equations employed in the numerical calculation of mechanical modes of periodic structures and their visualization as phononic band diagrams. Subsequently, we present a common field of application for phononic crystals, called *bandgap engineering*, detailing how the theoretical knowledge can be applied to engineer materials with very specific elastic properties.
It should be noted that, in the following discussion, we make use of some of the vocabulary and concepts established in the field of *crystallography*, including the *reciprocal space*, *Bloch's theorem*

and the *Brillouin zone*. Since a comprehensive introduction to this field would exceed the scope of this thesis, we refer readers unfamiliar with these concepts to the excellent introductions in solid state physics books such as Refs. [48] or [54].

2.1.1 Phononic Bloch Waves

The propagation of an acoustic wave in a homogeneous medium without body forces is described by the time evolution of the displacement field $\vec{\mathbf{u}}(\vec{\mathbf{x}},t)$, which is given (in component notation) by [55]

$$\rho(\vec{\mathbf{x}})\frac{\partial^2 u_i(\vec{\mathbf{x}},t)}{\partial t^2} = \partial_j[C_{ijmn}(\vec{\mathbf{x}})\partial_n u_m(\vec{\mathbf{x}},t)]. \tag{2.1}$$

The differential equation 2.1 connects the elastic properties of a material, namely the scalar density field $\rho(\vec{\mathbf{x}})$ and the rank 4 elasticity tensor $\mathbf{C}(\vec{\mathbf{x}})$, with the displacement (i.e. the mode shape) $\vec{\mathbf{u}}(\vec{\mathbf{x}},t)$ of an acoustic wave propagating through the material. The indices (i,j,m,n) range up to the number of considered dimensions, i.e. $(i,j,m,n) \in (1,2,3)^4$ and $\vec{\mathbf{u}} = (u_1, u_2, u_3)$ in the three-dimensional case. For the treatment of phononic crystals, we now consider a material system with a discrete, one-dimensional translation symmetry of its elastic properties, i.e. $C_{ijmn}(\vec{\mathbf{x}} + \lambda\vec{\mathbf{a}}) = C_{ijmn}(\vec{\mathbf{x}})$ and $\rho(\vec{\mathbf{x}} + \lambda\vec{\mathbf{a}}) = \rho(\vec{\mathbf{x}})$ for all integer values λ. In other words, the material is periodic along the direction $\vec{\mathbf{a}}$ with periodicity $a = |\vec{\mathbf{a}}|$. Based on this periodicity, Bloch's theorem states that the displacement field can be expressed in the form of a Bloch wave

$$u_i(\vec{\mathbf{x}},t) = e^{ik\vec{\mathbf{x}}}U_i(\vec{\mathbf{x}},t), \tag{2.2}$$

where k is the Bloch wave number and $U_i(\vec{\mathbf{x}},t)$ is a periodic function satisfying [56]

$$U_i(\vec{\mathbf{x}} + \vec{\mathbf{a}},t) = U_i(\vec{\mathbf{x}},t). \tag{2.3}$$

This implies the following relation for the periodicity of the original displacement field

$$u_i(\vec{\mathbf{x}} + \vec{\mathbf{a}},t) = e^{ik(\vec{\mathbf{x}}+\vec{\mathbf{a}})}U_i(\vec{\mathbf{x}},t) = e^{ik\vec{\mathbf{x}}}e^{ik\vec{\mathbf{a}}}U_i(\vec{\mathbf{x}},t) = e^{ik\vec{\mathbf{a}}}u_i(\vec{\mathbf{x}},t). \tag{2.4}$$

Equation 2.4 is known as a Bloch boundary condition. Since the displacement in any position $\vec{\mathbf{x}} + \vec{\mathbf{a}}$ is connected to the displacement at $\vec{\mathbf{x}}$ by a simple phase shift $e^{ik\vec{\mathbf{a}}}$, calculating $\vec{\mathbf{u}}(\vec{\mathbf{x}},t)$ for a *unit cell* of the structure (i.e. for all $|\vec{\mathbf{x}} \cdot \hat{\mathbf{a}}| < a$) with respect to the Bloch boundary condition results in a complete description of the displacement field for all positions $\vec{\mathbf{x}}$. To this end, we rewrite Eq. 2.1 using Eq. 2.2 to [56]

$$\rho(\vec{\mathbf{x}})\frac{\partial^2 U_i(\vec{\mathbf{x}},t)}{\partial t^2} = ik_j S_{ij}(\vec{\mathbf{x}},t) + \partial_j S_{ij}(\vec{\mathbf{x}},t), \tag{2.5}$$

where we defined the reduced stress tensor $S_{ij}(\vec{\mathbf{x}},t)$:

$$S_{ij}(\vec{\mathbf{x}},t) = C_{ijmn}(x)[ik_n U_m(\vec{\mathbf{x}},t) + \partial_n U_m(\vec{\mathbf{x}},t)]. \tag{2.6}$$

The set of differential equations presented by Eq. 2.5 can be discretized and solved numerically for solutions of $U_i(\vec{\mathbf{x}},t)$, classified by the wave number k. However, to further simplify the calculation

we make use of another property of Bloch waves: Solutions that differ in k by integer multiples of the *reciprocal lattice vector* $\vec{\mathbf{b}} = (2\pi/a)\hat{\mathbf{a}}$ are identical. This can also be seen in Eq. 2.4 when considering the phase shift between adjacent cells, since $e^{i(k+\vec{\mathbf{b}})\vec{\mathbf{a}}} = e^{ik\vec{\mathbf{a}}}$ by definition of $\vec{\mathbf{b}}$. As such, it is sufficient to consider a range of k between $-\pi/a$ and π/a, which is called the *Brillouin zone*. In fact, by using time-reversal symmetry, one can even further reduce the discussion to the *irreducible Brillouin zone*, spanning $0 \leq k \leq \pi/a$, which is typically labeled by symmetry points Γ ($k = 0$) and X ($k = \pi/a$).

In summary, one chooses a wave number $0 \leq k \leq \pi/a$ and numerically calculates the time-dependent displacement field of the unit cell $\vec{\mathbf{u}}(\vec{\mathbf{x}},t)$ from Eq. 2.5 with respect to the Bloch boundary conditions Eq. 2.4. Subsequently, the mechanical eigenfrequencies ν_n of the structure can be obtained by a discrete Fourier transformation of the displacement field. Repeating this calculation for various k within the irreducible Brillouin zone results in a phononic band diagram of the structure. For the band diagrams shown throughout this thesis, this process is performed by a Finite Element Method (FEM) solver, which divides a model of the unit cell of the structure into a finite number of *nodes* and solves the necessary differential equations at these discrete points.

Note that this procedure can easily be expanded to structures with higher degrees of symmetry (i.e. periodicity along more than one direction). In this case, the wave number classifying the solutions becomes a wave vector $\vec{\mathbf{k}} = (k_x, k_y, k_z)$ and the irreducible Brillouin zone becomes more complex, leading to the introduction of additional symmetry points. For example, in the case of a two-dimensional rectangular lattice with periodicity a, the irreducible Brillouin zone is spanned by $0 \leq k_x \leq \pi/a$ and $0 \leq k_y \leq k_x$, introducing the new symmetry point M ($k_x = k_y = \pi/a$). For further information and alternative approaches regarding the calculation of acoustic waves in periodic structures, please refer to Refs. [55, 57, 58] and [59], with the latter focusing on the practical application of FEM simulations.

2.1.2 Bandgap Engineering and Localization

Having established suitable tools to simulate acoustic waves in periodically structured solids, we now want to discuss how this knowledge can be employed in order to design materials with specific elastic properties. A goal commonly pursued in the design of phononic crystals is the fabrication of materials with a *phononic band gap* [60–62], i.e. a range of frequencies for which no eigenmodes of the system exist for any wave vector $\vec{\mathbf{k}}$. A simple, classical model exhibiting a phononic bandgap is a one-dimensional, linear chain comprised of alternating small and large masses, which are coupled by springs. Such model systems are commonly studied in solid-state physics lectures in the context of crystal lattices with a diatomic basis [48, 54]. An illustration of the model along with its phononic band structure is shown in Fig. 2.1a and a sketch of the analytic calculation of the phononic dispersion relation can be found in App. A.3. Clearly, we observe a wide gap in the frequency spectrum between the two possible vibrational modes of the linear chain. A detailed examination of the mode shapes reveals that the low-frequency *acoustic* band corresponds to a motion that is primarily carried out by the large masses M, while

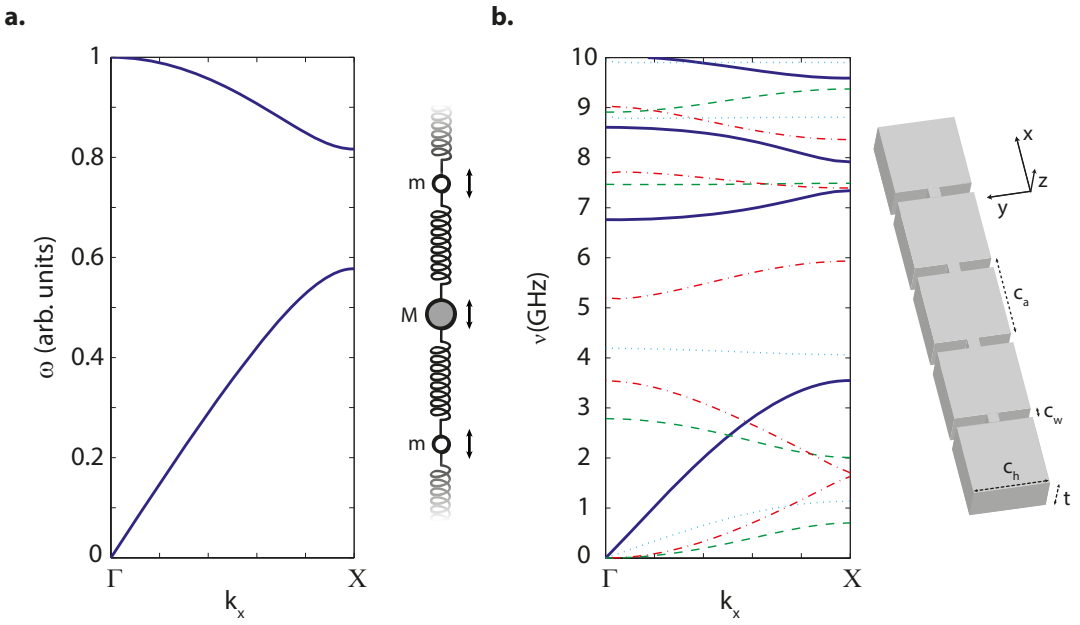

Figure 2.1: Phononic band diagram for **a.** a simple spring-mass system and **b.** its nanomechanical analogue realized with the quasi-1D phononic crystal chain shown on the far right. The crystal's bands were simulated for a silicon structure with dimensions of $(c_a, c_h, c_w, t) = (500, 400, 100, 200)$ nm and are drawn according to the symmetry of the mode. (——), (·····), (- - -) and (-·-·-) correspond to modes with (σ_y,σ_z) symmetry of (+,+), (−,−), (−,+) and (+,−) respectively, where σ_y denotes mirror plane symmetry about the y-axis and σ_z denotes mirror plane symmetry about the z-axis. The figure is adapted from Ref. [60].

the displacement of the high-frequency *optical* mode predominantly affects the small masses m. Furthermore, it can be shown that an increased discrepancy between the masses M and m leads to an enlargement of the frequency bandgap.

Notably, it was found that the properties of this *masses-and-springs* model can be reproduced in a periodic, nanomechanical structure. Fig. 2.1b shows the realization of a quasi-1D (i.e. infinitely periodic only in x-direction) phononic crystal chain, consisting of a series of nanometer-sized *squares*, connected by narrow *bridges*, along with a FEM simulation of its phononic band structure. Notably, as the crystal, unlike the spring model, is in fact a three-dimensional body, significantly more modes result from the simulation. However, the bands can be distinguished by symmetry arguments. When considering only modes with mirror plane symmetry about the y- and z-axis (solid blue bands), we observe the formation of a similar, several GHz wide bandgap between the two lower eigenmodes. Importantly, only a negligible amount of energy is coupled between modes of alternate symmetry. Therefore, for the propagation of a mechanical mode with a certain symmetry, the bands of other symmetries can in fact be neglected for the general discussion of a phononic bandgap. Note that while the phononic band structure of the crystal is similar to the spring model, the actual mode

shapes exhibited by the crystal are much more complex and can not be straightforwardly compared. For a detailed simulation and discussion of the individual mode shapes, please refer to Ref. [60]. Lastly, it has been shown that the eigenfrequencies of the lower bands depend strongly on the size of the connecting *bridges*, c_w, while the high-frequency bands are almost entirely determined by the internal resonances of the *squares*. As such, the position of high- and low-frequency bands can be adjusted almost independently of each other by altering the geometry, offering high control over the bandgap size and position over ranges of several GHz [60].

When an acoustic wave encounters a structure with a frequency inside the latter's bandgap, it will be assigned a complex wave number k, leading to an exponential decay of the wave's displacement as it propagates through the material (since $e^{ik\vec{\mathbf{x}}}$ in Eq. 2.2 gains a real component). Therefore, materials exhibiting a phononic bandgap can be used as frequency dependent *mirrors* for acoustic waves (phonons), exhibiting large reflection coefficients for frequencies within the bandgap. Potential applications are not only related to the isolation of measurements against external vibrations, but also the confinement or *localization* of phonons of certain frequencies to an area surrounded by the phononic crystal (cf. e.g. Refs. [38, 63, 64]), with the latter essentially representing the mechanical analogue to an optical Fabry-Perot cavity. We will discuss two specific applications of bandgap-engineered phononic crystal as *phonon cavities* and *phononic shields* in the context of our simulations in Sec. 3.

2.2 Magnetoelastics

While a large part of this thesis is focused on the description and precise engineering of elastic properties of hybrid-nanostructures, the long term goal is the investigation of *magnetoelastic interaction* between the mechanical and magnetic degrees of freedom within the fabricated samples. To this end, we want to dedicate this section to an introduction to the field of magnetoelastics, providing basic definitions, an overview of research applications and an evaluation of the expected effects on ferromagnetic resonance (FMR) measurements.

2.2.1 Fundamentals

Magnetoelasticity describes the reciprocal dependency between the elastic stress of a ferromagnetic material and its magnetization [39, 40], enabling an alternative method of control of the latter without requiring the generation of magnetic fields [65, 66]. In particular, a periodic elastic deformation (i.e. a mechanical oscillation) affects the magnetic anisotropy throughout a material, which leads to an effective torque acting on the magnetization of the system. The underlying spin-mechanical interaction can be understood as the coupling between spin waves (magnons) and elastic waves (phonons) present in the material. According to theory, the strength of the coupling is enhanced if the magnons and phonons exist at similar frequencies (usually few MHz to GHz) [46, 47]. The magnetoelastic interaction has been used in a variety of experiments from strain sensing [67] to phonon-driven ferromagnetic resonance (FMR) [68] and the creation of spin-polarized electrical currents [69, 70]. Furthermore, the reverse application of the interaction, called *magnetostriction* [39], also constitutes an active field of study. The effect can be used to

manipulate a material's elastic properties by controlling its magnetization, e.g. by applying an external magnetic field. For example, it has been demonstrated that magnetic thin films can be precisely investigated using nanomechanical resonators by exploiting the magnetostrictive properties of the material [71, 72].
In the following, we proceed with a compact overview of the equations describing the effects of magnetoelastic interaction in order develop an understanding of how magnon-phonon coupling could be observed in the sample structures of this thesis. For a more in-depth, theoretical treatment of the subject please refer to Refs. [39, 46, 47].

Since we only consider magnetic films with thicknesses below 50 nm throughout this thesis (see Chap. 3), we begin with the expression for the magnetic free energy density F^0 of a thin magnetic film (extended in x- and y-direction), exposed to an external magnetic field $\vec{\mathbf{H}}_0$ [39]

$$F^0(\vec{\mathbf{m}}) = -\mu_0 \vec{\mathbf{H}}_0 \cdot \vec{\mathbf{m}} + B_\mathrm{d} m_z^2 + B_\mathrm{u} (\vec{\mathbf{u}} \cdot \vec{\mathbf{m}})^2 + \mathrm{const}, \tag{2.7}$$

using the magnetization vector normalized to the saturation magnetization $\vec{\mathbf{m}} = \vec{\mathbf{M}}/M_\mathrm{s} = (m_x, m_y, m_z)$. Further, μ_0 is the vaccuum permeability, $B_\mathrm{d} = \mu_0 M_\mathrm{s}/2$ describes the shape anisotropy and B_u is the uniaxial in-plane anisotropy along $\vec{\mathbf{u}} = (u_x, u_y, 0)$. In a static equilibrium scenario, the magnetization $\vec{\mathbf{m}}$ will align itself towards the most energetically favorable state, i.e. the minimum of F^0. A mechanical oscillation will introduce a time-dependent strain $\varepsilon(t)$ to the material, which we assume to act only along the x-direction for simplicity (i.e. $\varepsilon(t) \parallel \hat{\mathbf{x}}$). The strain contributes to the magnetic free energy due to magnetoelastic coupling [39] according to

$$F^\mathrm{elas}(\vec{\mathbf{m}}, t) = B_1 \varepsilon(t) m_x^2 + \mathrm{const}, \tag{2.8}$$

proportional to the magnetoelastic coupling constant B_1.
The change in the free magnetic energy density can now be expressed as an effective magnetic field

$$\vec{\mathbf{H}}_\mathrm{eff}(t) = -\nabla_{\vec{\mathbf{m}}} F = -\nabla_{\vec{\mathbf{m}}} \Big(F^0 + F^\mathrm{elas}(t) \Big), \tag{2.9}$$

acting on the magnetization vector $\vec{\mathbf{m}}$ evaluated at its equilibrium position [73]. This result tells us that for a finite coupling constant B_1 the effective magnetic field gains an oscillatory component $\vec{\mathbf{H}}_\mathrm{elas}(t) = -\nabla_{\vec{\mathbf{m}}} F^\mathrm{elas}(t))$ due to the time-dependent strain $\varepsilon(t)$.
However, at this point, we will neglect the explicit time-dependence of $\varepsilon(t)$ and instead consider the effect of an averaged strain $\varepsilon_x = \langle \varepsilon(t) \rangle$. This simplifies the following discussion since $\vec{\mathbf{H}}_\mathrm{elas}$ is now constant in time. We can consequently rewrite the time-independent effective field to

$$\vec{\mathbf{H}}_\mathrm{eff} = \vec{\mathbf{H}}_0 + \vec{\mathbf{H}}_\mathrm{aniso} + \vec{\mathbf{H}}_\mathrm{elas}, \tag{2.10}$$

where we introduced a virtual anisotropy field $\vec{\mathbf{H}}_\mathrm{aniso}$ to encapsulate the contributions to Eq. 2.7, which are independent of the real, externally applied field $\vec{\mathbf{H}}_0$. Note that $\vec{\mathbf{H}}_\mathrm{eff}$ corresponds to a minimization of the magnetic free energy, so that the magnetization will strive to align itself along its orientation, i.e. $\vec{\mathbf{m}} \parallel \vec{\mathbf{H}}_\mathrm{eff}$ in equilibrium. Therefore, the effective magnetic field crucially influences the magnetization dynamics of the investigated system. In particular,

the time-evolution of $\vec{\mathbf{m}}$ is governed by its classical equation of motion, known as the Landau-Lifshitz-Gilbert (LLG) equation [74, 75]:

$$\partial_t \vec{\mathbf{m}} = -\gamma \vec{\mathbf{m}} \times \mu_0 \vec{\mathbf{H}}_{\text{eff}} + \alpha \vec{\mathbf{m}} \times \partial_t \vec{\mathbf{m}} \tag{2.11}$$

Here, α is a phenomenological damping parameter and $\gamma = g\mu_B/\hbar$ is the gyromagnetic ratio with the Landé-factor g, the Bohr magneton μ_B and the reduced Planck constant $\hbar$.

By solving Eq. 2.11, one finds that $\vec{\mathbf{m}}$ performs a precessional motion around $\vec{\mathbf{H}}_{\text{eff}}$ with the angular frequency

$$\omega_{\text{res}} = \gamma \mu_0 \left| \vec{\mathbf{H}}_{\text{eff}} \right|. \tag{2.12}$$

Notably, a study of the precession frequency ω_{res} for different magnetic fields $\vec{\mathbf{H}}_0$ can provide information about the magnetic properties (e.g. the anisotropy and damping) of the investigated material. A common approach to the quantitative investigation of ω_{res} are ferromagnetic resonance (FMR) measurements [45], a concept which we will now introduce.

2.2.2 Ferromagnetic Resonance (FMR)

In the following, we discuss the fundamental principles of FMR and subsequently assess the influence of magnetoelastic coupling on the observed resonance frequency. FMR measurements probe the resonant absorption of electromagnetic waves in a magnetic material. In the presence of an external magnetic field $\vec{\mathbf{H}}_0$, the material's magnetization $\vec{\mathbf{M}}$ precesses around a corresponding effective field $\vec{\mathbf{H}}_{\text{eff}}$, as described by Eq. 2.11 and illustrated in Fig. 2.2a.

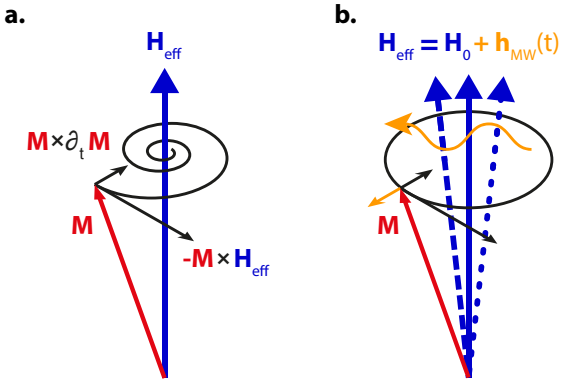

Figure 2.2: Schematic illustration of the basic working principle of ferromagnetic resonance (FMR). **a.** The magnetization $\vec{\mathbf{M}}$ precesses around an effective magnetic field $\vec{\mathbf{H}}_{\text{eff}}$ with frequency ω_{res}. Due to damping effects, $\vec{\mathbf{M}}$ will eventually cease precession and align itself along $\vec{\mathbf{H}}_{\text{eff}}$. **b.** The external microwave field $\vec{\mathbf{h}}_{\text{MW}}(t)$ alters the effective field acting on the magnetization. In the case of ferromagnetic resonance, i.e. $\omega_{\text{MW}} = \omega_{res}$, the damping is compensated by the microwave field (see orange arrow), which is partly absorbed in the process. Thus, a resonance signature is visible in the microwave transmission spectrum. The figure is adapted from Ref. [76].

In FMR measurements, an additional, oscillating magnetic field $\vec{\mathbf{h}}_{\text{MW}}(t)$ is introduced per-

pendicular to $\vec{\mathbf{H}}_0$, generated by a microwave signal passing through a conductor close to the investigated structure. The origin of the resonant absorption is the interaction of the oscillating field with the precessing magnetization, as is illustrated in Fig. 2.2b. In particular, the oscillating field counteracts the damping of the precession (see orange arrow). If the precession frequency of $\vec{\mathbf{M}}$, ω_{res} (cf. Eq. 2.12), and the frequency of the driving field ω_{MW} are brought on resonance, the microwave field compensates the damping of the precessional motion completely and an increased absorption of the microwave signal can be observed in the transmission spectrum.

Notably, due to the addition of the oscillating magnetic field, $\vec{\mathbf{H}}_{\text{eff}}$ becomes more complex. In order to derive a corresponding solution for the ferromagnetic resonance frequency, we assume an orientation of the magnetic field along the x-axis, i.e. $\vec{\mathbf{H}}_0 = H_0\hat{\mathbf{x}}$, and split the expressions for $\vec{\mathbf{H}}_{\text{eff}}$ and m into static and time-dependant parts:

$$\vec{\mathbf{H}}_{\text{eff}}(t) = \vec{\mathbf{H}}_{\text{stat}} + \vec{\mathbf{h}}_{\text{MW}}(t) = (H_0 + H_{\text{aniso}} + H_{\text{elas}})\hat{\mathbf{x}} + \vec{\mathbf{h}}_{\text{MW}}(t) \tag{2.13}$$

$$\vec{\mathbf{m}} = \frac{\vec{\mathbf{M}}_0}{M_{\text{sat}}} + \vec{\mathbf{m}}(t) \tag{2.14}$$

Furthermore, we assume harmonic time-dependencies of the form $\vec{\mathbf{h}}_{\text{MW}}(t) = \vec{\mathbf{h}}_{\text{MW},0} \cdot e^{i\omega t}$ and $\vec{\mathbf{m}}(t) = \vec{\mathbf{m}}_0 \cdot e^{i\omega t}$.
Inserting these expressions into Eq. 2.11 and solving[1] the differential equation for the FMR frequency $f_{\text{FMR}} = \omega/2\pi$ results in the solution [77]

$$f_{\text{FMR}} = \frac{\gamma}{2\pi}\mu_0 \sqrt{(H_0 + H_{\text{aniso}} + H_{\text{elas}} + (N_x - N_z)M_{\text{sat}}) \cdot (H_0 + H_{\text{aniso}} + H_{\text{elas}} + (N_y - N_z)M_{\text{sat}})}, \tag{2.15}$$

which is known as the Kittel equation[2]. Here, $N_{x,y,z}$ are demagnetization factors that depend on the geometry of the investigated sample with respect to the applied magnetic field. In a thin film, they lead to a distinction between two specific cases. For a magnetic field oriented normal to the sample plane, $N_x = N_y = 0$ and $N_z = 1$, resulting in the out-of-plane Kittel equation:

$$f_{\text{FMR}}^{\text{oop}} = \frac{\gamma}{2\pi}\mu_0(H_0 + M_{\text{sat}} - H_{\text{aniso}} - H_{\text{elas}}) \tag{2.16}$$

Conversely, for a magnetic field pointing along the plane of the thin film, $N_z = N_y = 0$ and $N_x = 1$. Thus, we obtain the in-plane variant of the equation:

$$f_{\text{FMR}}^{\text{ip}} = \frac{\gamma}{2\pi}\mu_0 \sqrt{(H_0 + H_{\text{aniso}} + H_{\text{elas}}) \cdot (H_0 + H_{\text{aniso}} + H_{\text{elas}} + M_{\text{sat}})} \tag{2.17}$$

The Kittel equations describe the dispersion of the FMR frequency, i.e. its dependence on the externally applied magnetic field. Therefore, the experimentally observed dispersion in FMR measurements can be fitted with the corresponding equation in order to quantitatively analyze the data, which we will use in Chap. 5. However, the fitting process can not distinguish between

[1] Here, we do not provide a detailed calculation of the equation. For a more thorough derivation, please refer to Refs. [77–79].

[2] Note that the original Kittel equation does not explicitly consider elastic contributions H_{elas}. However, as they correspond to a simple addition to the effective field, they can be easily incorporated.

H_{aniso} and H_{elas}, as they are summarized. Therefore, the magnetoelastic contribution can not be individually extracted. Nonetheless, Eq. 2.15 clearly shows that the strain ε induced by a mechanical oscillation of the material will affect the resonance frequency f_{FMR}. Therefore, it should be possible to observe the influence of magnon-phonon coupling in conventional FMR measurements, as long as the magnetoelastic coupling is sufficiently strong. In particular, the investigation of engineered materials exhibiting a complete phononic bandgap (see Sec. 2.1.2) appears intriguing. Due to the wide tunability of the FMR frequency with the external magnetic field, the dispersion of the FMR mode could be investigated at frequencies within the bandgap of the material, where no resonant magnon-phonon coupling can occur, and subsequently compared to the dispersion at frequencies outside of the bandgap.

Chapter 3

Simulations and Sample Design

This section is dedicated to a detailed description of the design process which the samples fabricated in the scope of this thesis underwent. We use Finite Element Method (FEM) simulations to first recreate geometries of phononic crystals, which were previously published in the field of optomechanics, and adapt them to our material system and evaluate the suitability for our project. Subsequently, we introduce magnetic materials to the structures, forming a double-layer system intended to investigate magnetoelastic interaction and simulate the mechanical properties of the altered crystal. For additional information regarding FEM simulations of acoustic waves, we recommend Ref. [59]. All simulations in this thesis are performed using the FEM solver software *Comsol Multiphysics* [80].

3.1 Zipper Resonators

We commence by introducing the design of a "zipper"-type *optomechanical crystal* or *zipper resonator*, a design popular in the field of optomechanics [17] for its ability to simultaneously localize GHz-frequency elastic waves (phonons) and photons in the THz regime (cf. e.g. Refs. [20, 38, 43, 44]). Since we intend to investigate magnetoelastic interaction, we all but neglect the optical properties and focus our discussion on the localization of GHz-frequency phonons. An illustration of a typical zipper resonator design is shown in Fig. 3.1. It consists of a nanomechanical

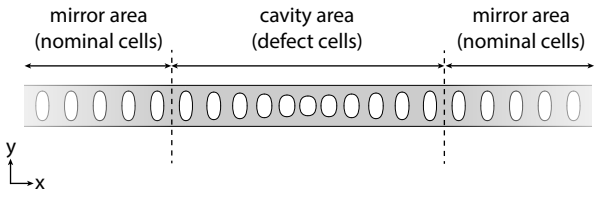

Figure 3.1: Schematic illustration of a typical zipper resonator geometry in top-down view. The resonator consists of a freely suspended nanomechanical string, perforated by elliptic holes. The *mirror areas* extend beyond the boundaries of the illustration and form a perfectly periodic phononic crystal. They act as mirrors for acoustic waves of certain frequencies, confining them to the *cavity area* of different geometry in the center of the string.

string, which is periodically perforated by holes, generating the discrete periodicity of elastic properties necessary to create a phononic crystal with a phononic bandgap (as introduced in Sec. 2.1.2). The perfect one-dimensional periodicity is interrupted in the center of the string by a *defect-* or *cavity area* of altered geometry. If the mechanical eigenmodes of the defect area are successfully matched to the bandgap of the surrounding phononic crystal, the latter forms a *mirror area* reflecting and confining acoustic waves to the *cavity*. In order to achieve this state, the geometry of the string, the holes and the defect has to be carefully chosen. In the following, we will detail the design process of a zipper resonator, using FEM simulations in order to determine the ideal geometry for the localization of phonons in a frequency range comparable to magnonic resonance frequencies (i.e. several GHz).

3.1.1 Phonon Localization

At the beginning of the design process, we will focus on creating a fully periodic crystal (i.e. the mirror area) which exhibits a wide phononic bandgap at suitable frequencies and neglect the defect area for the time being. As discussed in Sec. 2.1.1, when dealing with periodic materials, it is possible to make statements about the elastic properties of an extended structure by only considering its *unit cell*, i.e. the largest, non-redundant building block that can form the actual body when repeated sufficiently. Therefore, in order to simulate the elastic properties of our mirror area, we treat it as a quasi one-dimensional, infinitely periodic repetition (projection) of a rectangular unit cell with length a, width w and thickness t, which is perforated by an elliptic hole spanned by h_x and h_y. A 3D model of such a unit cell is illustrated in Fig. 3.2a, with the dimensions $(a, w, h_\mathrm{x}, h_\mathrm{y}, t)_\mathrm{nominal} = (350, 500, 360, 160, 90)$ nm and periodicity along the x-axis. The chosen geometric parameters are loosely based on Refs. [44, 64], but have been altered in order to produce similar results in a material system of 90 nm thick Si_3N_4 .

As discussed in Sec. 2.1.1, the possible mechanical modes of the structure can now be gathered using a FEM simulation of the unit cell by defining periodic Bloch boundary conditions as in Eq. 2.4. The periodicity further allows us to invoke Bloch's Theorem and classify all of the solutions by a wave number k_x in the irreducible Brillouin zone, $\Gamma = 0 \leq k_x \leq \frac{\pi}{a} = X$, and a band index n. Thus, we can fully describe the system's mechanical modes by its phononic band structure. The resulting band diagram for the zipper unit cell is plotted in Fig. 3.2c, where every band represents one discrete eigenfrequency of the infinitely periodic structure, each continuous in the wave number k_x. Due to the plane symmetry of the unit cell about the $z = 0$ and $y = 0$ planes, the eigenmodes can be further distinguished based on their vector symmetry regarding these planes. To this end, bands with a positive y-z-symmetry are highlighted in red. The mode symmetry becomes significant because it has been shown [38, 43], that, in an ideal scenario, the mode-mode coupling between bands of different symmetry is negligible, resulting in an effective- or *quasi-bandgap* of more than 2.6 GHz for y-z-symmetric modes in the investigated structure (light orange area).

So far, the simulations show that the projection of the investigated unit cell can exhibit GHz frequency oscillations and form a phononic bandgap, but no localization is yet achieved.

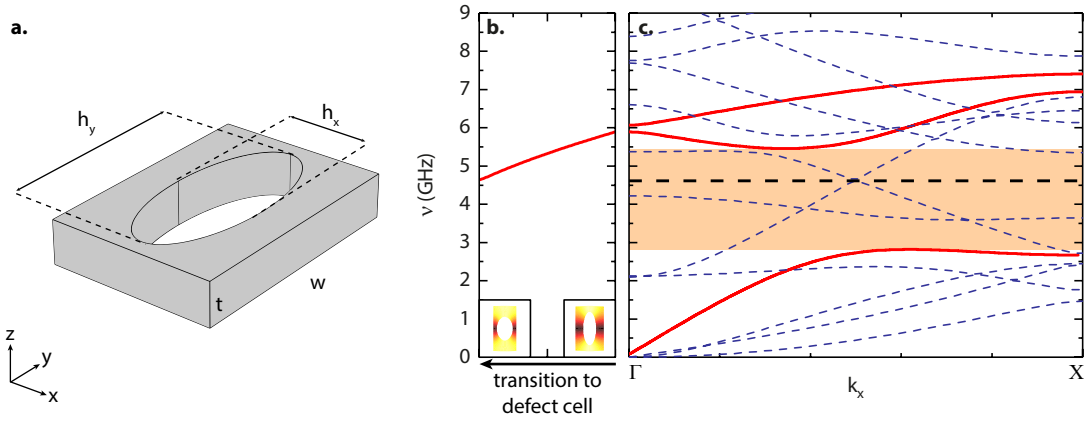

Figure 3.2: **a.** The unit cell of a zipper resonator defined by the geometric parameters $(a, w, h_\mathrm{x}, h_\mathrm{y}, t)_\mathrm{nominal} = (350, 500, 180, 80, 90)$ nm. **c.** Band diagram simulated for the unit cell's projection in x-direction. Bands with mirror plane symmetry about the y- and z-axis (——) and other symmetries (- - -) are set apart and the resulting *quasi-bandgap* (light orange) is highlighted. **b.** Eigenfrequency of the fundamental breathing mode (second red band) in the Γ-point during the transition from the nominal unit cell to the defect cell. The final defect mode frequency $\nu_\mathrm{defect} = 4.61\,\mathrm{GHz}$ is projected (**- - -**) onto **c.** The insets show simulated mode shapes of the breathing mode for the nominal (right) and the fully transformed defect cell (left) with $(a, w, h_\mathrm{x}, h_\mathrm{y}, t)_\mathrm{defect} = (280, 500, 240, 200, 90)$ nm.

Consequently, the discrete periodicity of the structure has to be broken by insertion of a *defect area* within the resonator, which allows the formation of mechanical modes of different frequencies. If the defect area is designed properly, it will exhibit eigenfrequencies which are not allowed to propagate within the nominal (non-defect) structure. The latter will thus act as a reflecting *Bragg mirror*, effectively confining the defect modes to the cavity area. In our structure, the defect is realized by inserting a number of differently shaped, rectangular cells around the center of the resonator.

By performing further FEM simulations of unit cells with different geometries, we find that a cell with shorter size a and a smaller, more circular hole (i.e. $h_\mathrm{x} \approx h_\mathrm{y}$) will exhibit a y-z-symmetric mode with a significantly lower eigenfrequency. The effect of moving from the nominal cell geometry to a defect cell with $(a, w, h_\mathrm{x}, h_\mathrm{y}, t)_\mathrm{defect} = (280, 500, 240, 200, 90)$ nm is illustrated in Fig. 3.2b, where we focus only on the second y-z-symmetric mode at $k_x = 0$. This mode is commonly referred to as *breathing mode*[1] [38], since it is characterized by periodic expansion and contraction of the material along the y-direction, resembling a breathing motion (the mode shape is visualized in the insets). Notably, this defect mode has a frequency of $\nu_\mathrm{defect} = 4.61\,\mathrm{GHz}$ which lies within the quasi-band gap of the nominal projection. As such, a defect with this geometry should theoretically perform mechanical oscillations strictly localized to the defect area.

In order to test this hypothesis, we move on to model a complete zipper resonator, including

[1] While it is possible to localize other modes to the same defect, we choose to focus on the *breathing mode* due to its well suited frequency with an almost linear dependence on the cell geometry. For a discussion of other modes exhibited by a zipper resonator, see Ref. [38].

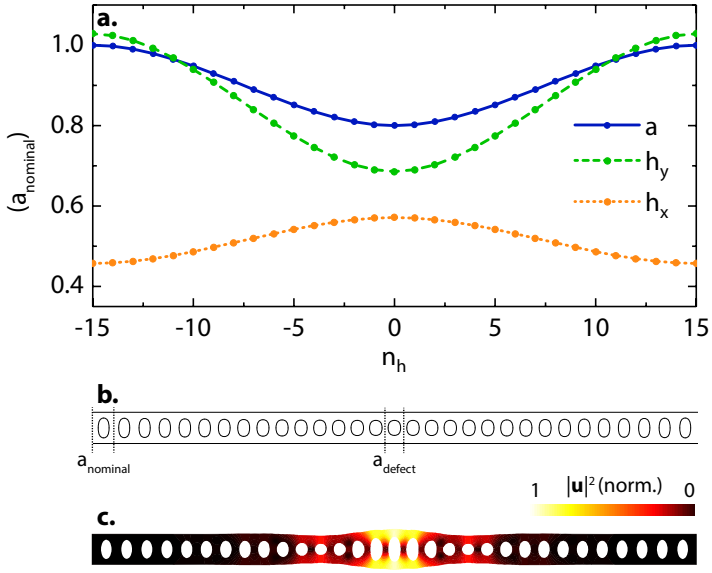

Figure 3.3: **a.** The unit cell parameters a (——), h_y (- - -) and h_x (·····) in units of a_nominal, plotted as a function of the hole index n_h, where $n_\mathrm{h} = 0$ corresponds to the center of the defect area. Within the defect area, the parameters are smoothly transitioned by Eq. 3.1 to the defect geometry $(a, h_\mathrm{x}, h_\mathrm{y})_\mathrm{defect}$ $= (280, 240, 200)$. For indices $|n_\mathrm{h}| \geq 15$, the unit cell remains constant at its nominal dimensions $(a, h_\mathrm{x}, h_\mathrm{y})_\mathrm{nominal} = (350, 360, 160)$ nm. **b.** Illustration of the resulting zipper resonator's defect area. **c.** FEM simulation of the zipper resonator's fundamental breathing mode shape at $\nu_\mathrm{cavity} = 4.764\,\mathrm{GHz}$. The strong localization of the displacement field (color) to the center of the defect area is clearly visible. Note that the deformation of the material is exaggerated for clarity.

the defect area discussed above, in order to perform simulations of the actual structure. We design the resonator to have a total length of 35 μm, offering space for 100 nominal unit cells, and choose the defect area to span 15 holes to each side from the center of the string. Since the suppression of the defect mode in the mirror region is expected to be exponential [81], this number of surrounding nominal cells should be sufficient to form a low-loss phonon cavity. To achieve a gradual modification of the nominal cell towards the defect cell, we transition each of the geometric cell parameters $p \in (a,h_\mathrm{y},h_\mathrm{x})$ with a smooth function of the form

$$p(n_\mathrm{h}) = p_\mathrm{defect} + (p_\mathrm{nominal} - p_\mathrm{defect}) \cdot \left[3\left(\frac{|n_\mathrm{h}|}{N}\right)^2 - 2\left(\frac{|n_\mathrm{h}|}{N}\right)^3\right], \tag{3.1}$$

where $n_\mathrm{h} \in [-N,N]$ is used to index the cells in the defect area with N being the total number of defect cells on each side. Equation 3.1 was chosen to ensure a smooth transition of the cell dimensions, which has been shown to have an influence on optical quality factors [82]. So far, no significant influence of the transition function on the localization of mechanical modes became apparent in the simulations. However, no systematic investigation was performed. The resulting development of the parameters a, h_y and h_x across the defect area is plotted in Fig. 3.3a while the corresponding zipper resonator layout is shown in Fig. 3.3b. Using the transition functions, we obtain a complete description of the zipper resonator's geometry and can proceed to perform

a FEM simulation of the structure's possible eigenfrequencies. While the resonator exhibits a multitude of eigenmodes, we are primarily interested in the breathing mode of the defect cell which we expect around $\nu_{\text{defect}} = 4.61\,\text{GHz}$ according to previous simulations. We find the fundamental breathing mode of the zipper resonator at $\nu_{\text{cavity}} = 4.764\,\text{GHz}$ and present its displacement field in Fig. 3.3c. As expected, the displacement field is confined to a small area of roughly 12 cells within the cavity area of the string. The fact that we find the localized mode shifted to higher frequencies in comparison to the defect cell simulations can be explained given that the actual structure consists of a series of smoothly transitioned defect cells and not a periodic repetition of the fully deformed cell as assumed in the single cell simulations.

3.1.2 Influence of the Cobalt Layer

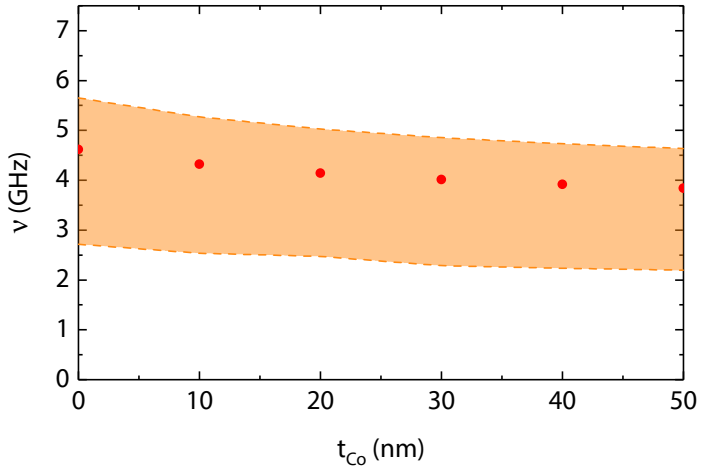

Figure 3.4: Fundamental breathing mode frequency (at the Γ point) of the defect cell (red dots) and size of the quasi-bandgap of the nominal cell (light orange) for increasing thicknesses t_{Co} of Co added in positive z-direction to the unit cell. The values are the result of FEM simulations of unit cells with $(a, w, h_{\text{x}}, h_{\text{y}}, t)_{\text{nominal}} = (350, 500, 360, 160, 90)$ nm and $(a, w, h_{\text{x}}, h_{\text{y}})_{\text{defect}} = (280, 500, 240, 200, 90)$ nm, respectively. We observe a small but steady decline in the size of the quasi-bandgap and the defect mode frequency.

According to the simulations, the localization of phonons should be achievable by fabricating a zipper resonator with the geometric parameters described in the previous section. However, as the aim of this thesis is to investigate magnetoelastics in the zipper structure, it is time to introduce magnetic materials into the discussion. In a fairly straightforward approach, we extend the zipper resonator designed above towards a double-layer system comprised of an additional layer of cobalt applied on top of the Si_3N_4 string. In order to evaluate the impact of this addition on the elastic properties of the zipper resonator, we perform additional single cell FEM simulations for varying thicknesses of Co. The results are shown in Fig. 3.4. In particular, we simulate band diagrams for the nominal cell with dimensions as described above in order to extract the size of the quasi-bandgap. Additionally, we investigate the eigenfrequency of the fundamental breathing mode (at the Γ point) of the fully deformed defect cell as a function of

the Co thickness t_{Co}. The results show a decrease in the bandgap size and defect mode frequency with increasing t_{Co}. However, both effects are comparatively small and do not seem to prohibit mode localization in any way. It should, however, be noted, that the Co layer breaks the perfect mirror symmetry of the zipper structure about the z-axis, which also affects the symmetry of its exhibited modes. Therefore, it is plausible that the mode-mode coupling between modes of formerly completely different symmetry could become non-vanishingly small, creating a loss channel for the localized mode. To this end, it seems advisable to keep the thickness of the Co layer as small as possible from a mechanical standpoint, while still retaining enough magnetic material to observe magnetic resonances. Therefore, we choose a value of $t_{\mathrm{Co}} = 20\,\mathrm{nm}$ for the fabricated samples. Finally, we repeat the simulation of the full zipper geometry as shown in Fig. 3.3 with the addition of the 20 nm Cobalt layer. The localized breathing mode frequency is determined to $\nu_{\mathrm{cavity,Co}} = 4.423\,\mathrm{GHz}$. Tab. 3.1 summarizes the design parameters of the finalized Si_3N_4/Co double-layer structure.

parameter	value
l	$35\,\mu\mathrm{m}$
w	500 nm
t_{SiN}	90 nm
t_{Co}	20 nm
a_{nominal}	350 nm
$h_{\mathrm{x,nominal}}$	160 nm
$h_{\mathrm{y,nominal}}$	360 nm
a_{defect}	280 nm
$h_{\mathrm{x,defect}}$	200 nm
$h_{\mathrm{y,defect}}$	240 nm
N	15
$\nu_{\mathrm{cavity,Co}}$	4.423 GHz

Table 3.1: Summary of the finalized design parameters for the Si_3N_4/Co double-layer zipper resonator.

3.2 Phononic Shields

In an ideal scenario, the nominal cells surrounding the defect region of a zipper resonator act as a series of Bragg mirrors and provide exponential attenuation to modes within their bandgap. Therefore, one would expect losses from the localized defect mode to the clamps and the remainder of the substrate to become negligible as long as the mirror region is made sufficiently large [81, 83]. However, since we are dealing with a quasi-bandgap that relies on the assumption of vanishing coupling between modes of alternate symmetry, small defects inevitably occurring in fabrication processes can cause local symmetry breaking, resulting in energy loss to other modes. This complication becomes even more relevant when considering the broken z-symmetry introduced by the addition of the magnetic top-layer. It has been shown, however, that energy leakage from the string can be strongly reduced by surrounding it with an additional phononic crystal structure which is designed to exhibit a complete bandgap at

the cavity frequency. The surrounding structure thus attenuates modes of any symmetry which would otherwise propagate to the substrate. A design which has been proven to accomplish this task very effectively is the two-dimensional *cross* phononic shield [60], as illustrated in Fig. 3.5. It is constructed from a square unit cell with sidelength c_a, perforated by a cross of width c_w and

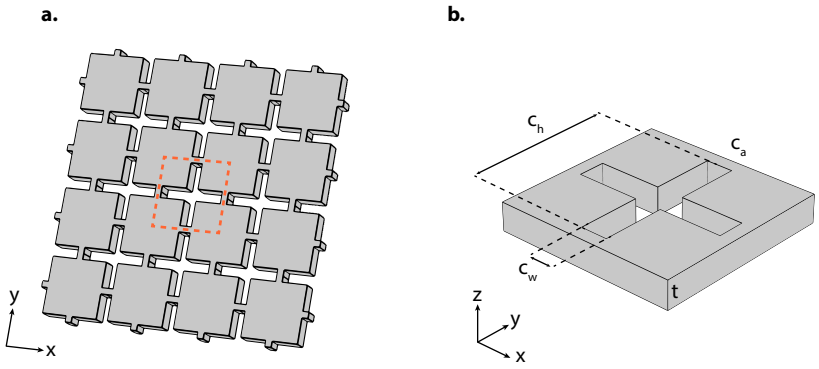

Figure 3.5: a. Schematic illustration of the quasi-2D *cross* phononic shield structure employed to minimize clamping losses of mechanical resonators. **b.** The unit cell defining the phononic shield structure as shown in a. (dashed line). It is constructed by the geometric design parameters $(c_\mathrm{a}, c_\mathrm{h}, c_\mathrm{w}, t)$, which define size and position of the exhibited phononic bandgap.

height c_h. The phononic shield can be considered the extension of the linear chain of *squares* and *bridges*, discussed in Sec. 2.1.2, by introduction of a discrete two-dimensional periodicity (in x- and y-direction). The design has been successfully employed in various experiments (cf. e.g. Refs. [21, 63, 64]), with simulations suggesting a reduction of mechanical loss rates by up to several orders of magnitude [83]. Furthermore, the size and frequency of the exhibited phononic bandgap is widely tunable by altering the design's geometric parameters, a fact we will demonstrate in the following section and use to engineer a suitable shielding specifically for our application.

3.2.1 Band Gap Engineering

In order to design a phononic crystal that provides effective shielding for the previously designed zipper resonator, we aim to find a set of parameters $(c_\mathrm{a}, c_\mathrm{w}, c_\mathrm{h})$[2] of the *cross* unit cell that results in a material with a complete bandgap around $\nu_\mathrm{cavity,Co} = 4.423\,\mathrm{GHz}$. As a starting point, we use values similar to Ref. [64] and, for simplicity, define a fixed ratio of $c_\mathrm{w} = 0.15 c_\mathrm{a}$ and $c_\mathrm{h} = 0.85 c_\mathrm{a}$ for the parameters. Subsequently, we proceed as above and perform FEM simulations of the shield's unit cell, defining periodic Bloch boundary conditions in x- and y-direction and calculating the eigenfrequencies for wave vectors $\vec{\mathbf{k}}$ along the high symmetry points Γ,X,M of the two-dimensional, irreducible Brillouin zone (see Sec. 2.1.1). By repeating the simulation for varying values of c_a, we receive a set of band diagrams, presented in Fig. 3.6b, for differently sized unit cells, effectively mapping out the influence of a uniform scaling operation due to the

[2] The thickness $t = 90\,\mathrm{nm}$ is predetermined by the used sample material and thus kept constant.

fixed relation between the parameters.

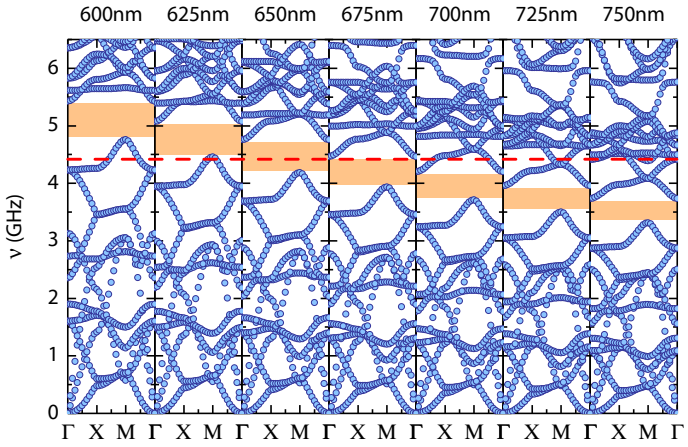

Figure 3.6: FEM simulated band diagrams of the phononic shield unit cell for different values of c_a, showcasing the wide tunability of the resulting band gap (light orange). For simplicity, the other cell dimensions are kept at a fixed ratio of $c_\mathrm{h} = 0.85 c_\mathrm{a}$ and $c_\mathrm{w} = 0.15 c_\mathrm{a}$ respectively, with $c_t = 90\,\mathrm{nm}$ remaining constant. As such, the process corresponds to an uniform scaling operation in the unit cell's x-y-plane. The dashed, red line highlights the localized mode frequency $\nu_\mathrm{cavity,Co} = 4.423\,\mathrm{GHz}$ of the zipper resonator, making the design with $c_\mathrm{a} = 650\,\mathrm{nm}$ a promising candidate for the shielding.

Clearly, the scaling operation has a large, apparently linear, influence on the frequency bands of the shield structure, trending towards lower frequencies for increasing cell dimensions. As a result, the exhibited bandgap (highlighted in light orange) is shifted to lower frequencies and shrunken in width. Remarkably, this shows that the bandgap of the shield structure can be adapted to a wide range of frequencies in a fairly predictable way by performing a simple scaling operation. Comparing the bandgap positions with the cavity frequency $\nu_\mathrm{cavity,Co} = 4.423\,\mathrm{GHz}$ (dashed red line), the design with $c_\mathrm{a} = 650\,\mathrm{nm}$ is identified as a promising candidate for an effective shielding of the localized mode. Naturally, when considering c_w and c_h independently of c_a, the parameter space of possible bandgap positions and sizes becomes even larger. The bandgap is shown to be tunable by more than 5 GHz in a silicon structure in Ref. [60]. In a last step, we use these additional degrees of freedom in order to slightly optimize c_w and c_h for a fixed value of $c_\mathrm{a} = 650\,\mathrm{nm}$, engineering a bandgap which is more precisely centered around the cavity resonance frequency. Through this process we arrive at the finalized geometric parameters for our design $(c_\mathrm{a}, c_\mathrm{h}, c_\mathrm{w}, t) = (650, 570, 100, 90)$ nm.

In conclusion, the simulations confirm that the advantages of the *cross* phononic shield structure, a highly flexible, GHz wide bandgap, which can be shifted across a wide frequency range, can be successfully adapted to our material system and to a frequency range suited for the intended application. Therefore, by surrounding the double-layer zipper resonator with a suitable phononic shield, a significant reduction of the clamping losses should be achievable. Fabricated samples based on the design parameters derived in this and the previous section are presented in Sec. 4.1.

3.2.2 Double-Layer Phononic Shields

Previously, we focused on the sample design of a zipper resonator, intended to localize phonons and investigate their interaction with magnetic modes present in the Co layer of the double-layer structure. In this section, we want to discuss a parallel approach to investigate magnetoelastic interaction, which omits the localization of phonons and relies directly on the ability of phononic shields to exhibit complete phononic bandgaps in the GHz range. By fabricating Si_3N_4/Co double-layer phononic shield structures, we aim to create a magnetic system which also exhibits a phononic band gap at typical frequencies of magnetic resonances (i.e. several GHz). Consequently, we hope to observe the effect of magnon-phonon coupling when comparing magnetic resonance features within and outside of the phononic bandgap.

To this end, we simulate the band diagram of a phononic shield structure using the previously optimized design parameters $(c_a, c_h, c_w, t) = (650, 570, 100, 90)$ nm and model the addition of a Co layer of varying thickness on top of the structure, plotting the results in Fig. 3.7.

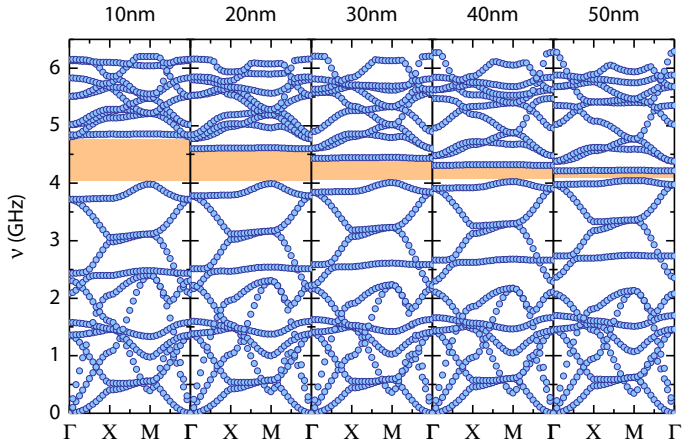

Figure 3.7: FEM simulated band diagrams of a phononic shield unit cell with design parameters $(c_a, c_h, c_w, t) = (650, 570, 100, 90)$ nm for different thicknesses of Cobalt added as an additional layer on top of the Si_3N_4. Clearly, the added inhomogeneity of the material along the z-axis reduces the size of the exhibited bandgap (light orange).

Similar to the observations made in Sec. 3.1.2, the addition of a Co layer leads to a decrease in the size of the band gap due to a strong downwards shift of higher frequency bands. However, in this case the effect is much more pronounced and quickly leads to a vanishingly small bandgap. Considering the results, the design of a magnetic double-layer structure with a complete phononic bandgap seems possible, but clearly, a thickness larger than 30 nm should not be chosen. Fabricated samples based on the double-layer shield design are shown in Sec. 4.2 and corresponding ferromagnetic resonance (FMR) measurements are presented in Chap. 5.

Chapter 4

Fabrication

4.1 Zipper Resonators

Fabrication Procedure

In this section, we detail the fabrication of Si_3N_4/Co double-layer zipper resonators surrounded by a Si_3N_4 phononic shield structure, as designed in Sec. 3.1. The step-by-step fabrication process is illustrated in Fig. 4.1:

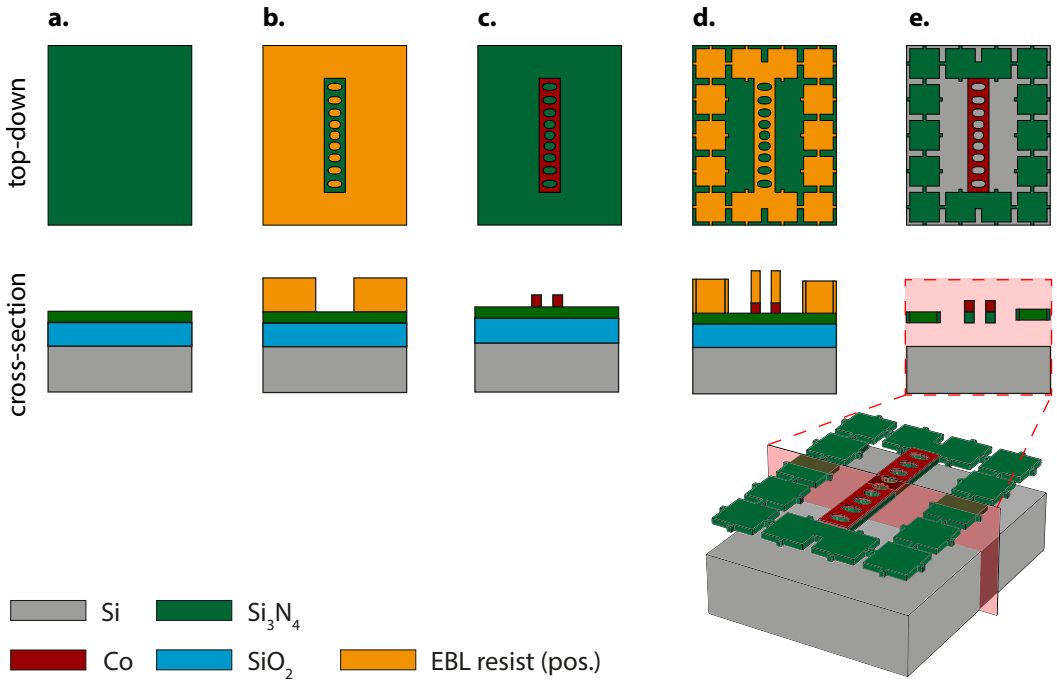

Figure 4.1: Schematic illustration of the thin film fabrication process of a Si_3N_4/Co double-layer zipper resonator surrounded by a phononic shield structure. Each step is presented in a top-down view (top row) and a corresponding cross-section through the sample as visualized in the 3D model in the bottom right. The individual process steps are described in the main text. Note that the size and placement of the zipper resonator with respect to the phononic shield are not to scale.

a. We commence with a commercially available silicon wafer, which is covered with a 200 nm thick sacrificial layer of SiO_2 and 90 nm of tensile stressed Si_3N_4 by low pressure chemical vapor deposition (LPCVD). **b.** The substrate is coated with positive resist and a mask in the shape of the zipper resonator is structured using electron beam lithography (EBL). **c.** A Co layer of desired thickness is evaporated onto the sample and a subsequent lift-off process is performed in order to remove the resist mask, along with excess Co. Due to the small dimensions of the elliptic holes in the zipper design, a lift-off using warm acetone can fail to remove the resist layer without residue. Better results were accomplished by employing a solvent based remover recommended for the used resist. **d.** Another layer of positive resist is applied and structured using EBL. In this step, the mask defines the phononic shield structure, but also includes the previously structured zipper layout to protect the Co layer. **e.** The resist mask is transferred into the substrate using a short anisotropic reactive ion etching (RIE) process. Afterwards, a wet etching step with buffered hydrofluoric acid (BHF) solution ($\approx 3\%$) removes the majority of the SiO_2 layer, leaving the resonator and the surrounding shield freely suspended. The etching process is terminated by rinsing the sample with H_2O, followed by multiple ethanol baths, which remove the remaining resist layer. Finally, the sample is carefully dried using a critical point dryer (CPD) in order to minimize potential damage to the delicate structures.

Fabricated Samples

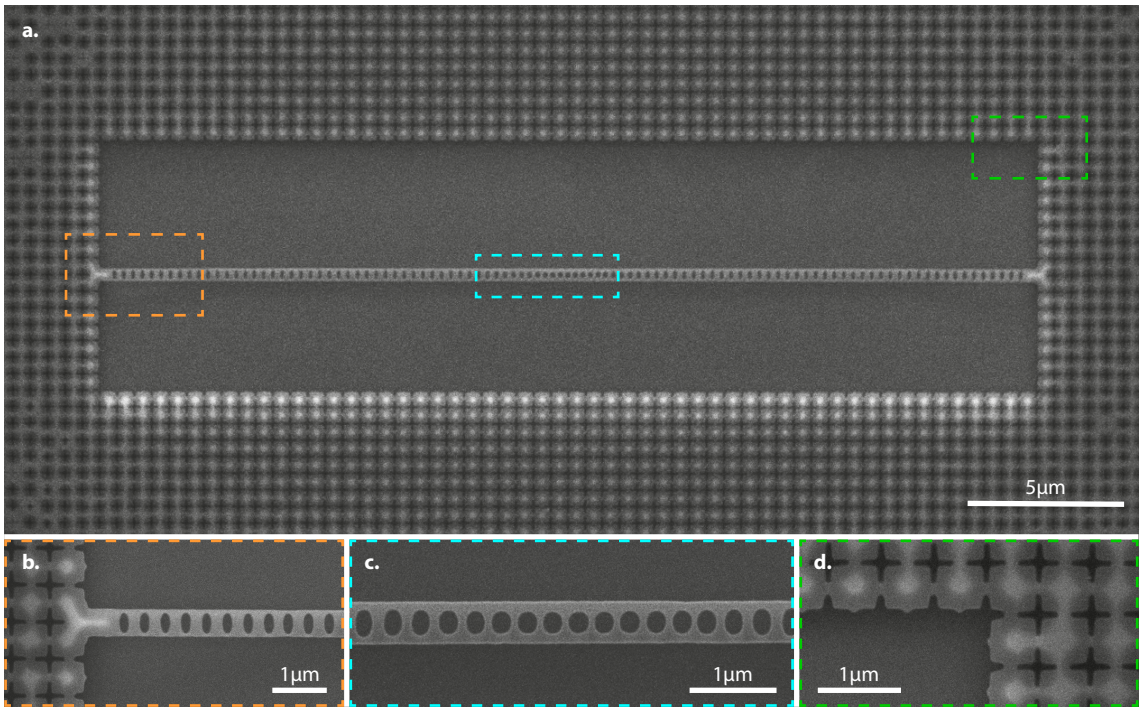

Figure 4.2: **a.** Scanning Electron Microscopy (SEM) image of a fabricated zipper resonator surrounded by a *cross* phononic shield structure as designed in Sec. 3.1. **b.** Zoom-in on the *clamping area*, connecting the zipper resonator to the phononic shield. **c.** Zoom-in on the defect region in the center of the zipper resonator, showcasing the gradually changing hole shape and cell size. **d.** Zoom-in on the edge of the phononic shield region of the sample.

Scanning Electron Microscopy (SEM) images of a finished sample, fabricated as detailed above with the design parameters derived in Sec. 3.1, are shown in Fig. 4.2. The employed lithography process proves capable of sharply defining the nm-sized features comprising the zipper resonator (**b.** and **d.**) and the phononic shield (**d.**). Furthermore, a good agreement between the designed feature size and the observed structures is reached, at least to the accuracy of the scale provided by the SEM software. In particular, we measure a slightly reduced beam width $w \approx 480\,\mathrm{nm}$ and almost perfectly reproduced dimensions of the central hole, i.e. $h_x \approx 201\,\mathrm{nm}$ and $h_y \approx 240\,\mathrm{nm}$. From the top-down view provided in Fig. 4.2, the edges of the structure appear to be sufficiently under-etched to be freely suspended and only supported at the edges of the phononic shield area (not shown). However, it does not become clear whether the center of the squares forming the phononic shield are fully released. The brighter spots (see panel **b.** and **d.**) could signify material below the Si_3N_4 layer that is still connected to the substrate. On the other hand, it is expected that the protective resist layer which covers the shield structure during the etching process is attacked by the BHF. Therefore, the bright spots might also indicate a concentric degradation of the top-layer itself, while the structure is fully released.

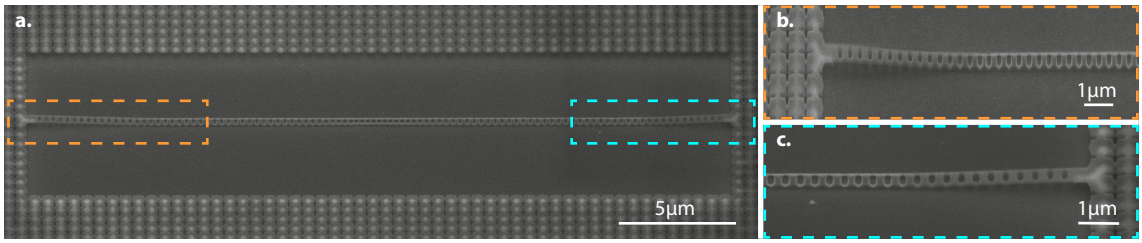

Figure 4.3: Angled (55°) Scanning Electron Microscopy (SEM) images of the fabricated sample structure shown in Fig. 4.2. **a.** Wide, angled view of the zipper resonator surrounded by a *cross-design* phononic shield. **b-c.** Zoom-in on the left (**b.**) and right (**c.**) *clamping areas*. It becomes obvious in the angled view that the zipper resonator was successfully under-etched, but its central section subsequently collapsed and is stuck to the substrate.

In order to gain more information about the state of the structure, we tilt the sample and analyze SEM images from an angled perspective, as presented in Fig. 4.3. It becomes clear that the central section of the zipper resonator was successfully released (see panels **b.** and **c.**), but did subsequently collapse onto the substrate. Notably, we find released and collapsed zipper resonators not only in the shown structure, but in a total of 20 identical resonators, located on two different chips that underwent an identical fabrication process. Therefore, we assume the collapse not to be caused by an external influence damaging the structure, and instead conclude that the current zipper design is inherently incapable of supporting itself once released from the substrate. We attribute the lack of structural integrity to the lower thickness of the material (90 nm Si_3N_4) in comparison to other published works involving zipper resonators (220 nm Si in Ref. [64] and 350 nm Si_3N_4 in Ref. [44]). Notably, solid string resonators made from the same material system can be released from the substrate and remain stable, but the perforations necessary for the zipper design seemingly weaken the structure sufficiently to collapse during the release. While this implies that stable zipper structure can not be fabricated on the material system currently in use, we are confident that, given the favorable lithography results, the

established process can be quickly adapted to a new material system and successfully produce a freely suspended zipper resonator.
Conversely, even after investigation of the angled SEM images, it is still unclear whether the phononic shield structure surrounding the resonator is fully released from the substrate. To positively confirm or refute this, a destructive measurement would have to be performed. For example a section of the structure could be cut free by a focused ion beam (FIB). Subsequently it would be possible to determine via SEM whether the structure has collapsed or is still supported.

4.2 Double-Layer Phononic Shields

Fabrication Procedure

In the following, we will detail the fabrication process of the second sample type, a Si_3N_4/Co double-layer phononic shield structure, which we discussed in Sec. 3.2.2. A schematic illustration of the process steps is presented in Fig. 4.4:

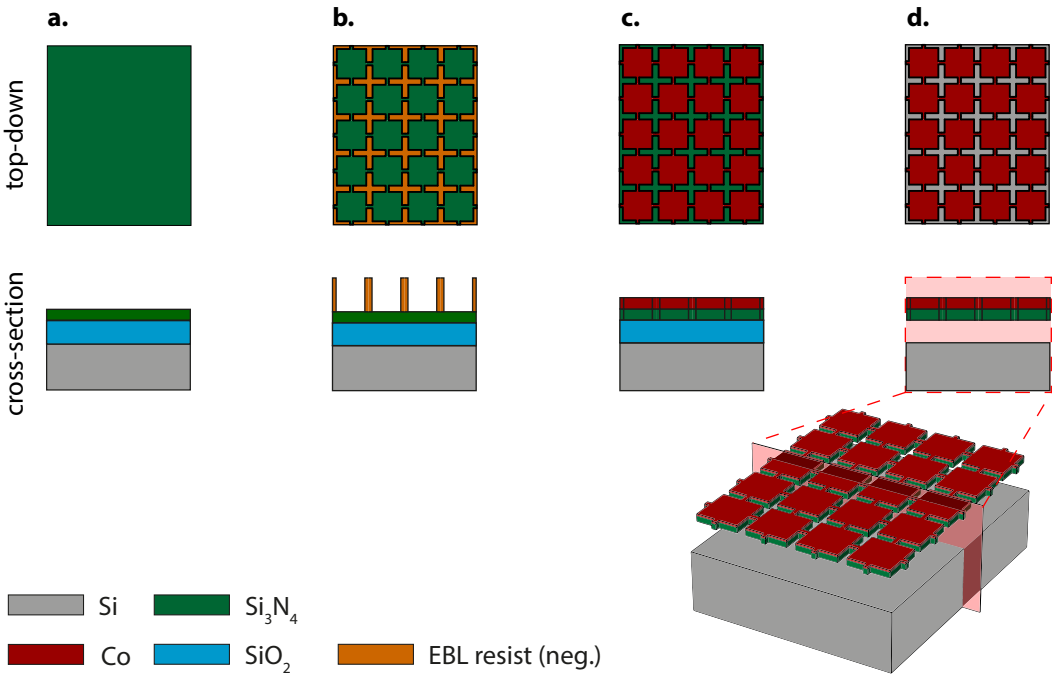

Figure 4.4: Schematic illustration of the thin film fabrication process of a Si_3N_4/Co double-layer phononic shield structure. Each step is presented in a top-down view (top row) and a corresponding cross-section through the sample as visualized in the 3D model in the bottom right. A detailed description of the process steps can be found in the main text.

a. The substrate is identical to the one discussed above, i.e. silicon with a sacrificial layer of 200 nm SiO_2 and 90 nm of tensile stressed Si_3N_4 deposited by LPCVD. **b.** The sample is coated with negative resist and the phononic shield structure is defined using EBL. The use of negative resist is advisable for this type of structure, since it requires exposition of the smaller *cross* area (orange), as opposed to the larger *squares* (green), greatly reducing the negative effects of

back-scattering [84] during EBL. **c.** Cobalt of desired thickness is evaporated onto the sample and the resist mask is removed in a lift-off process. As described above, a specialized remover did achieve better lift-off results for the small cross-like structures compared to warm acetone. **d.** The shield structure is transferred into the substrate by anisotropic RIE and subsequently released by a wet etching process with BHF solution ($\approx 3\%$), which dissolves the sacrificial SiO_2 layer. The termination of the etching process is achieved by H_2O, followed by removal of the resist in ethanol baths. Finally, the samples are dried using a CPD process.

For more information regarding specific process steps or parameters, please refer to App. A.4.

Fabricated Samples

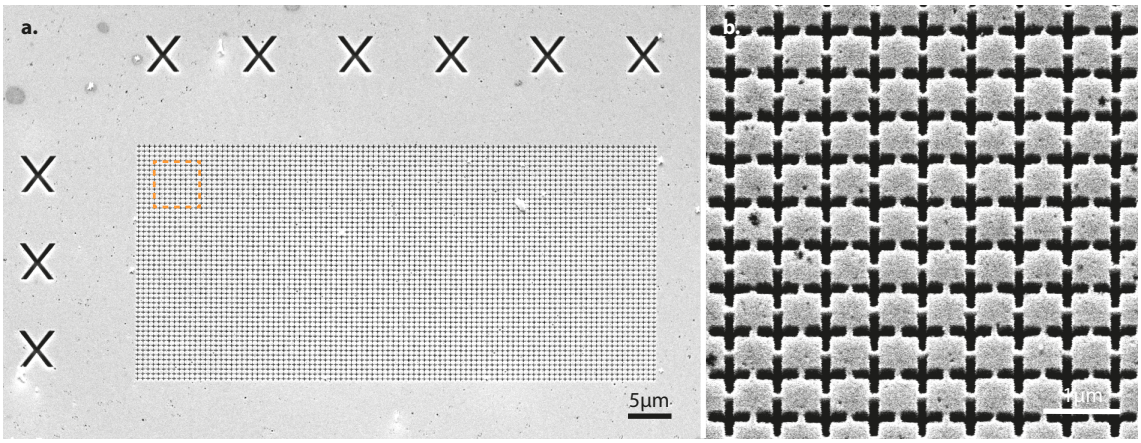

Figure 4.5: **a.** Wide, angled (55°) view of a fabricated Si_3N_4/Co double-layer phononic shield structure. The X-shaped features are markers intended for alignment of optical measurements. **b.** A detailed look at the dashed orange area of the phononic shield structure.

Here, we present SEM images of Si_3N_4/Co double-layer phononic shield samples, fabricated according to the procedure detailed above. In Fig. 4.5, an angled view of a small phononic shield array spanning roughly 60x30 μm^2 is shown, along with surrounding X-shaped markers, intended for alignment purposes in measurements. The periodic cells appear to be nicely and consistently defined, and only a few defects, mostly consisting of resist residue, are found. Comparing the observed feature dimensions with the designed parameters, we find slightly enlarged trenches (i.e. *crosses* with $c_w \approx 117\,\text{nm}$) at the cost of smaller *squares* ($c_a \approx 507\,\text{nm}$). These are most likely effects of *beam broadening* [84] during the EBL process. Following further quantification of these deviations, it should be possible to derive a correction factor which can be applied to the layout in order to achieve more precisely replicated dimensions. Notably, it can not be positively determined from the images whether the structure is fully released from the substrate. As previously discussed in Sec. 4.1, a definite proof can only be gained from destructive measurements (e.g. cutting the sample with FIB). However, based on the experiences with the zipper design (i.e. the released but collapsed resonator) and the evaluation of damaged sample structures (shown in Fig. A.9), we believe that the wet etching duration was sufficient to leave this phononic shield structure freely suspended.

Chapter 5

Experimental Results

In Section 2.2, we discussed the theory of magnetoelastic interaction, i.e. how the magnetization dynamics of a material are influenced by mechanical oscillations of the same body. Furthermore, we discussed the principle of ferromagnetic resonance (FMR) and how it can be affected by the magnetoelastic coupling. We found that the stress induced by mechanical oscillations leads to a change of the effective magnetic field in the material. Thus, as the ferromagnetic resonance frequency depends on the same effective magnetic field (see Eq. 2.15), we expect the effect of magnon-phonon coupling to be observable in FMR measurements, i.e. through a shift in resonance frequency. Therefore, in this chapter, we experimentally investigate two different Si_3N_4/Co double-layer phononic shield samples, which we designed in Sec. 3.2.2, using FMR measurements. Notably, the samples were fabricated as detailed in Sec. 4.2, but were not exposed to the final wet etching process. Consequently, the phononic shield structures are not fully released and still supported by the substrate. Unreleased samples have been chosen because a FMR measurement as performed here, especially the placement of the sample (which we will discuss shortly), would likely damage or even destroy a freely suspended structure. As such, the samples are not expected to exhibit the designed phononic bandgap, which would allow the comparison of FMR lines within and outside of the frequency range of the bandgap in order to determine the influence of resonant magnon-phonon interaction. Instead, the samples will be used to investigate the magnetization dynamics of the fabricated hybrid structures and use this knowledge to optimize the design in future iterations.

Figure 5.1a-b shows schematic illustrations of the two investigated samples. Both samples are designed using the finalized geometric parameters derived from the simulations in Sec. 3.2.2 with a chosen cobalt layer thickness of 30 nm. The sample shown in panel **a.** consists of a small phononic shield structure (dotted red area), spanning roughly 1x1 mm^2, which is centered on a 6x5 mm^2 chip. Notably, the remainder of the chip is covered with an unstructured Co layer. The second sample (see panel **b.**) contains a larger phononic shield structure spanning 3x1.3 mm^2, centered on a chip of identical size. Furthermore, the surface of the chip, aside from the phononic shield area, was cleared of any excess Co.
For the measurement, we employ a standard broadband ferromagnetic resonance (bbFMR) spectroscopy setup (cf. e.g. Refs. [86, 87]). To this end, the sample is mounted on the center

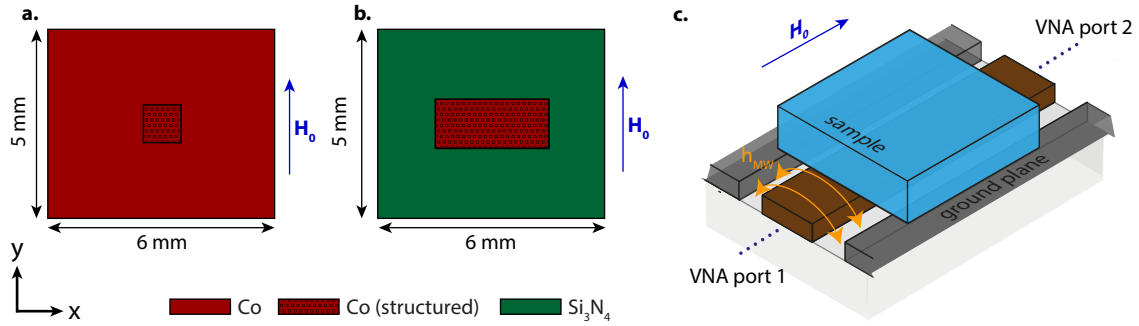

Figure 5.1: a-b. Top-down view on a schematic sample geometry of the two investigated double-layer phononic shield samples. Sample **a.** consists of a small phononic shield structure (dotted red area), spanning roughly 1x1 mm^2. The remainder of the chip is covered with an unstructured, homogeneous Co film (red). Sample **b.** contains a larger phononic shield array spanning 3x1.3 mm^2 and the surface of the chip was cleared of any excess Co. The blue arrows indicate the magnetic field orientation during the measurement. **c.** Schematic experimental setup for broadband FMR measurements. The sample is placed in flip-chip orientation on the center conductor (brown) of a coplanar waveguide (CPW). An external magnetic field $\vec{\mathbf{H}}_0$, oriented along the sample plane (blue arrow), is applied to the area by an electromagnet. A vector network analyzer (VNA) connected to the ends of the center conductor applies a microwave signal which induces an oscillating magnetic field $\vec{\mathbf{h}}_{\mathrm{MW}}(t)$ (orange arrows). In the measurement, the microwave transmission parameter S_{21} between the two ports of the VNA is analyzed. The figure in panel **c.** is adapted from Ref. [85].

conductor of a coplanar waveguide (CPW) in flip-chip orientation, i.e. with the top layer of the sample directly facing the CPW. The CPW is then placed in the homogeneous magnetic field region of an electromagnet so that the external field $\vec{\mathbf{H}}_0 = H_0\hat{\mathbf{y}}$ acts along the sample plane (*in-plane* orientation), as illustrated in Fig. 5.1c. The ends of the center conductor are connected to the ports of a vector network analyzer (VNA). The VNA applies a microwave signal the center conductor, inducing an oscillating magnetic field $\vec{\mathbf{h}}_{\mathrm{MW}}(t)$ which interacts with the magnetization of the investigated sample. After passing through the conductor, the transmitted microwave signal is returned to the VNA, which measures the complex transmission parameter of the setup S_{21} as a function of the microwave frequency $\nu = \omega_{\mathrm{MW}}/2\pi$. As discussed in Sec. 2.2.2, an increased absorption in the transmission spectrum is found when the frequency of the microwave field is resonant with the internal precession frequency ω_{res} of the samples magnetization. The process is then repeated for a multitude of (temporarily) constant magnetic field amplitudes H_0. In each measurement, we investigate frequencies and magnetic fields up to 50 GHz and 1.25 T respectively.

The results of the first measurement, preformed with the sample shown in Fig. 5.1a are presented in Fig. 5.2. In panel **a.**, we show the experimentally measured transmission parameter in the form of its *derivative divide* $\partial_D S_{21}/\partial H$, a numerical derivative technique which is highly successful in removing the signal's background (see App. A.1 and Ref. [88]). We observe two strong, distinct resonance lines that shift upwards in frequency roughly parallely as the magnetic field is increased. Furthermore, curious vertical features can be observed between $\mu_0 H_0 \approx 0.7\,\mathrm{T}$ to $0.9\,\mathrm{T}$. These are known to be unphysical measurement artifacts, which regularly

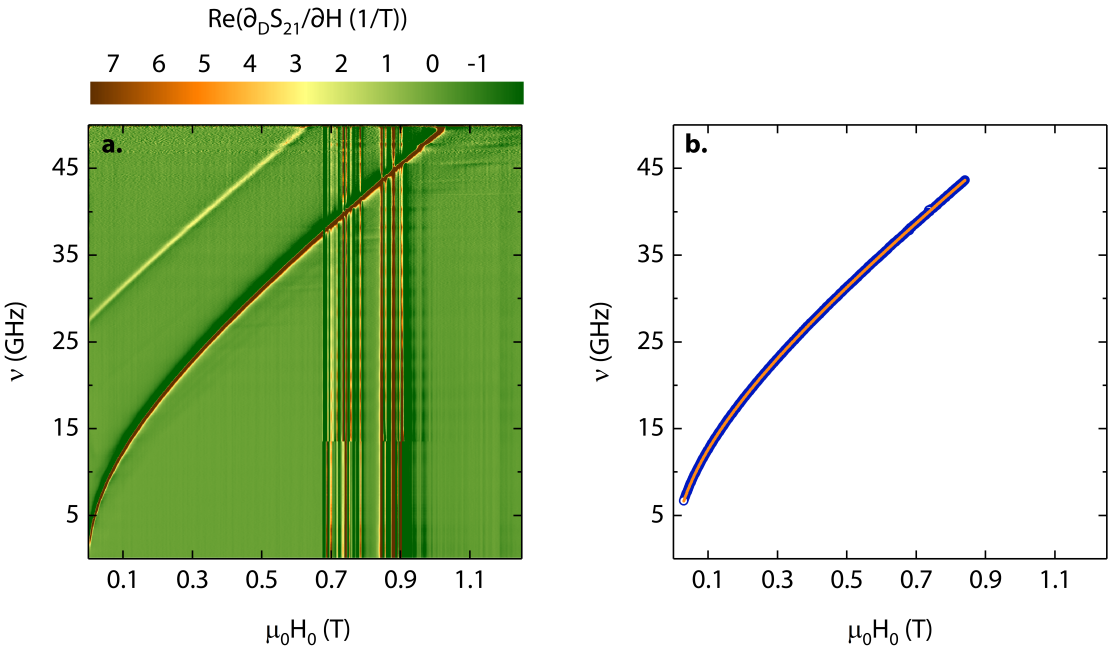

Figure 5.2: **a.** bbFMR measurement data of the first sample, featuring a 1x1 mm^2 phononic shield structure as shown in Fig. 5.1a. Shown is the real part of the field-derivative of the VNA transmission spectra as a function of magnetic field and frequency. We observe two strong, distinct resonance lines which shift in frequency as the externally applied field H_0 is swept. The lower line is attributed to the FMR, while the upper line is identified as a perpendicular standing spin wave (PSSW). Note that the vertical features between $\mu_0 H_0 \approx 0.7\,\mathrm{T}$ to $0.9\,\mathrm{T}$ are known to be caused by small cable movements or similar disturbances to the measurement setup. The experiment was performed with the microwave power $P_{\mathrm{MW}} = 0.1\,\mathrm{mW}$. **b.** The blue circles indicate the resonance frequencies of the FMR mode, extracted by fitting the data in panel a, where possible. The orange line is a fit to the resonance frequencies according to Eq. 2.17. From the fit we extract $\mu_0 M_{\mathrm{sat}} = 1.697\,\mathrm{T}$ and $g = 2.135$.

appear in the measurement setup, caused by cable movements or similar disturbances. Notably, the dispersion of the lower, high intensity mode is visible almost through the entire measurement and traverses frequencies from 1 GHz to 50 GHz. By comparing the observed behaviour to FMR measurements found in literature (cf. e.g. Refs. [89–91]), we find that a dispersion of this form is typical for ferromagnetic resonance lines. The higher-frequency mode on the other hand can be attributed to a perpendicular standing spin wave (PSSW). PSSWs are additional, standing spin wave modes that form between the boundaries of thin films perpendicular to the applied magnetic field, and are the topic of various publications [89, 91]. In this case however, we will focus the discussion on the analysis of the FMR mode and neglect the PSSW for the time being. In order to quantitatively analyze the data, we extract the resonance frequencies from the experimental data by fitting the individual spectra with the expected resonance lineshape found in the form of the derivative divide (see App. A.1). The extracted resonance frequencies are shown in Fig. 5.2b. Note that not all spectra could be successfully fitted due to the previously discussed artifacts. According to theory (see Sec. 2.2.2), the dispersion of FMR frequencies should be described by the Kittel equation, in particular Eq. 2.17, since $\vec{\mathbf{H}}_0$ is oriented in-plane with the sample structure. Therefore, we attempt to fit the experimentally observed frequencies

to Eq. 2.17 and plot the result as a solid line in panel **b.** The equation is able to match the experimental data excellently and allows us to extract several material parameters. We obtain $\mu_0 M_{\mathrm{sat}} = 1.697\,\mathrm{T}$ for the saturation magnetization and $g = 2.135$ for the Landé-factor. By comparison with literature values, reasonably good agreement is found between the reported saturation magnetization of a cobalt thin film and the measured value. In particular, in the supplementary material to Ref. [92], a saturation magnetization of $\mu_0 M_{\mathrm{sat}} \approx 1.775\,\mathrm{T}$ is reported. Regarding the Landé-factor, one theoretically expects a value of $g \approx 2$ for elemental ferromagnets. However, an increased g in association with microwave-driven resonance experiments is reported [93]. Given these results, the data appears to be in line with measurements of fully homogeneous cobalt thin films and no significant influence of the phononic shield structure is found. Recalling the sample geometry (see Fig. 5.1a), this is likely a consequence of the presence of the unstructured Co film around the shield structure. Since bbFMR measurements are not localized, it seems plausible that the FMR signal of the large Co thin film dominates and overshadows any influence the phononic shield structure might have had on the transmission spectra. To test this hypothesis, we perform an identical bbFMR measurement on the second fabricated sample (see Fig. 5.1b) which does not feature an extended cobalt thin film.

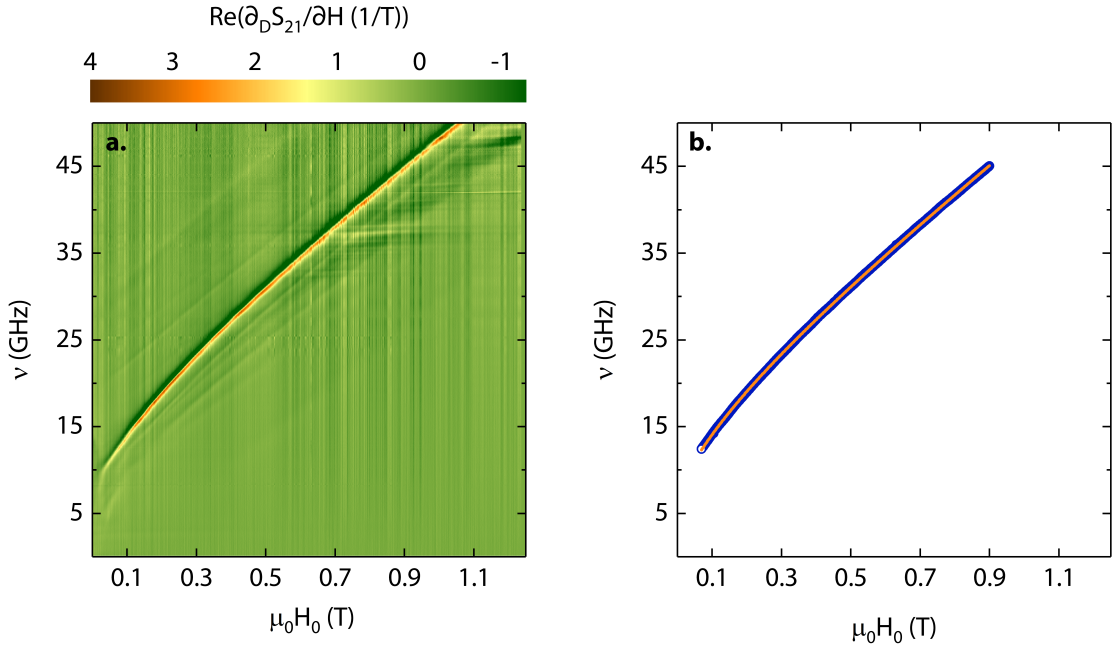

Figure 5.3: a. bbFMR measurement data of the second sample, featuring a 3x1.3 mm^2 phononic shield structure as shown in Fig. 5.1b. Shown is the real part of the field-derivative of the VNA transmission spectra as a function of magnetic field and frequency. We observe one strong, and many weaker resonance lines shifting in frequency as the external field H_0 is swept. The additional resonance lines are well visible between $\nu \approx 15\,\mathrm{GHz}$ to $25\,\mathrm{GHz}$. The strongest mode is again attributed to the FMR. The remaining modes are discussed in the main text. The experiment was performed with the microwave power $P_{\mathrm{MW}} = 0.1\,\mathrm{mW}$. **b.** The blue circles indicate the resonance frequencies of the FMR mode, extracted by fitting the data in panel a, where possible. The orange line is a fit to the resonance frequencies according to Eq. 2.17. From the fit we extract $\mu_0 M_{\mathrm{sat}} = 1.386\,\mathrm{T}$ and $g = 2.179$.

The acquired measurement data is presented in Fig. 5.3. We proceed as above and investigate panel **a.**, which shows the derivative divide of the experimentally measured microwave transmission parameter. In this measurement, we observe only one strong resonance line but a much larger number of lower-intensity resonance features (especially visible around $\nu \approx 15\,\mathrm{GHz}$ to $25\,\mathrm{GHz}$). As previously, we attribute the strongest resonance line to the FMR, based on its high intensity and the shape of the dispersion, which appears very similar to the previous measurement. However, the line only becomes visible for frequencies $\nu > 10\,\mathrm{GHz}$, a significantly different behavior than in the previous measurement, where the dispersion could be observed over the full frequency range. A possible interpretation of this finding is that a higher magnetic field is required to align a majority of the spins in the phononic shield structure compared to the homogeneous film. The structure of the phononic shield (i.e. the squares separated by trenches) imposes additional boundary conditions on the propagation of spin waves. This could make the formation of other, more localized spin wave energetically favorable compared to the collective ferromagnetic resonance for weak magnetic fields. In individual, nano-structured permalloy disks such localized spin wave modes in the low GHz regime have been experimentally observed [94]. Furthermore, It is very likely that the appearance of the additional resonance lines in this measurement can be explained by a similar argument. In particular, the previously discussed boundary conditions imposed by the periodic structure of the phononic shield will lead to a much more complex magnonic bandstructure in the material, allowing for the formation of additional spin wave modes aside from the FMR. The number of modes is likely additionally increased due to the inevitable variatation that arises from fabrication as well as by defects in the geometry of the structure. In other words, cobalt squares of slightly different size will exhibit internal magnetic resonances of slightly different frequency. In order to gain deeper insight into the various spin waves in nano-structured materials, the geometry would need to be evaluated using micromagnetic simulation tools [73, 95], which have already been employed successfully in similar contexts [94].
Moving on to a quantitative analysis of the data, the resonance frequencies of the main FMR line are extracted using fits to the experimental data (see App. A.1) and plotted in Fig. 5.3b. The discrepancy compared to the previous measurement also shows in the fitting process, as no frequencies could be successfully extracted for fields below $\mu_0 H_0 = 0.1\,\mathrm{T}$, where the FMR line begins to vanish. Fitting the resonance frequencies to the in-plane Kittel equation (Eq. 2.17) produces the fitting parameters $\mu_0 M_{\mathrm{sat}} = 1.386\,\mathrm{T}$ for the saturation magnetization and $g = 2.179$ for the Landé-factor. While the g-factor is comparable to the previous measurement and the expectation, M_{sat} is found to be significantly lower than before. Given the nominally identical material, we assume an actual change of the saturation magnetization in this magnitude to be unlikely. Instead, it is possible that the Kittel equation is no longer able to accurately describe the resonance behavior of the system. Recalling Sec. 2.2.2, we made several assumptions related to the geometry of the sample in the derivation of the in-plane Kittel equation. In particular, the demagnetization factors $N_{x,y,z}$ were chosen assuming an infinitely extended, homogeneous thin film geometry. It seems plausible that some of these assumptions do not hold when confronted with the complex geometry of the phononic shield structure.

In conclusion, we find that the phononic shield's geometric structure clearly influences the

spin wave modes present in the material, an effect which is expected for nano-structured magnetic materials. We observe the disappearance of the FMR line below $\nu \approx 10\,\mathrm{GHz}$, which implies that resonant magnon-phonon coupling with the Kittel mode would not be observable in this sample at frequencies close to the designed phononic bandgap ($\nu \approx 4.4\,\mathrm{GHz}$). This shows that it is crucial to consider the influence of the sample geometry on the FMR mode, and the magnonic modes in general, in the design process of any subsequent magneto-mechanical hybrid structures. In particular, the engineering of phononic modes, as performed in this thesis, has to be coordinated with the engineering of magnonic modes, which can be achieved by performing micromagnetic simulations [73, 95].

Moreover, it would be desirable to investigate the sample with other measurement techniques that offer spatial resolution, e.g. micro-focused Brillouin light scattering (BLS) spectroscopy [96] or magneto-optical Kerr effect (MOKE) techniques [97], which allow visualization of local spin wave propagation within the shield structure. In addition, BLS spectroscopy would enable us to investigate the phonon- and magnon- modes of the freely suspended phononic shield structures shown in Sec. 4.2 and hereby allow to test the fidelity of the simulations regarding the phononic engineering presented in Sec. 3.2. In these samples, the existence of a phononic band gap could be examined and the effects of magnon-phonon coupling could possibly be observed.

Chapter 6

Summary

Throughout the first part of this thesis, we developed design and fabrication processes for two different magneto-mechanical hybrid structures, namely a zipper-type phonon cavity and a double-layer phononic shield structure designed to exhibit a complete phononic bandgap. Both hybrid structures are intended to be employed as novel platforms for the investigation of magnetoelastic interaction.

We successfully adapted established designs from the field of optomechanics to incorporate ferromagnetic materials. Using FEM simulations we demonstrated that a newly designed extension of the zipper-type optomechanical crystal, featuring a magnetic layer of cobalt, is capable of confining GHz-frequency phononic modes despite the altered material system. We also showed that the design can be widely tuned regarding its localized frequency by controlling macroscopic, geometric parameters. Additionally, we introduced a second sample design, which does not rely on the localization of phonons to a cavity region but is instead based on the *cross* phononic shield structure. Similarly to the zipper resonator, we successfully expanded the design towards a Si_3N_4/Co double-layer structure, retaining the essential feature of the original phononic shield, namely the complete phononic bandgap, which is widely tunable by altering geometric parameters.

Subsequently, we established a suitable thin film fabrication process for both sample geometries, involving the challenging optimization of the final wet etching step, where we are confident to have found a set of parameters which will reliably succeed in producing freely suspended structures. Upon evaluating SEM images of fabricated sample structures, we found the established lithography process to be sufficiently accurate in replicating the nanometer-sized features necessary to define the zipper cavity as well as the phononic shield. Unfortunately, all fabricated zipper-type samples appeared to lack the necessary structural integrity to support themselves once released from the substrate. We attribute this to an insufficient thickness of the sample material. Consequently, no working zipper-type sample could be fabricated in the limited time frame of this thesis. Due to the otherwise favorable results, however, we are confident that the established process can be quickly adapted to a new, thicker material system and successfully produce a freely suspended zipper resonator in the near future.

Conversely, the second sample type, the double-layer phononic shield structure, could be successfully fabricated and investigated in a first series of measurements. In broadband FMR measurements, we found a significant difference in the FMR measurement signature of a phononic shield structure in comparison to a quasi-homogeneous thin film. We concluded that the altered signature is likely a consequence of the finite size of the phononic crystal structure, which influences the exhibited magnon modes in the material. Therefore, in order to investigate magnon-phonon coupling, the sample geometry has to be engineered not only regarding its elastic properties, but also considering the effects on the exhibited magnon modes. Notably, this is a crucial realization for the design process of any future magneto-mechanical hybrid structure. Lastly, micro-focused BLS spectroscopy measurements on the same sample type could not be completed in time due to technical problems of the measurement setup. However, once the problems are resolved, these measurements will allow to test the existence of a phononic bandgap within the phononic shield structure and evaluate the fidelity of the phononic engineering performed in this thesis.

Part II

Nanomechanical Resonator Networks

Chapter 7

Introduction

The second part of this thesis is dedicated to the investigation of strong inter-resonator coupling between nanomechanical string resonators (*nanostrings*) and its applications. We design and fabricate networks of multiple high-Q nanostring resonators, which are mechanically coupled by a shared support structure, forming a fully mechanical and classical multi-level system [98–100]. Such systems allow the exploration of quantum-classical analogies to a variety of phenomena like population oscillations [101, 102], Landau-Zener-Stückelberg dynamics [103–105] and electromagnetically induced transparency [106]. In addition, they represent an important step towards all-mechanical realizations of information processing [107–109] and storage [110–112].

By definition, almost all of these applications require strong inter-resonator coupling, the ability to perform targeted transfer of phonons, and the possibility to control the resonance frequency of individual resonators (or modes), with the latter commonly achieved through application of electric fields [106, 113, 114]. Throughout this part of the thesis, we demonstrate all three of these key requirements in our nanostring resonator networks using a recent, purely mechanical *eigenfrequency tuning technique* [105] based on the inherent *geometric non-linearity* of tensile stressed nanostring resonators. Therefore, in our system, we completely eliminate the need for electric fields and the corresponding local control gates and offer an alternative, fully mechanical approach to the design of multi-resonator networks.

We establish theoretical background and the mathematical foundation for the description of nanomechanical resonator networks in Chapter 8, which is divided into three parts.
Section 8.1 introduces a simplified one-dimensional oscillator model for the vibrational motion of a tensile stressed nanostring and employs it to derive a theoretical model for the interaction in arbitrarily large, mechanically coupled resonator networks. In Section 8.2, we explore the transition dynamics of multi-level systems and discuss how the Landau-Zener model of quantum tunneling can be applied to describe coherent transfer of phonons between coupled resonators. Section 8.3 deals with the inherent geometric non-linearity of nanostrings and examines how it can be exploited to manipulate a nanostring's resonance frequency in situ, introducing the mechanical eigenfrequency tuning technique which will be used extensively in experiments. In Chapter 9, we discuss the fabrication procedure of Si_3N_4 nanostring resonators and present

the three different resonator network designs fabricated and investigated in the scope of this thesis. The employed measurement setups and signal processing systems are then examined in Chapter 10. Lastly, we present experimental data in Chapter 11. Using optical interferometry techniques, we characterize single Si_3N_4 nanostrings regarding their quality factors and material parameters in Section 11.1. We move on to the investigation of multi-nanostring networks in Section 11.2, where we investigate the capabilities of the eigenfrequency tuning technique and employ it to quantify the inter-resonator coupling of the three fabricated networks. Finally, we present the results of Landau-Zener-type experiments in Section 11.3, demonstrating targeted excitation transfer between nanostring resonators in the same network. The findings are then summarized in Chapter 12.

Chapter 8

Theory

8.1 Nanomechanical String Resonators

This section is dedicated to a theoretical treatment of nanomechanical string resonators, referred to in the following as *nanostrings*. We will introduce an easily accessible description of the string's oscillatory motion, describe the fundamental formulas that are employed in the experiments and discuss the interaction of multiple resonators in a mechanically coupled network.

8.1.1 Fundamentals of Nanostrings

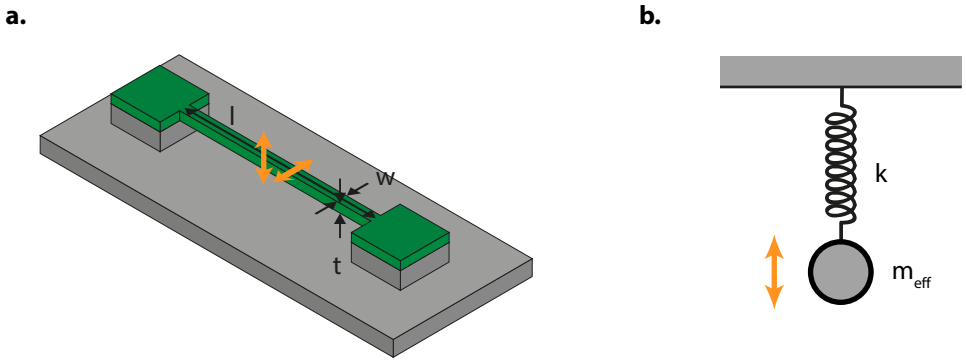

Figure 8.1: **a.** Illustration of a nanomechanical string resonator of length l, width w and thickness t. Its in-plane and out-of-plane vibrational modes are indicated by the orange arrows. **b.** A simple, 1D *mass-on-a-spring* model of a harmonic oscillator with effective parameters mass m_{eff} and stiffness k, offering a simplified description for the center of mass motion of nanostring resonators.

A nanostring resonator, as illustrated in Fig. 8.1a, is formed by a freely suspended *string*, which is clamped to an underlying substrate on both ends. Although it naturally constitutes a three-dimensional body, its motion can be theoretically treated as a one-dimensional, damped, harmonic oscillator[1] for most intents and purposes. Conveniently, by introducing substitute

[1] For a full derivation validating this model, please refer to [115, 116] or other works concerning Euler-Bernoulli beam theory.

parameters like the effective mass m_{eff}, stiffness k and damping rate Γ_{m}, the description can be reduced to a single degree of freedom per vibrational mode, as shown in Fig. 8.1b. Note that nanostring resonators exhibit a multitude of different modes (transversal, torsional etc.), but since they can be considered uncoupled, each mode can be treated independently. For this thesis we will limit the discussion to the in-plane and out-of-plane vibrational modes (as visualized in Fig. 8.1a), which are most accessible in experiments, and neglect any other modes. Proceeding with this model, we can describe each mode's center of mass motion as an independent one-dimensional harmonic oscillator governed by the equation

$$\ddot{x}(t) + \Gamma_{\text{m}}\dot{x}(t) + \frac{k}{m_{\text{eff}}}x(t) = \frac{F_0}{m_{\text{eff}}}\exp(-i\Omega t) \tag{8.1}$$

with the displacement x and an added, coherent driving force with the frequency Ω. Solving this differential equation using the Ansatz $x(t) = x_0 \exp(-i\Omega t)$, a complex solution can be found:

$$x_0 = \frac{F_0/m_{\text{eff}}}{(\Omega_{\text{m}}^2 - \Omega^2) - i\Omega_{\text{m}}\Gamma} \tag{8.2}$$

defining the angular[2] resonance frequency $\Omega_{\text{m}} = \sqrt{k/m_{\text{eff}}}$. We can further introduce the *quality factor* $Q = \Omega_{\text{m}}/\Gamma_{\text{m}}$, a measure of the loss rate of a resonator in relation to its stored energy. Since experimental setups are commonly sensitive to the squared magnitude of the displacement x_0, an amplitude spectrum can be described by

$$|x_0|^2 = \frac{F_0^2/m_{\text{eff}}^2}{(\Omega_{\text{m}}^2 - \Omega^2)^2 + \Gamma_{\text{m}}^2\Omega^2} \approx \left(\frac{F_0/m_{\text{eff}}}{2\Omega}\right)^2 \frac{1}{(\Omega_{\text{m}} - \Omega)^2 + \Gamma_{\text{m}}^2/4} \tag{8.3}$$

where the right hand side approximation assumes $\Gamma_{\text{m}} \ll \Omega_{\text{m}}$. This condition is usually well satisfied for nanostring resonators, especially for the high-Q strings studied in this thesis. Notably, in the approximation, Eq. 8.3 corresponds to an Lorentzian lineshape.

The effective mass m_{eff} in the formulas is a necessary correction since the calculated center of mass motion does not take into account any asymmetry in the cross-section of the string and which part of its mass contributes to the oscillations. For an exact calculation the string's geometry, boundary conditions and even specific mode shapes have to considered [117]. However, in the limit of highly tensile-stressed nanostrings, the effective mass can be well approximated to $m_{\text{eff}} = 0.5m$ [118] using the physical mass of the string $m = \rho lwt$ (l, w and t as in Fig. 8.1).

In the same high-stress limit, the angular resonance frequency of a nanostring's vibrational mode can be approximated to [119]

$$\Omega_{\text{m},n}^{\text{HTS}} = \frac{n\pi}{l}\sqrt{\frac{\sigma_0}{\rho}} \tag{8.4}$$

with the pre-stress σ_0 and density ρ of the material of the string and the mode index n. While this approximation is sufficient for most calculations, it can be shown that its accuracy can be

[2] Note that, throughout this thesis, formulas generally contain angular frequencies Ω, which are related to the (bare) frequencies f, which are usually measured in experiments, via $f = \Omega/2\pi$.

improved by applying a first order correction based on bending effects in the string [118]:

$$\Omega_{\mathrm{m},n}^{\mathrm{TS}} = \Omega_{\mathrm{m},n}^{\mathrm{HTS}} \frac{l\sqrt{\sigma_0 wt}}{l\sqrt{\sigma_0 wt} - 2\sqrt{EI}}. \tag{8.5}$$

Equation 8.5 requires knowledge of the material's Young's modulus E and the moment of inertia I of the investigated mode, which is found to be $I_{\mathrm{ip}} = w^3 t/12$ for in-plane and $I_{\mathrm{oop}} = wt^3/12$ for out-of-plane modes [120], using the width w and thickness t of the string. The corrected equation holds for typical tensile stressed nanostrings with $\sigma_0^2 wt \gg 2EI\rho\Omega^2$.

Lastly, it should be noted that, even in absence of an externally applied driving force, oscillatory motion can be observed in mechanical resonators. This *Brownian motion* is driven by thermal energy present in the system and can be used to connect the read-out signal of an experiment (e.g. the voltage) to a corresponding mechanical displacement. To this end, we use the equipartition theorem [121] to quantify the thermal driving force $F_{\mathrm{th}}^2(\Omega_{\mathrm{m}}) = 2m_{\mathrm{eff}}\Gamma_{\mathrm{m}}k_B T$ [122] and calculate the thermal amplitude spectrum of a mechanical resonator [122, 123]

$$S_{xx}(\Omega) = \frac{k_B T}{2\Omega_{\mathrm{m}}^2 m_{\mathrm{eff}}} \frac{\Gamma_{\mathrm{m}}}{(\Omega - \Omega_{\mathrm{m}})^2 + (\Gamma_{\mathrm{m}}/2)^2} \tag{8.6}$$

given in units of m^2/Hz with k_B being the Boltzmann constant. We will use Eq. 8.6 in Chap. 11 to calibrate our experimental data in terms of displacement amplitudes.

8.1.2 Coupling Two Harmonic Oscillators

Having established the harmonic oscillator model used to describe the nanostring resonators in this thesis, we want to extend the discussion to the interplay of multiple resonators in a network, i.e. the mechanical coupling of harmonic oscillators. Remaining in the model system, we begin with one of the simplest forms of inter-resonator coupling and consider the linear interaction of two masses and three springs as illustrated in Fig. 8.2. Each mass $m_{\mathrm{A,B}}$, along with its

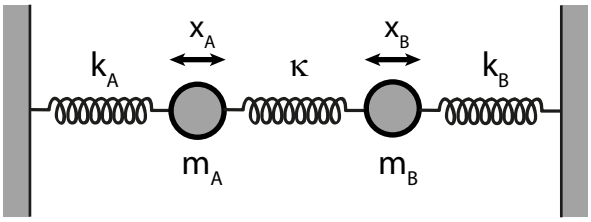

Figure 8.2: Illustration of a simple model system for the coupling of two 1D harmonic oscillators. Each mass $m_{\mathrm{A,B}}$ is affixed to a wall by a spring with stiffness k_{A} or k_{B} respectively. Additionally, the masses are connected to each other by a third spring with stiffness κ, causing their equations of motion to become coupled.

corresponding stiffness $k_{\mathrm{A,B}}$ represents a one dimensional harmonic oscillator as discussed above, while the third spring with stiffness κ introduces a cross-dependency between their displacements. As such, we formulate an equation of motion for each one of the oscillators, recalling Eq. 8.1, but neglecting external forces and damping, which simplifies the discussion and allows us to

focus on the eigenfrequencies.

$$\begin{aligned} -k_\mathrm{A}x_\mathrm{A} + \kappa(x_\mathrm{B} - x_\mathrm{A}) &= m_\mathrm{A}\ddot{x}_\mathrm{A} \\ -k_\mathrm{B}x_\mathrm{B} + \kappa(x_\mathrm{A} - x_\mathrm{B}) &= m_\mathrm{B}\ddot{x}_\mathrm{B} \end{aligned} \tag{8.7}$$

In the model geometry, the sign of the inter-resonator coupling κ can be intuitively understood to be positive, since a displacement of mass A relative to mass B in positive x-direction must lead to a positive force acting on mass B. We will later discuss how the simple coupling assumed in Eq. 8.7 describes the situation in the experiment.
We assume harmonic solutions of the form $x_m(t) = x_m^0 \exp(i\Omega_\pm t)$, with the index ($m$ = A,B) referring to the corresponding mass, and obtain

$$\begin{pmatrix} \tilde{\Omega}_\mathrm{A}^2 & -\frac{\kappa}{m_\mathrm{A}} \\ -\frac{\kappa}{m_\mathrm{B}} & \tilde{\Omega}_\mathrm{B}^2 \end{pmatrix} \begin{pmatrix} x_\mathrm{A}^0 \\ x_\mathrm{B}^0 \end{pmatrix} = \Omega_\pm^2 \begin{pmatrix} x_\mathrm{A}^0 \\ x_\mathrm{B}^0 \end{pmatrix}, \tag{8.8}$$

defining $\tilde{\Omega}_m = \sqrt{(k_m + \kappa)/m_m}$. We recognize the presentation as an eigenvalue equation and solve it for $\Omega_\pm^2$, obtaining the two *normal modes* of the coupled system

$$\Omega_\pm^2 = \frac{1}{2}\left[\tilde{\Omega}_\mathrm{A}^2 + \tilde{\Omega}_\mathrm{B}^2 \pm \sqrt{(\tilde{\Omega}_\mathrm{A}^2 + \tilde{\Omega}_\mathrm{B}^2)^2 + 4g^2\tilde{\Omega}_\mathrm{A}\tilde{\Omega}_\mathrm{B}}\right] \tag{8.9}$$

with $g^2 = \kappa^2/(m_\mathrm{A}m_\mathrm{B}\tilde{\Omega}_\mathrm{A}\tilde{\Omega}_\mathrm{B})$.

Since we investigate networks of nominally identical nanostrings in this thesis, only differing by small factors due to fabrication, we focus on studying coupled resonators with $m_\mathrm{A} = m_\mathrm{B} \equiv m$, $k_\mathrm{A} \equiv k$ and $k_\mathrm{B} = k + \Delta k$ with $\Delta k \ll k$, which allows us to approximate

$$g^2 \approx \kappa^2/(mk). \tag{8.10}$$

The behavior of the two normal modes Ω_+ and Ω_- for a varying detuning Δk is illustrated in Fig. 8.3. We see that for $|\Delta k| \gg \kappa$, the resulting frequencies are barely affected by the inter-resonator coupling κ and $\Omega_\pm \approx \tilde{\Omega}_\mathrm{A,B}$. By decreasing the detuning to $|\Delta k| \approx \kappa$ on the other hand, we observe an increased hybridization of modes in the coupled system, which in turn modifies the observed eigenfrequencies significantly. Finally, for $\Delta k = 0$ the mode-splitting becomes exactly $\Omega_+ - \Omega_- = g$, a fact that is commonly exploited in order to extract inter-resonator coupling rates from avoided crossings observed in measurements (see Sec. 11.2.2 and e.g. Refs. [102, 105, 110]).

8.1.3 General Description of N Coupled Oscillators

We now want to demonstrate that the above treatment of two coupled harmonic oscillators can be easily expanded to a larger network consisting of an arbitrary number of resonators. However, we will restrict the discussion to certain key aspects and refer the reader to Ref. [124] for an in-depth derivation and treatment of the *general coupled oscillator problem.*

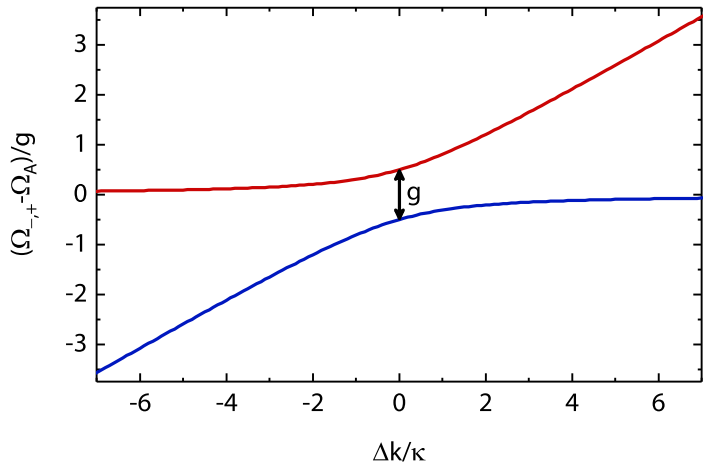

Figure 8.3: Normal mode frequencies $\Omega_\pm$ as a function of the detuning Δk, calculated according to Eq. 8.9. Due to the finite inter-resonator coupling κ, the normal modes of the system hybridize and an avoided crossing can be observed. For $\Delta k = 0$, i.e. two resonators exactly on resonance, the mode-splitting $\Omega_+ - \Omega_-$ minimizes to g.

Recalling Eq. 8.7, it can be understood that the general equation of motion for a harmonic oscillator with index $n \in [1,N]$ and mass m_n[3] in a network of N resonators can be written as [124]

$$m_n \ddot{x}_n = F_n = -\kappa_{nn} x_n + \sum_{i \neq n}^{N} \kappa_{ni}(x_i - x_n), \tag{8.11}$$

again neglecting the damping and defining κ_{ni} as the coupling between resonators n and i for $i \neq n$ (i.e. the stiffness of the connecting spring in the model), and its own effective stiffness for $i = n$. We now introduce a *generalized stiffness* k_{ij}, defined as

$$k_{ij} = \frac{\partial F_i}{\partial x_j}, \tag{8.12}$$

which allows us to write the N linear, homogenous differential equations that arise from Eq. 8.11 concisely in the matrix form

$$\mathbf{M}\ddot{\vec{\mathbf{x}}} = \mathbf{K}\vec{\mathbf{x}}, \tag{8.13}$$

defining the *mass matrix* $\mathbf{M}$, *stiffness matrix* $\mathbf{K}$ and displacement vector $\vec{\mathbf{x}}$

$$\mathbf{M} = \begin{pmatrix} m_1 & 0 & \dots & 0 \\ 0 & m_2 & \dots & 0 \\ \vdots & 0 & \ddots & \vdots \\ 0 & \dots & 0 & m_n \end{pmatrix}, \quad \mathbf{K} = \begin{pmatrix} k_{11} & k_{12} & \dots & k_{1n} \\ k_{21} & k_{22} & \dots & k_{2n} \\ \vdots & \vdots & \ddots & \vdots \\ k_{n1} & \dots & \dots & k_{nn} \end{pmatrix}, \quad \vec{\mathbf{x}} = \begin{pmatrix} x_1 \\ x_2 \\ \vdots \\ x_n \end{pmatrix}. \tag{8.14}$$

[3] For clarity, we will employ numeric instead of alphabetic indices for the discussion of the generalized problem, i.e. $x_\mathrm{A} \equiv x_1$,$k_\mathrm{AB} \equiv k_{12}$ etc.

Note that since the inter-resonator coupling is bi-directional, we can require $k_{ij} = k_{ji}$, making $\mathbf{K}$ a symmetric matrix. As above, we now assume solutions of the form $x_n(t) = x_n^0 \exp(i\Omega t)$ and subsequently produce an eigenvalue equation for Ω^2 and the eigenvector $\vec{\mathbf{x}}_0 = \left(x_1^0 \dots x_n^0\right)^T$ that can be written as

$$-\Omega^2 \mathbf{M}\vec{\mathbf{x}}_0 = \mathbf{K}\vec{\mathbf{x}}_0. \tag{8.15}$$

Equation 8.15 is a *generalized Eigenvalue problem* that can be solved for exactly N eigenvalues Ω_λ (which do not have to be distinct) and up to N corresponding, linearly independent eigenvectors $\vec{\mathbf{x}}_{0,\lambda}$. Each pair $(\Omega_\lambda, \vec{\mathbf{x}}_{0,\lambda})$ with $\lambda \in [1 \dots N]$ forms one oscillatory *normal mode* of the coupled system. However, since $\mathbf{K}$ is real and symmetric and $\mathbf{M}$ is real and positive-definite, basic theorems of linear algebra [125] tell us that the problem can be decomposed to an ordinary eigenvalue problem that will result in exactly N distinct normal mode solutions of the system.

Problems of this kind arise regularly in a wide variety of engineering and scientific applications and algorithms to find their solutions as efficient as possible have been studied extensively (cf. e.g. Ref. [126]). Therefore, by describing multi-resonator networks in the above matrix form, the normal modes of even very large networks can be quickly calculated with widely available numerical solver software (e.g. Mathematica, MATLab).

8.1.4 Independent Crossing Approximation

While we have shown above that it is comparatively easy to solve large resonator networks for their normal modes, calculating the inter-resonator coupling factors κ_{ij} from an observed mode splitting can become increasingly complex when considering the full system of equations. However, as seen in Fig. 8.3, the influence of inter-resonator coupling on the eigenfrequencies of the coupled modes is actually largely confined to a small area with $|\Delta k| \approx \kappa_{ij}$, while the normal modes otherwise remain close to the undisturbed eigenfrequencies of the resonators. Based on this observation, we want to proof in the following lines that, for all resonators investigated in this thesis, it is in fact sufficient to treat the two modes directly involved in the avoided crossing as an independent two-level system, as long as all other modes are far enough detuned.

To this end, we start by considering a network of three nominally identical resonators with $m_1 = m_2 = m_3 \equiv m$. We further assume uniform coupling across the network, i.e. $k_{13} = k_{12} = k_{23} \equiv \kappa$, which implies $k_{11} = k_{22} \equiv -(k + 2\kappa)$, and set $k_{33} \equiv -(k + 2\kappa + \Delta k)$. This corresponds to two resonators on resonance (i.e. at the center of an avoided crossing), both separated by a finite detuning Δk from the third.

Solving Eq. 8.15 for these values, we obtain the three normal mode frequencies of the coupled system

$$\Omega_1^2 = \frac{k + 3\kappa}{m}, \quad \Omega_{2,3}^2 = \frac{2k + \Delta k + 3\kappa \mp \sqrt{\Delta k^2 + 2\Delta k\kappa + 9\kappa^2}}{2m}. \tag{8.16}$$

Now, for large frequency detunings $\Delta \gg \kappa$, the expression for Ω_2[4] can be approximated to

$$\begin{aligned}\Omega_2 &= \sqrt{\frac{2k + \Delta k + 3\kappa - \sqrt{\Delta k^2 + 2\Delta k\kappa + 9\kappa^2}}{2m}} \\ &\approx \sqrt{\frac{2k + \Delta k + 3\kappa - \sqrt{(\Delta k + \kappa)^2}}{2m}} = \sqrt{\frac{k+\kappa}{m}}.\end{aligned} \tag{8.17}$$

Subsequently, we can calculate the mode-splitting on resonance between the hybridized modes Ω_1 and Ω_2 to

$$\begin{aligned}\Omega_1 - \Omega_2 &= \sqrt{\frac{k+3\kappa}{m}} - \sqrt{\frac{k+\kappa}{m}} = \sqrt{\frac{k}{m}(1+3\kappa/k)} - \sqrt{\frac{k}{m}(1+\kappa/k)} \\ &\approx \sqrt{\frac{k}{m}}\left(1 + \frac{1}{2}(3\kappa/k)\right) - \sqrt{\frac{k}{m}}\left(1 + \frac{1}{2}(\kappa/k)\right) = \frac{\kappa}{\sqrt{mk}}\end{aligned} \tag{8.18}$$

where we used an approximation of the square root valid for $\kappa \ll k$, finally arriving at the same expression as in Eq. 8.10.

In other words, the observed mode-splitting g between the two crossing resonators is not significantly altered by the presence of a third resonator in the same network as long as the latter's eigenfrequency is far enough detuned (i.e. $|\Delta k| \gg \kappa$). It should be noted that while the analytic approximation above assumes uniform coupling across the network, it can be shown (e.g. numerically) that it holds for differences in κ, e.g. $\kappa_{13} = \kappa_{23} + \Delta\kappa$, as long as $\Delta\kappa \ll \Delta k$. Therefore, in the majority of scenarios where avoided crossing are analyzed individually (see Sec. 11.2.2), it is a viable approach to consider the crossings independent and extract the inter-resonator coupling rates κ_{ij} using Eq. 8.10.

8.2 Transition Dynamics in Multi-Level Systems

The Landau-Zener model [127, 128] provides a description for time dependent transition dynamics in strongly coupled quantum two-level systems. In particular it can be used to predict the outcome of a system's passage through an avoided crossing, where the model describes the tunneling of quantum mechanical excitations from one state to another. Coupled mechanical resonators, while still in the domain of classical physics, have been shown [99, 129, 130] to form an equivalent two-level system and adhere to the same formulas presented by Landau and Zener. Therefore, the model can be used to describe the dynamics of excitation transfer from one mechanical resonator to another [103, 131]. In the following section, we will introduce the original Landau-Zener formulas, discuss the resulting transition dynamics in two-level systems, and subsequently extend the discussion to systems comprised of three (or more) levels, like the three-resonator networks investigated in this thesis.

[4] Looking at Eq. 8.16, it becomes clear that the avoided crossing occurs between Ω_1 and either Ω_2 or Ω_3, depending on the sign of Δk. Without loss of generality we perform the calculation for Ω_2.

8.2.1 The Landau-Zener Formula

The original problem investigated by Landau and others concerns the time evolution of a quantum mechanical system described by the time-dependent Schrödinger equation [132]

$$i\hbar \begin{pmatrix} \dot{\Psi}_\mathrm{A} \\ \dot{\Psi}_\mathrm{B} \end{pmatrix} = \mathbf{H}(t) \begin{pmatrix} \Psi_\mathrm{A} \\ \Psi_\mathrm{B} \end{pmatrix} \tag{8.19}$$

with the time-dependant Hamiltonian operator

$$\mathbf{H}(t) = \begin{pmatrix} e_\mathrm{A} + \beta_\mathrm{A} t & v \\ v & e_\mathrm{B} + \beta_\mathrm{B} t \end{pmatrix}. \tag{8.20}$$

From a physical standpoint, the equation corresponds to a system of two *states* or *levels* with undisturbed energies of $E_m(t) = e_m + \beta_m t$ (m = A,B) that exhibit a linear time-dependence β_m and are coupled to each other by the off-diagonal elements v. The squared wave function $|\Psi_m|^2$ represents the probability for the system to be found in state m.

For $\beta_\mathrm{A} \neq \beta_\mathrm{B}$ the system will eventually develop to a point in time t_c where the undisturbed energy levels cross (i.e. $E_\mathrm{A}(t_\mathrm{c}) = E_\mathrm{B}(t_\mathrm{c}) \equiv E_\mathrm{c}$), making transitions between the states possible for $|v| > 0$. Calculating the eigenvalues of the Hamiltonian in this case, we obtain $\lambda_{+,-} = E_\mathrm{c} \pm v$, showing that an avoided crossing of $\lambda_+ - \lambda_- = 2v$ is formed. At this point, it becomes clear that the system of mechanically coupled oscillators discussed in Sec. 8.1.2 does indeed behave equivalently to this quantum mechanical two-level system, with each normal-mode $\Omega_\pm$ corresponding to one energy *state* of the system.

During the passage through an avoided crossing, tunneling processes can lead to the transfer of excitation from one state to the other. The Landau-Zener model quantifies this process and gives an expression for the transition probability [128]

$$P_\mathrm{diab} = \exp\left(\frac{-2\pi v^2}{\zeta}\right), \tag{8.21}$$

introducing $\zeta = |\beta_\mathrm{A} - \beta_\mathrm{B}|$ as the relative time dependency or *passage rate*. P_diab is defined as the probability that a system prepared in a certain state at the start of time evolution (e.g. $|\Psi_\mathrm{A}(t \to -\infty)|^2 = 1$) passes through the crossing *diabatically* and is found in a different state at the end (e.g. $|\Psi_\mathrm{A}(t \to -\infty)|^2 = 0$). Notably, the probability depends only on the coupling term v and the rate ζ at which the energy of the levels change relative to each other, not the energy itself. Analyzing Eq. 8.21, it can be seen that for slow transitions (i.e. small ζ), the transition probability is also small. This adheres to the *adiabatic theorem*, which postulates that in the limit of slow passage ($\zeta \to 0$) the probability for the system to leave its current state must become exponentially small [133, 134], thus the crossing is passed *adiabatically*. Necessarily, in a system comprised of only two states, this scenario exhibits an inverse probability $P_\mathrm{adiab} = 1 - P_\mathrm{diab}$. The different modes of passage through the crossing are further illustrated in Fig. 8.4.

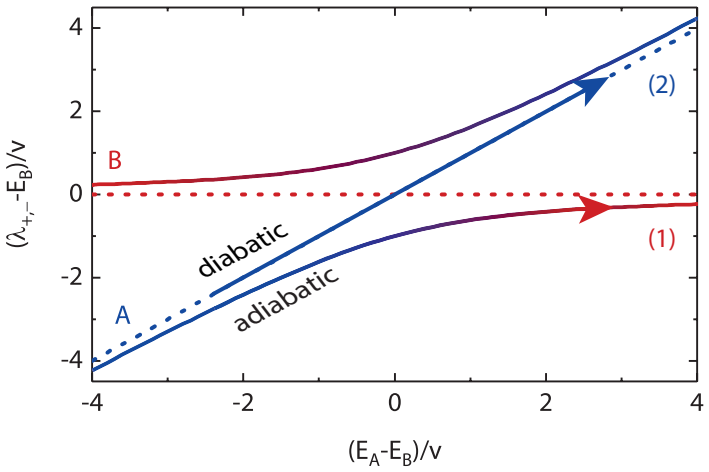

Figure 8.4: Illustration of Landau-Zener dynamics at an avoided crossing of a two-level system as defined in Eq. 8.20, calculated for a coupling of $v = 0.2E_\mathrm{B}$. If the passage through the crossing is performed slowly (i.e. small passage rate ζ), the system follows the lower branch of the mode splitting and ends up in state (1), i.e., the transition is adiabatic. For fast passage rates ζ, the system passes through the crossing diabatically without energy transfer and ends up in state (2).

The validity of the formula has been experimentally confirmed [135] and is since widely used in a variety of research fields (cf. e.g. [103, 136–138]).

8.2.2 Multi-Level Transitions

Analytic Solutions

Notably, while the Landau-Zener formula offers a strikingly simple model for transition dynamics in two-level systems, extending the discussion to systems with three or more levels turns out to be a highly challenging endeavor. In particular, already for a three-level system, defined by the Hamiltonian

$$\mathbf{H}(t) = \begin{pmatrix} e_\mathrm{A} + \beta_\mathrm{A} t & v_{12} & v_{13} \\ v_{12} & e_\mathrm{B} + \beta_\mathrm{B} t & v_{23} \\ v_{13} & v_{23} & e_\mathrm{C} + \beta_\mathrm{C} t \end{pmatrix}, \tag{8.22}$$

no explicit analytic solution can be found [132].
In an approximative approach, it is possible to consider all crossings in a system to be fully independent and treat more complex problems as a series of individual two-level crossings, eventually arriving at transition probabilities of the form

$$P_\mathrm{diab,n} = (P_\mathrm{diab})^n, \tag{8.23}$$

where $P_\mathrm{diab,n}$ is the probability for the system to pass through n successive crossings completely diabatically.

Furthermore, there exist several special cases, where some or all of the transition probabilities can be calculated analytically as long as certain conditions are fulfilled. These require e.g. for

all but one energy level to be constant in time (i.e. $\beta_B = \beta_C = 0$) and the crossed levels to be uncoupled (i.e. $v_{23} = 0$). For a detailed description of solvable n-level systems, please refer to Refs. [132, 139]. In this thesis, however, the investigated networks exceed the scope of the analytically solvable cases and we will instead introduce a set of differential equations, which can be solved numerically in order to model the transition dynamics of the networks.

Numerical Solution for Three-Level Systems

In the following we will briefly derive the differential equations used to model transition dynamics of three-resonator networks in response to the measurement protocol described in Sec. 11.3.1. Note that the following is an expansion of the model used in Ref. [105] to three-level systems and can easily be expanded further based on the general coupled oscillator treatment discussed in Sec. 8.1.3.

We begin with the equations of motion for the three coupled resonators according to Eq. 8.11 under addition of linear damping terms and an external driving force F_{drive}.

$$m_A\ddot{x}_A + m_A\Gamma_A\dot{x}_A + \kappa_{AA}x_A = \kappa_{AB}(x_B - x_A) + \kappa_{AC}(x_C - x_A) + F_{\mathrm{drive}} \tag{8.24}$$

$$m_B\ddot{x}_B + m_B\Gamma_B\dot{x}_B + \kappa_{BB}x_B = \kappa_{AB}(x_A - x_B) + \kappa_{BC}(x_C - x_B) + F_{\mathrm{drive}} \tag{8.25}$$

$$m_C\ddot{x}_C + m_C\Gamma_C\dot{x}_C + \kappa_{CC}x_C = \kappa_{AC}(x_A - x_C) + \kappa_{BC}(x_B - x_C) + F_{\mathrm{drive}} \tag{8.26}$$

In the following, as we are dealing with almost identical nanostrings, we will set $\Gamma_A = \Gamma_B = \Gamma_C \equiv \Gamma$ and $m_A = m_B = m_C \equiv m$. Without loss of generality, we assume nanostring A to be excited and controlled in the measurement. Thus, its eigenfrequency $\tilde{\Omega}_A$ is time dependent, being tuned upwards by an amount $\Delta\tilde{\Omega}_A$ in time τ. Therefore we describe $\tilde{\Omega}_A$ as a function of time as

$$\tilde{\Omega}_A(t) = \begin{cases} \tilde{\Omega}_A^0 & t < t_0 \\ \tilde{\Omega}_A^0 + \zeta(t - t_0) & t_0 \le t \le t_0 + \tau \\ \tilde{\Omega}_A^0 + \Delta\tilde{\Omega}_A & t \ge t_0 + \tau \end{cases} \tag{8.27}$$

using $\zeta = \Delta\tilde{\Omega}_A/\tau$. In the beginning of the measurement, nanostring A is excited by a short (t_p) pulse with an oscillatory force with the frequency $\tilde{\Omega}_A^0$. Since $t_p < t_0$, we can write $F_{\mathrm{drive}}(t) = F_0 \exp(i\Omega_A^0 t)\Theta(t_p - t)$ with the Heaviside step function $\Theta(t)$. Note that in the experiment, the driving force is applied globally via a piezoelectric actuator, so it affects the three nanostrings equally.

We now use the ansatz $x_m(t) = x_0 c_m(t) \exp\left(i\tilde{\Omega}_A(t)t\right)$ (m = A,B,C) in order to find solutions for the amplitude coefficients $c_m(t)$ with $|c_A|^2 + |c_B|^2 + |c_C|^2 = 1$ and re-introduce $\tilde{\Omega}_{B,C}^2 = k_{BB,CC}/m$ with the generalized stiffness k_{ij} from Eq. 8.12 as the (non-hybridized) resonance frequencies of resonators A and B. Note that we use the time dependant resonance frequency $\tilde{\Omega}_A(t)$ of nanostring A in the harmonic solution for all three equations of motion. This is possible since $\left|\tilde{\Omega}_A(t) - \tilde{\Omega}_{B,C}\right| \ll \tilde{\Omega}_{B,C}$ holds in general, and in particular $\tilde{\Omega}_A(t) = \tilde{\Omega}_{B,C}$ at the corresponding

avoided crossings, where the transfer of excitations takes place. We obtain

$$\ddot{c}_\mathrm{A} + G(t)\dot{c}_\mathrm{A} + (F(t) + \tilde{\Omega}_\mathrm{A}^2(t))c_\mathrm{A} = \frac{\kappa_\mathrm{AB}}{m}c_\mathrm{B} + \frac{\kappa_\mathrm{AC}}{m}c_\mathrm{C} + \frac{F_0}{mx_0}\Theta(t_\mathrm{p} - t) \tag{8.28}$$

$$\ddot{c}_\mathrm{B} + G(t)\dot{c}_\mathrm{B} + (F(t) + \tilde{\Omega}_\mathrm{B}^2)c_\mathrm{B} = \frac{\kappa_\mathrm{AB}}{m}c_\mathrm{A} + \frac{\kappa_\mathrm{BC}}{m}c_\mathrm{C} + \frac{F_0}{mx_0}\Theta(t_\mathrm{p} - t) \tag{8.29}$$

$$\ddot{c}_\mathrm{C} + G(t)\dot{c}_\mathrm{C} + (F(t) + \tilde{\Omega}_\mathrm{C}^2)c_\mathrm{C} = \frac{\kappa_\mathrm{AC}}{m}c_\mathrm{A} + \frac{\kappa_\mathrm{BC}}{m}c_\mathrm{B} + \frac{F_0}{mx_0}\Theta(t_\mathrm{p} - t), \tag{8.30}$$

defining the functions

$$F(t) = (i\dot{\tilde{\Omega}}_\mathrm{A}t + i\tilde{\Omega}_\mathrm{A})^2 + 2i\dot{\tilde{\Omega}}_\mathrm{A} + \Gamma(i\dot{\tilde{\Omega}}_\mathrm{A}t + i\tilde{\Omega}_\mathrm{A})$$
$$G(t) = 2i(i\dot{\tilde{\Omega}}_\mathrm{A}t + \tilde{\Omega}_\mathrm{A}) + \Gamma.$$

Note that, as the coupling rates are much smaller than the stiffness of the resonators (i.e. $\kappa_{ij} \ll k_{ii}\ \forall\ ((i,j) \in (\mathrm{A,B,C})^2 \wedge i \neq j)$, we assume the coefficients $c_m(t)$ to vary much slower in time than the oscillatory motion $\propto \exp\left(i\tilde{\Omega}_\mathrm{A}(t)t\right)$. Consequently, we neglect the second derivatives $\ddot{c}_m(t)$ in the Eqs. 8.28-8.30 and arrive at the final form of the equations:

$$G(t)\dot{c}_\mathrm{A} + (F(t) + \tilde{\Omega}_\mathrm{A}^2(t))c_\mathrm{A} = \frac{\kappa_\mathrm{AB}}{m}c_\mathrm{B} + \frac{\kappa_\mathrm{AC}}{m}c_\mathrm{C} + \frac{F_0}{mx_0}\Theta(t_\mathrm{p} - t) \tag{8.31}$$

$$G(t)\dot{c}_\mathrm{B} + (F(t) + \tilde{\Omega}_\mathrm{B}^2)c_\mathrm{B} = \frac{\kappa_\mathrm{AB}}{m}c_\mathrm{A} + \frac{\kappa_\mathrm{BC}}{m}c_\mathrm{C} + \frac{F_0}{mx_0}\Theta(t_\mathrm{p} - t) \tag{8.32}$$

$$G(t)\dot{c}_\mathrm{C} + (F(t) + \tilde{\Omega}_\mathrm{C}^2)c_\mathrm{C} = \frac{\kappa_\mathrm{AC}}{m}c_\mathrm{A} + \frac{\kappa_\mathrm{BC}}{m}c_\mathrm{B} + \frac{F_0}{mx_0}\Theta(t_\mathrm{p} - t). \tag{8.33}$$

A sketch of the algorithm to perform the numerical solution of Eqs. 8.31-8.33 can be found in App. A.10. The resulting model calculations are shown in Sec. 11.3 and provide good agreement with experimental results.

8.3 Non-Linear Response Regime

So far, we discussed the mechanical motion of nanostring resonators in the model of one-dimensional, harmonic oscillators with a fully linear equation of motion. However, in the case of real nanostrings, the geometry of a doubly clamped string can lead to the emergence of non-linear effects. In particular, as the string performs a transverse motion, the material stretches, causing additional stress. Considering only low amplitudes, i.e. much smaller than the width of the beam, these effects can be well neglected. However, in our experiments, the strings are regularly excited by strong external forces, causing the oscillation amplitudes to reach the order of the string's width. In the following, we will derive this *geometric non-linearity* and discuss how it affects the response of the nanostring. Notably, we will subsequently employ the non-linearity of highly excited nanostrings in order to derive a technique which allows for the all-mechanical tuning of the eigenfrequencies of nanostring resonators.

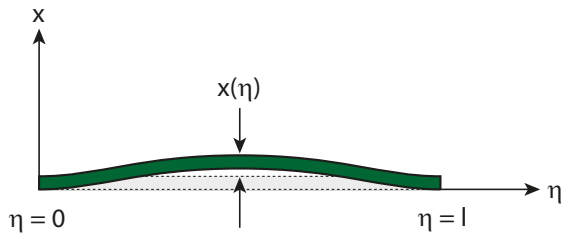

Figure 8.5: Schematic illustration of a nanostring resonator aligned along the axis of a coordinate η. The displacement profile of the string's vibrational modes is described by $x(\eta)$, which takes the form of Eq. 8.34 in the limit of high tensile stress. The figure is adapted from Ref. [118].

8.3.1 Geometric Non-Linearity

We start by considering a nanostring resonator aligned along the axis of a coordinate η, as illustrated in Fig. 8.5. For highly tensile stressed strings, the displacement profile $x(\eta)$ (i.e. the mode-shape) of its vibrational modes is given by the expression [120]

$$x(\eta) = x_{0,n} \sin\left(n\pi\eta/l\right), \quad 0 \leq \eta \leq l, \tag{8.34}$$

where $x_{0,n}$ is the displacement at the center of the string for the mode index n.
Therefore, a center displacement $x_{0,n} > 0$ leads to an elongation of the string according to

$$l' = \int_0^l \sqrt{1 + \left(\frac{\mathrm{d}}{\mathrm{d}\eta}x(\eta)\right)^2}\, d\eta \approx \int_0^l \left[1 + \frac{1}{2}\left(\frac{\mathrm{d}}{\mathrm{d}\eta}x(\eta)\right)^2\right] d\eta = l\left(1 + \frac{n^2 x_{0,n}^2 \pi^2}{4l^2}\right), \tag{8.35}$$

which can be translated into an increase in the tensile stress σ along the string using the Young's modulus E of the material [140]

$$\sigma = \sigma_0 + E\frac{l' - l}{l} = \sigma_0 + \frac{n^2 x_{0,n}^2 \pi^2 E}{4l^2}. \tag{8.36}$$

Substituting the altered stress into the equation of motion for a highly tensile stressed nanostring [115, 119]

$$\ddot{x}(t) + \Gamma_{\mathrm{m},n}\dot{x}(t) + \left(\frac{n\pi}{l}\right)^2 \frac{\sigma}{\rho} x(t) = \frac{F_0}{m_{\mathrm{eff}}} \exp(-i\Omega t), \tag{8.37}$$

introduces a non-linear term proportional to $x^3(t)$ and results in

$$\ddot{x}(t) + \Gamma_{\mathrm{m},n}\dot{x}(t) + \Omega_{\mathrm{m},n}^2 x(t) + \alpha_n x^3(t) = \frac{F_0}{m_{\mathrm{eff}}} \exp(-i\Omega t). \tag{8.38}$$

Equation 8.38 represents the standard form of a *Duffing oscillator* [141, 142], using the expression from Eq. 8.4 for the angular resonance frequency of the mode $\Omega_{\mathrm{m},n}$ and defining the non-linearity or *Duffing parameter* as

$$\alpha_n = \frac{n^4 \pi^4 E}{4l^4 \rho}. \tag{8.39}$$

The amplitude spectrum of such an oscillator's vibrational mode with index n, linear damping $\Gamma_{\mathrm{m},n}$ and resonance frequency $\Omega_{\mathrm{m},n}$ is found to be described by the implicit equation [142]

$$\left[\Gamma_{\mathrm{m},n}^2 + 4\left(\Omega - \Omega_{\mathrm{m},n} - \frac{3}{8}\frac{\alpha_n}{\Omega_{\mathrm{m},n}}x_{0,n}^2\right)^2\right]x_{0,n}^2 = \frac{F_0}{m_{\mathrm{eff}}\Omega_{\mathrm{m},n}^2}, \tag{8.40}$$

which corresponds to a Lorentzian shaped response function for low driving powers, where the geometric non-linearity remains negligible. However, for increasing drive powers, we observe a more complex behavior, as illustrated in Fig. 8.6.

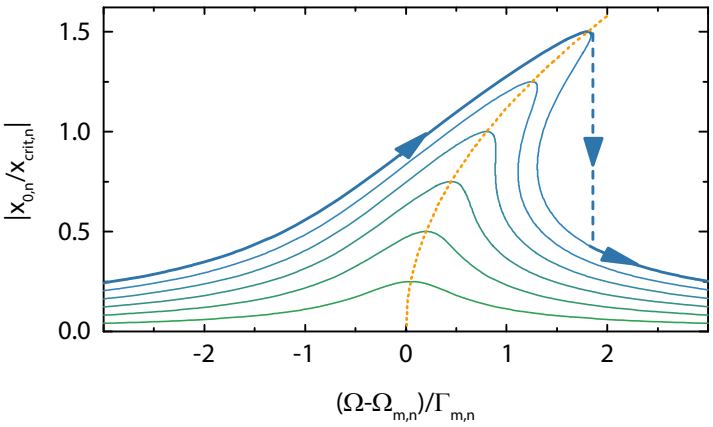

Figure 8.6: Theoretical amplitude spectrum of a *Duffing oscillator* according to Eq. 8.40 for increasing drive powers (bottom to top). Above a critical amplitude $x_{\mathrm{crit},n}$, the response spectrum becomes bistable. The blue arrows illustrate a frequency sweep from left to right, following the high-amplitude path of the hysteresis until the bistability breaks down at the effective resonance frequency $\Omega_{\mathrm{eff},n}$. The orange dotted line corresponds to the *backbone curve* given in Eq. 8.41 connecting the amplitude maxima to $\Omega_{\mathrm{eff},n}$. The figure is adapted from Ref. [118].

In particular, the point of maximum displacement $x_{0,n,\mathrm{max}}^2$ is shifted towards an increased, effective resonance frequency $\Omega_{\mathrm{eff},n} \geq \Omega_{\mathrm{m},n}$ according to [142]

$$x_{0,n,\mathrm{max}}^2 = \frac{8}{3}\frac{\Omega_{\mathrm{m},n}}{\alpha_n}(\Omega_{\mathrm{eff},n} - \Omega_{\mathrm{m},n}), \tag{8.41}$$

which is called the *backbone curve* of the oscillator (see the orange dashed line in Fig. 8.6). Furthermore, for driving forces that are sufficient to cause the resonator to exceed a critical amplitude of $x_{0,n} \geq x_{\mathrm{crit},n} = (\frac{4}{3})^{3/2}\sqrt{\Gamma_{\mathrm{m},n}\Omega_{\mathrm{m},n}/\alpha_n}$, a bistability of the response spectrum emerges, forming two stable and one metastable state, which is not accessible experimentally. By performing a continuous upwards sweep of the drive frequency, the spectrum follows the high amplitude solution until the bistability breaks down for frequencies $\Omega > \Omega_{\mathrm{eff},n}$ (dashed blue line in Fig. 8.6). Similarly, a downwards frequency sweep can be performed to investigate the lower branch of the hysteretic amplitude spectrum. Since both $x_{0,n,\mathrm{max}}$ and $\Omega_{\mathrm{eff},n}$ depend

on the amplitude of the external drive F_0, information about the non-linearity of a device can be gained by analyzing amplitude spectra for varying drive powers, which we will use in Sec. 11.1.2.

For a more comprehensive derivation and discussion of *Duffing oscillators*, please refer to Refs. [116, 142, 143] and the sources therein.

8.3.2 Eigenfrequency Tuning Mechanism

Notably, the additional stress that is induced into the material of the nanostring by high amplitude motion is not confined to the mode that performs the oscillations. Instead, it affects every possible mode exhibited by the driven nanostring, individually shifting the resonance frequency of each. In the following, we want to quantify how the resonance frequency of the fundamental mode of a nanostring $\Omega_{m,n=1} \equiv \Omega_m$ changes due to the high amplitude oscillations of one of its higher harmonics $\Omega_{m,n>1}$.

We begin by recalling the effect of an elongation Δl on the pre-stress σ_0 of a nanostring resonator (cf. Eq. 8.36)

$$\sigma' = \sigma_0 + \Delta\sigma = \sigma_0 + E\frac{\Delta l}{l} \tag{8.42}$$

and substituting the modified pre-stress σ' into the expression for the fundamental mode ($n = 1$) frequency from Eq. 8.4

$$\Omega'_m = \frac{\pi}{l}\sqrt{\frac{\sigma'}{\rho}} \approx \Omega_m\left(1 + \frac{\Delta\sigma}{2\sigma_0}\right). \tag{8.43}$$

To determine the elongation Δl, we time-average the expression derived in Eq. 8.35 under assumption of a harmonic time-dependency (i.e. $x(t) \propto \exp(i\Omega_{m,n}t)$) and receive

$$\Delta l = \langle l' - l \rangle = \frac{1}{2}\frac{n^2 x_{0,n}^2 \pi^2 E}{4l^2}. \tag{8.44}$$

Combining equations 8.42 and 8.43, we arrive at the relative eigenfrequency change of the fundamental mode

$$\frac{\Delta\Omega_m}{\Omega_m} = \frac{\Omega'_m - \Omega_m}{\Omega_m} = \frac{x_{0,n}^2}{4\sigma_0}\frac{n^2\pi^2 E}{4l^2}, \tag{8.45}$$

as a function of the amplitude of the higher order mode $x_{0,n}$, which is described by the amplitude spectrum of a duffing oscillator in Eq. 8.40.

Conveniently, the amplitude of the upper branch of the rather complex *Duffing* spectrum for a drive frequency $\Omega_{\text{aux}} > \Omega_{m,n}$ can be simplified to

$$x_{0,n,\max}^2 = \frac{8}{3}\frac{\Omega_{m,n}}{\alpha_n}(\Omega_{\text{aux}} - \Omega_{m,n}) \tag{8.46}$$

within the limits of the bistability region $x_{0,n}^3 \gg 4F_0/(3\alpha_n m_{\text{eff}})$ and $x_{0,n} \leq F_0/(\Gamma_{m,n} m_{\text{eff}} \Omega_{m,n})$ [105, 142]. Note that the expression is almost identical to Eq. 8.41, indicating that the *backbone* is actually a full description of the frequency to amplitude relation for the upper branch of a

duffing oscillator within the bistability region. Finally, by substituting Eq. 8.46 into Eq. 8.45 we obtain

$$\frac{\Delta\Omega_m}{\Omega_m} = \frac{2}{3}\frac{\Omega_{\text{aux}} - \Omega_{m,n}}{\Omega_{m,n}}. \tag{8.47}$$

connecting the auxiliary drive frequency to the shift in fundamental mode frequency. Notably, the expression is not only independent of the drive signal's power ($\propto F_0$), but the pre-factor is also independent of the mode index n.

Equation 8.47 shows that the geometric non-linearity of a nanostring resonator can be exploited to increase the eigenfrequency of its fundamental mode (and, in fact, any other mode[5]) by controlling the frequency Ω_{aux} of an auxiliary drive applied to the system. It is, however, important to note that the drive signal's power defines the size of the bistability region and thus the range of accessible frequencies. Furthermore, the drive frequency needs to be initialized at $\Omega^0_{\text{aux}} \approx \Omega_{m,n}$ and increased continuously towards the desired value of Ω_{aux} in order to access the upper branch of the hysteresis. We will make use of this *eigenfrequency tuning mechanism* extensively in Chap. 11. It should also be noted that geometric non-linearity is not a feature exclusive to nanostrings. Therefore, similar considerations should apply to many types of (nano)mechanical resonators, e.g. cantilevers.

[5] Since Eq. 8.4 shows that $\Omega_{m,n} = n \cdot \Omega_m$, Eq. 8.47 remains valid for arbitrary mode indices n in the high tensile stress approximation.

Chapter 9

Fabrication and Sample Design

In recent years, the fabrication of doubly clamped, nanomechanical string resonators made of Si_3N_4 has become a well established process at the WMI as well as the nanomechanics community as a whole [113, 144, 145]. As such, we will only briefly address the individual steps involved in the fabrication procedure and subsequently focus on the introduction and discussion of the resonator network designs that were fabricated and investigated in the scope of this thesis.

9.1 Fabrication Procedure

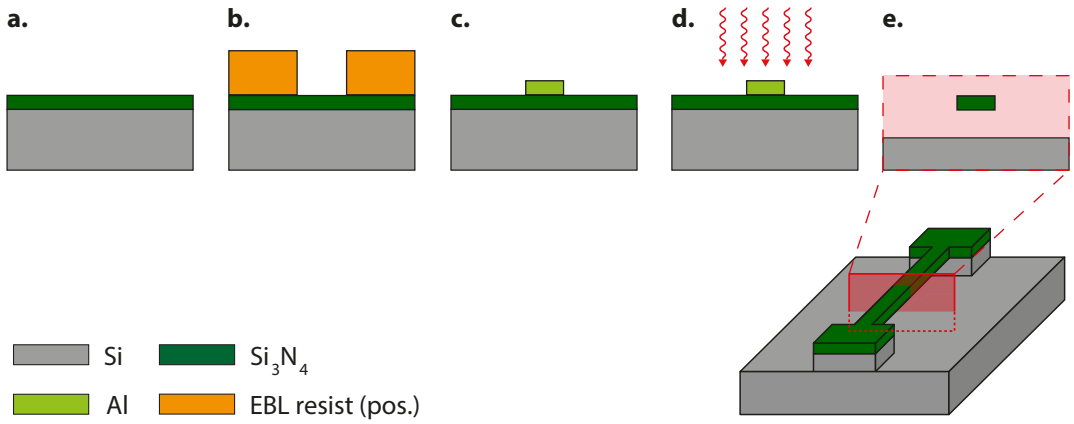

Figure 9.1: Schematic illustration of the thin film fabrication process of Si_3N_4 nanostring resonator networks. The individual steps are described in the main text.

Figure 9.1 illustrates the fabrication process of the Si_3N_4 nanostring resonators investigated in this thesis. **a.** Initially, the substrate is a commercially available silicon wafer covered with a 90 nm thick layer of tensile stressed Si_3N_4 by low pressure chemical vapor deposition (LPCVD). **b.** The substrate is coated with positive resist and structured using electron beam lithography (EBL), creating a mask in the shape of the clamps and string after development. **c.** Next, a 30 nm thick layer of Al is evaporated onto the sample and a lift-off in warm acetone is performed to remove the resist layer along with the excess Al. **d.** With the Al acting as an etch mask

for the Si_3N_4 , a sequence of anisotropic and isotropic reactive ion etching (RIE) processes first transfers the shape of the mask into the Si_3N_4/Si and subsequently releases the string from the substrate. **e.** Finally, the remainder of the Al mask is removed using a suitable remover and the sample is carefully dried using either a critical point dryer (CPD) or compressed N2, leaving the Si_3N_4 nanostring resonator freely suspended.

9.2 Resonator Network Designs

Due to the purely mechanical nature of the inter-resonator coupling investigated throughout this thesis, the geometric properties of the network design have an immense impact on the strength of the observed coupling and thus need to be thoroughly examined at the design-stage. Specifically, the small, partly under-etched, shared support that acts as a weak link and mediates the coupling between the two or more nanostrings it is connected to, must be carefully chosen regarding its shape as well as placement in the network. In the following, we will present the three resonator networks that have been investigated in this thesis, discussing the intentions behind the chosen design as well as their expected physical properties.

9.2.1 Tri Resonator Network (Series A)

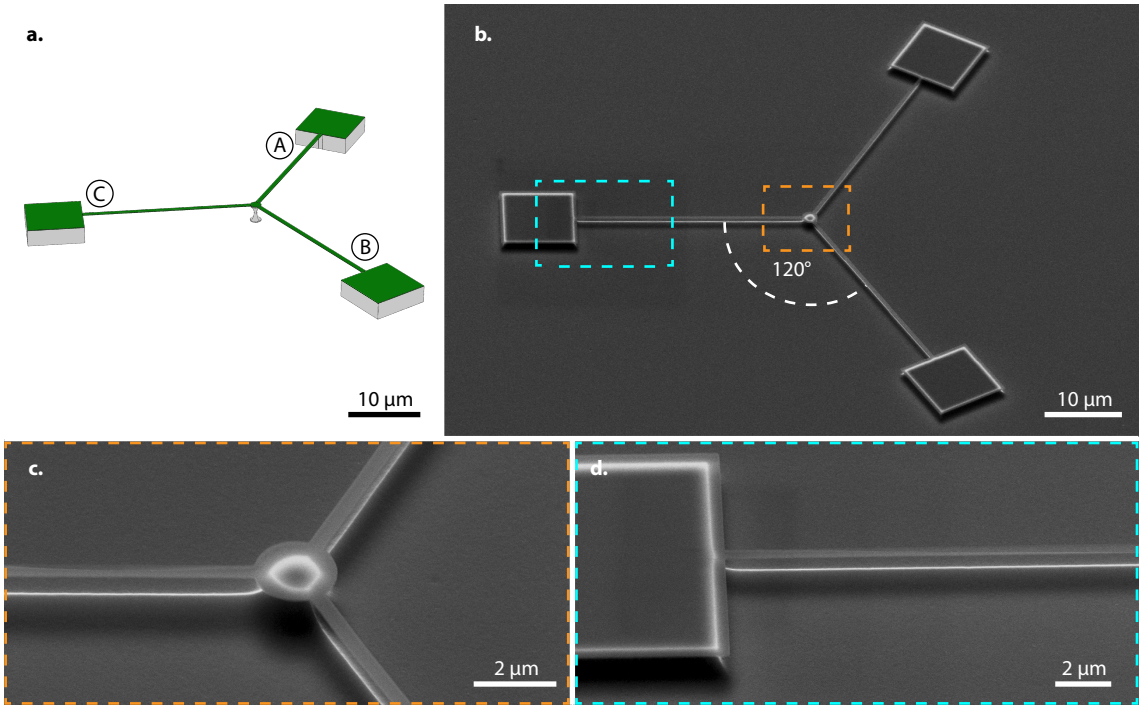

Figure 9.2: **a.** CAD model of a *Tri*-design (Series A) resonator network, consisting of three nanostring resonators with $(l, w, t) = (30 \cdot 10^3, 300, 90)$ nm, equally distributed around a circular shared support with $2\,\mu$m diameter. The individual strings are assigned letters alphabetically in clockwise order for future reference. **b.** Wide, angled (50°) Scanning Electron Microscopy (SEM) image of a fabricated Series A Tri-Resonator network. **c.** Zoom-in on the shared support structure that links the three resonators. **d.** Zoom-in on the clamp region, showing the freely suspended string as well as the under-etched clamp.

Figure 9.2 shows a 3D model (**a.**) and SEM images (**b-d.**) of a *Tri*-design (Series A) network. For this type of resonator network, three nominally identical nanostrings with $(l, w, t) = (30 \cdot 10^3, 300, 90)$ nm share a centrally placed, circular support with a diameter of $2\,\mu$m, each held aloft by a own square clamp ($10\text{x}10\,\mu\text{m}^2$) on the other end. The individual resonators are evenly placed around the shared support, forming a 120° angle between each of the strings. The zoom-ins in Fig. 9.2c-d show the freely suspended strings as well as the effect of the RIE step on the clamps and the circular support.

Based on the geometry chosen for this network design, it is possible to formulate a set of expectations regarding the behavior and strength of the inter-resonator coupling. In particular, since all of the resonators share the same support, we expect each resonator to be coupled to the two other resonators (i.e. $|\kappa_{\text{AB}}| > 0 \wedge |\kappa_{\text{AC}}| > 0$). Due to the equal spacing between the resonators and the resulting symmetry of the network, it further seems reasonable to assume equally strong coupling between any two resonators in the network (i.e. $\kappa_{\text{AB}} = \kappa_{\text{AC}} \equiv \kappa_{\text{BC}} = \kappa$). Finally, given the geometry of the shared support, one might intuitively expect a negative coupling $\kappa < 0$, i.e. a displacement of nanostring A in positive z-direction might *tilt* the circular support which in turn induces a force acting in negative z-direction on e.g. nanostring B. However, considering the small displacement amplitudes typically in the nanometer regime in comparison to the $2\,\mu$m wide support, this intuitive picture might not be applicable. Instead, the coupling could be primarily mediated by additional strain induced by a nanostring's motion into the shared support structure, which subsequently affects the other connected strings. Therefore, no well-founded prediction regarding the sign of the coupling can be made at this point. Notably, in a previous experiment with two coupled nanostrings placed in 180° angle a negative coupling constant was observed [105]. Recalling the matrix form of the eigenvalue equation 8.15 we can concisely summarize the the expected behavior of the network by forming its stiffness matrix:

$$\mathbf{K}_{\text{Tri,SA}} = \begin{pmatrix} k_{\text{AA}} & \kappa & \kappa \\ \kappa & k_{\text{BB}} & \kappa \\ \kappa & \kappa & k_{\text{CC}} \end{pmatrix} \tag{9.1}$$

9.2.2 Tri Resonator Network (Series B)

In Figure 9.3 a SEM image of a *Tri*-design (Series B) network is shown, featuring three nanostring resonators with $(l, w, t) = (30 \cdot 10^3, 140, 90)$ nm linked by a circular support ($\varnothing = 2\,\mu$m). Unlike in the previously discussed design, the resonators are not evenly spaced around the center support. Instead, two of the nanostrings form a 90° angle while the third is placed at an angle of 135° with respect to each of them. The sample design is equivalent to the series A design in all other aspects and will thus only be discussed in short. Due to the different distribution of the strings, one has to reconsider the assumptions made previously for series A regarding coupling strengths. Given the close proximity of the ends of resonators A and B, it appears highly likely that the strain induced on the shared support by the motion of resonator A will affect resonator B much more intensely in comparison to the farther distanced resonator C. Therefore, we assume

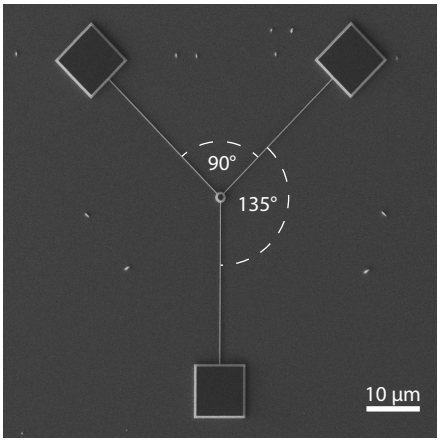

Figure 9.3: Scanning Electron Microscopy (SEM) image of a fabricated Series B Tri-Resonator network, consisting of three nanostring resonators with $(l, w, t) = (30 \cdot 10^3, 140, 90)$ nm. Unlike series A networks, the nanostrings are not evenly distributed, the different angles between the strings are highlighted. Aside from the altered distribution of strings and a smaller resonator width, the design is equivalent to series A.

$|\kappa_{\mathrm{AB}}| > |\kappa_{\mathrm{CA}}| = |\kappa_{\mathrm{CB}}|$ and write the expected stiffness matrix used in Eq. 8.15

$$\mathbf{K}_{\mathrm{Tri,SB}} = \begin{pmatrix} k_{\mathrm{AA}} & \kappa_+ & \kappa_- \\ \kappa_+ & k_{\mathrm{BB}} & \kappa_- \\ \kappa_- & \kappa_- & k_{\mathrm{CC}} \end{pmatrix}, \tag{9.2}$$

introducing $\kappa_{\mathrm{AB}} \equiv \kappa_+$ and $\kappa_{\mathrm{CA}} \equiv \kappa_-$ for simplicity.

9.2.3 Inline Resonator Network

The third and last network design investigated over the course of this thesis is the *Inline*-design presented in Fig. 9.4, showing a 3D model (**a.**) and SEM images of a fabricated sample (**b-d.**). The design consists of 3 or 4 nanostring resonators with the dimensions $(l, w, t) = (30 \cdot 10^3, 300, 90)$ being placed in line, each connected to its nearest neighbors via a circular support $2\,\mu$m in diameter, or stabilized by a clamp in the case of the outermost resonators.

The linear geometry of the inline-network should produce a significantly different coupling behavior within the network in comparison to the previously discussed Tri-networks. Specifically, due to the resonators being placed in line, no interaction between next-nearest-neighbors is expected in first order (i.e. $\kappa_{\mathrm{AC}} \approx 0$). Under the further assumption that nominally identical strings and supports result in identical coupling between each neighboring string, we once more form the stiffness matrix as used in Eq. 8.15

$$\mathbf{K}_{\mathrm{Inline}} = \begin{pmatrix} k_{\mathrm{AA}} & \kappa & 0 \\ \kappa & k_{\mathrm{BB}} & \kappa \\ 0 & \kappa & k_{\mathrm{CC}} \end{pmatrix} \tag{9.3}$$

with $\kappa_{\mathrm{AB}} = \kappa_{\mathrm{BC}} = \kappa$.

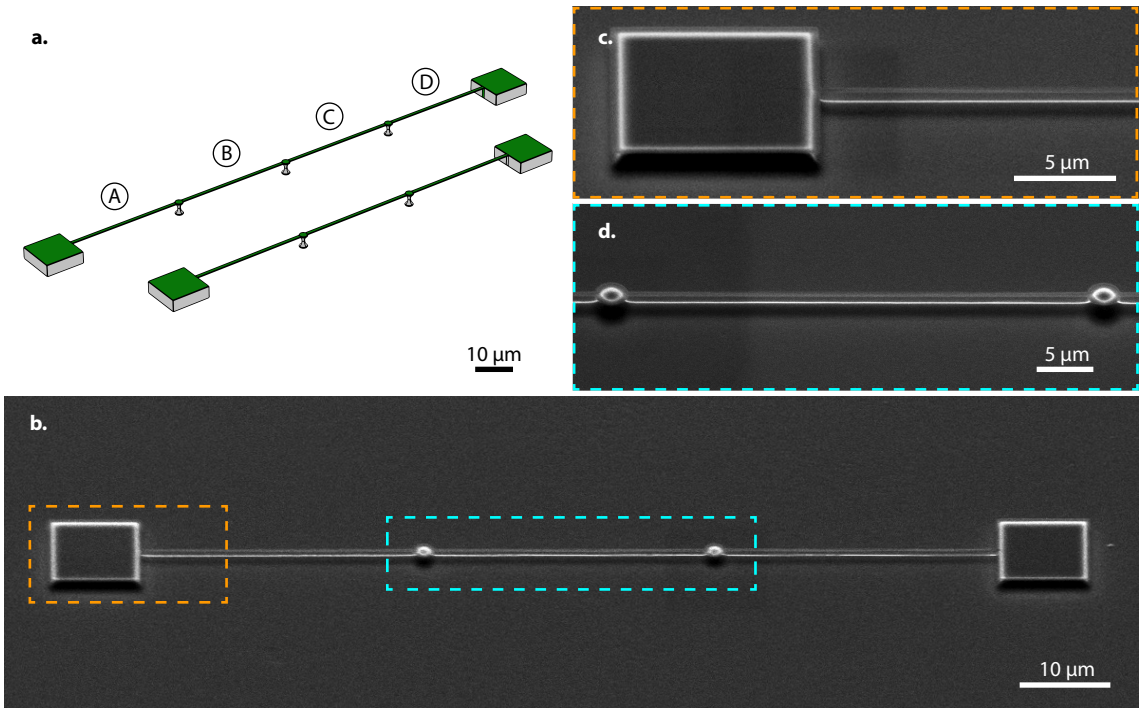

Figure 9.4: **a.** CAD models of the two fabricated inline resonator network designs, consisting of 3 and 4 nanostrings with $(l, w, t) = (30 \cdot 10^3, 300, 90)$ nm respectively. Each string is linked with its nearest neighbour(s) by circular shared supports with a diameter of $2\,\mu$m. The individual strings are assigned letters alphabetically from left to right for future reference. **b.** Scanning Electron Microscopy (SEM) image of a fabricated 3-string network. In the angled perspective, the freely suspended strings are clearly discernible. **c.** Zoom-in on the clamp region. **d.** Zoom-in on the center resonator with its two shared supports.

9.2.4 Shared Support Size and Shape

Early in the design and fabrication process, with the aim to gain a better understanding of the coupling mechanism mediated by the shared support and to determine the most suitable geometry for use in the following design of new resonator networks, *Tri (Series B)* networks have been fabricated with a variety of support geometries and investigated regarding their coupling rates. In the following, we will briefly discuss experimental results of these preliminary measurements since they have proven relevant for the design of subsequent samples.

An overview of the different support geometries fabricated for the investigation is presented in Fig. 9.5b. Out of six investigated designs only one was able to produce measurable inter-resonator coupling: The $2\,\mu$m circular support (i) that was subsequently used for all experimental samples. Notably, even the square support (iii) of almost identical size ($2\text{x}2\,\mu\text{m}^2$) was unable to mediate finite coupling rates. This observation suggests that the corners of the square design somehow prevent *information* about the motion of one nanostring to travel to the other resonators in the network. Consequently, it could be speculated that a continuous path along the freely suspended region of the support structure from one nanostring to another is desirable in order to generate strong inter-resonator coupling between resonators. In any case, these results emphasize

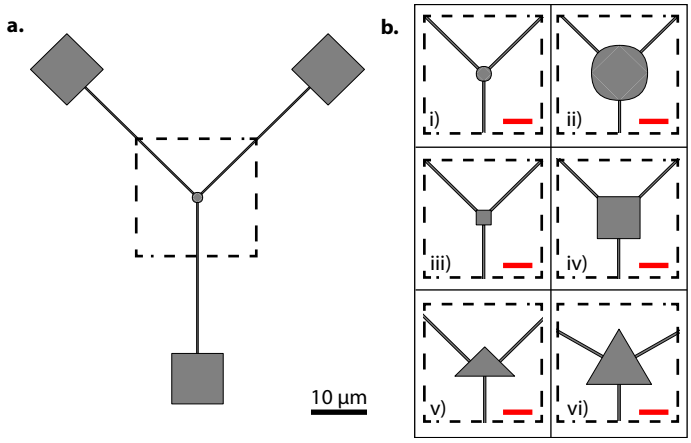

Figure 9.5: a. Top-down illustration of a *Tri (Series B)* resonator network used to evaluate the influence of the shared support geometry. Samples were fabricated with shared supports (black dashed area) of various geometries shown in **b** i-vi. The red bar represents 4 μm. Of all investigated support structures, only the circular support with a diameter of 2 μm (i) resulted in a measurable coupling.

the significance of careful choice of geometric parameters in the design process of mechanical multi-resonator networks.

Chapter 10

Measurement Setup

The measurements in Part II of this thesis were exclusively performed using an optical, homodyne laser interferometry setup. Since the optical setups involved in the experimental setup are fairly complex, whilst contributing comparatively little to the understanding of the results, we will only provide a very rudimentary description of the optics at this point and relegate a more detailed examination to the appendix. Instead, we will utilize the remainder of the chapter to discuss the employed signal processing.

10.1 Laser Interferometry Setup

The centerpiece of the interferometer is a single-mode diode laser with a wavelength of $\lambda = 633\,\mathrm{nm}$ and a maximum power of 50 mW. After being collimated and passed through a single mode optical fiber to ensure optimal coherence and spot shape, the beam is focused onto the sample, which is held in a vacuum chamber ($p < 1 \cdot 10^{-5}\,\mathrm{bar}$), to suppress the negative influence of air-damping on the resonators [144]. The sample itself is glued to a piezoelectric actuator, which can be driven by AC voltages to generate oscillating forces with multiple frequencies which affect the nanomechanical resonators on the chip. Additionally, the piezo-actuator (along with the sample) is mounted on a piezoelectric positioner, allowing for the fine control of the sample position in three dimensions (x,y,z) that is needed to focus the laser beam accurately onto nanostring resonators. Once sufficiently in focus, a small percentage of the incoming light is reflected off the sample, now modulated with the motion of the nanostring, and directed towards a photo-detector, converting the oscillating intensity of the light into an AC voltage signal that is then evaluated using the signal processing setups discussed in the following.

For additional information regarding the interferometry setup itself, please refer to App. A.5 as well as Ref. [146].

10.2 Frequency Domain Setup

An illustration of the frequency domain setup used in a majority of the measurements in this thesis is shown in Fig. 10.1. The piezo-actuator below the sample is connected to the output port

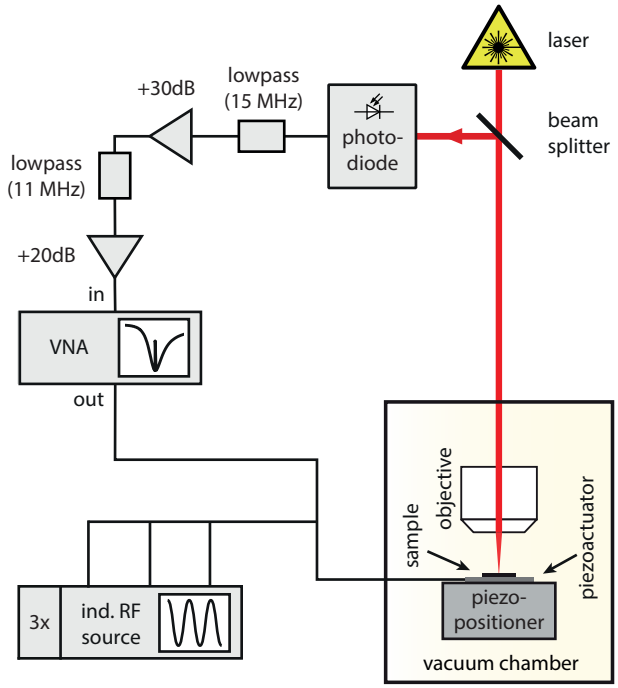

Figure 10.1: Schematic of the optical laser interferometry setup used for frequency domain measurements shown in this thesis. Note that the Vector-Network-Analyzer (VNA) was replaced by a spectrum analyzer for some measurements. The optics have been strongly simplified for this illustration and are discussed in Sec. 10.1.

of a Vector-Network-Analyzer (VNA), with the latter's input port being fed by the amplified (+ 50 dB) and filtered (< 11 MHz) AC photovoltage signal generated by the detector. By sweeping the drive frequency of the VNA and measuring the scattering parameter S_{21}, a response spectrum is generated and resonances of the investigated nanostring become visible as Lorentzian shaped features, allowing their properties, e.g. resonance frequency and linewidth, to be extracted. Three additional radio frequency (RF) signal sources are connected to the piezo-actuator via a power combiner and can be employed as independent auxiliary drive tones, e.g. to excite the higher harmonics of individual resonators necessary to perform eigenfrequency tuning sequences (see Sec. 11.2.1). In order to carry out measurements without an external force applied to the sample and thus investigating solely the thermal motion spectrum of a resonator, the VNA can be replaced by a spectrum analyzer.

10.3 Time Domain Setup

Figure 10.2b shows an illustration of the time domain setup employed in the excitation transfer experiments presented in Sec. 11.3. The most prominent adjustments in comparison to the previous setup are the replacement of the VNA by a fast digitizer card, used for time resolved acquisition of the detector's AC photovoltage signal with up to $200 \cdot 10^6$ samples/s, and the introduction of an Arbitrary Waveform Generator (AWG) capable of designing and emitting

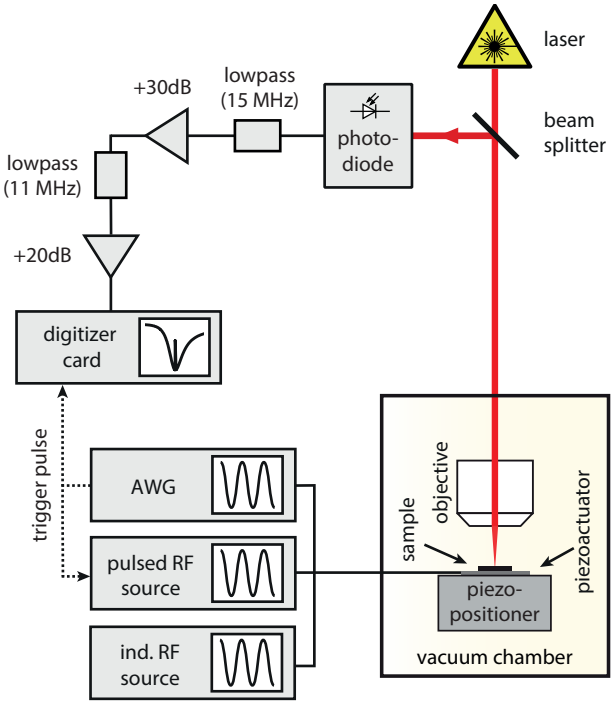

Figure 10.2: Schematic of the optical laser interferometry setup used for the time domain measurements shown in Sec. 11.3. The optics have been strongly simplified for this illustration and are discussed in Sec. 10.1.

almost arbitrarily complex auxiliary drive sequences. Furthermore, one of the RF sources is now configured to produce a pulsed output, controlled by an external modulation port. A detailed description of how the setup is employed to perform excitation transfer experiments is found at the beginning of Sec. 11.3.

10.4 Experimental Challenges

Largely independent of the chosen measurement electronics, the optical detection and the eigenfrequency tuning protocol, when confronted with the peculiarities of nanomechanical structures, encounter challenges that have to be overcome in order to produce consistent experimental results.

First and foremost, the eigenfrequencies of nanostring resonators prove to be heavily temperature-dependent, an effect that can be attributed to additional strain induced by differing thermal expansion coefficients of the string and the underlying substrate [116, 118]. In fact even the energy of the focused laser beam of the detection setup is sufficient to increase a nanostring's resonance frequency by several hundred Hz. However, an equilibrium between heat dissipation and laser heating is usually reached within few minutes. Much more critically, when exposed to the high signal powers necessary to perform eigenfrequency tuning sequences (sometimes ranging up to $10\,\mathrm{V_{rms}}$) the self-heating of the piezoelectric actuator affects the sample and can lead to resonance frequency shifts of several kHz over extended periods of measurement time.

Unfortunately, the current interferometry setup is not capable of reading out the sample temperature, preventing an exact quantification of the heating effects. Instead, as a short term solution, cool-down phases were integrated between measurements or measurement points in order to reduce the impact on the collected data. In the long term, it is desirable to improve heat dissipation from the sample, e.g. by outfitting the vacuum chamber with a suitable cooling system, and to introduce a way of monitoring the sample temperature allowing quantification and correction of arising heating effects.

Lastly, even though short pulse sequences, like the ones performed in excitation transfer experiments, are much less likely to produce significant heating on their own, a multitude of them in quick succession could indeed adversely affect the performance of following sequences due to frequency shifts. Therefore, sufficient heat dissipation should be seen as a key consideration in the design process of more sophisticated resonator network applications.

Chapter 11

Experimental Results

11.1 Characterization of Nanostring Resonators

In the following section we present measurement data of individual Si_3N_4 nanostring resonators that are part of the various resonator networks which were fabricated for this thesis (as introduced in Sec. 9.2). Thermal motion spectra are analyzed to characterize the resonators with respect to their undisturbed resonance frequencies, linewidths[1] and quality factors. These parameters can later be used to model and predict the interaction within a multi-resonator network. Subsequently, we evaluate driven resonance measurements with increasing drive powers in order to access the non-linear regime of the resonators, extracting various material parameters of the strings (e.g the Young's modulus E and the Duffing parameter α) in the process. Finally, we demonstrate the effectiveness of a purely mechanical eigenfrequency tuning method based on the inherent *geometric non-linearity* of nanostring resonators. It will be shown, that, by strongly exciting a nanostring's higher order mode, the resonance frequency of its fundamental mode can be deliberately modified in a way predictable by theory and without negative effect on its quality factor. For all measurements in this section, we have employed the frequency domain setup introduced in Sec. 10.2.

11.1.1 Quality Factors and Linewidth

We begin by presenting a thermal motion spectrum of the fundamental out-of-plane (oop) mode[2] of a single nanostring in a *Tri (Series 2)* resonator network, along with a complex Lorentzian fit (see App. A.2) to the data in Fig. 11.1. The resonance frequency of the examined resonator is determined to be $\Omega_m/2\pi = 9.3123\,\mathrm{MHz}$ with a linewidth of $\Gamma_m/2\pi = 87\,\mathrm{Hz}$ resulting in a quality factor of $Q = \Omega_m/\Gamma_m = 1.07 \cdot 10^5$, a value within the expected range for a Si_3N_4 nanostring resonator of this length (cf. Ref. [147]). Additionally, with the maximum photovoltage amplitude $S_{UU}^{max} = 1.43\,\mathrm{mV^2/Hz}$ extracted from the fit and the thermal motion peak amplitude calculated with Eq. 8.6 to $S_{xx}^{max} = 4.20\,\mathrm{pm^2/Hz}$, we can establish a calibration

[1] *linewidth* refers to the full width at half maximum (FWHM) of a resonator's Lorentzian resonance feature.

[2] In the scope of this thesis, we exclusively investigated the nanostring resonators regarding their out-of-plane vibrational modes. This is due to the fact that for the used optical interferometry setup, oop motion results in higher peak amplitudes and better signal-to-noise ratios. As such, all shown spectra can be assumed to show oop modes unless explicitly stated otherwise.

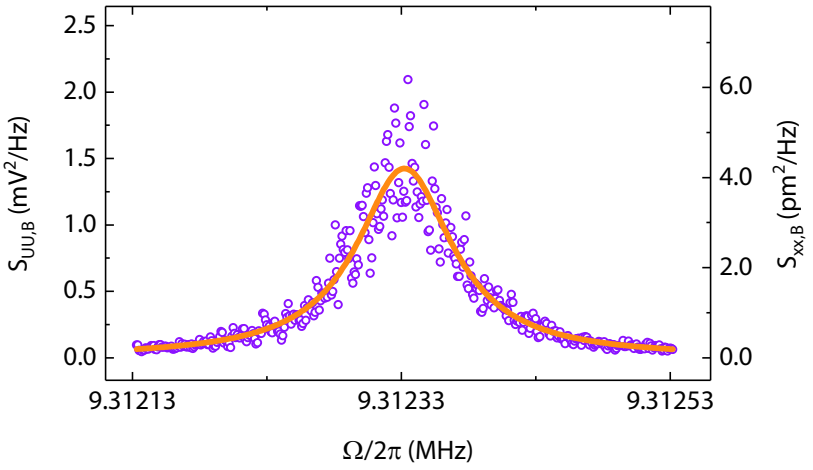

Figure 11.1: Thermal motion spectrum of a single nanostring resonator in a *Tri (Series A)* network. The orange line is a complex Lorentzian fit to the data, used to extract the mode's resonance frequency and linewidth. The fit is also employed to determine the calibration factor between photovoltage (left axis) and mechanical displacement (right axis) according to Eq. 8.6.

factor of $C \equiv S_{\mathrm{xx}}/S_{\mathrm{UU}} = 2.95\,\mathrm{pm}^2/\mathrm{mV}^2$ that allows us to determine the displacement amplitude of the string's motion from the measured voltage signal. For this we used the effective mass of the string $m_{\mathrm{eff}} = 1.053\,\mathrm{pg}$, which we calculated as described in Sec. 8.1.1 from the string's dimensions $(l, w, t) = (30 \cdot 10^3, 300, 90)$ nm and $\rho_{\mathrm{SiN}} = 2600\,\mathrm{kg/m}^3$ [103].

After performing analogous evaluations of thermal motion spectra for several nanostrings in all of the investigated network types, we summarize a selection of the extracted parameters in Tab. 11.1 for comparison. As is expected, we observe small variations in the resonance frequencies and quality factors between different resonators, caused by imperfections arising during fabrication. However, we can not find any systematic differences that can be related to the type of network design. Notably, we find the resonators in position A and B of an *Inline* network to be equivalent within the usual range of variation. Therefore, the type of clamping, one clamp and one shared support on position A compared to two shared supports on position B, does not seem to affect the quality of nanostring resonators significantly. This finding suggests a

network type	resonator pos.	$\Omega_{\mathrm{m}}/2\pi$ (MHz)	$\Gamma_{\mathrm{m}}/2\pi$ (Hz)	Q (10^5)
Tri	B	9.3123	87	1.07
Inline	A	9.2393	83	1.12
Inline	B	9.1740	79	1.16

Table 11.1: Overview of fundamental out-of-plane mode parameters extracted for individual Si_3N_4 nanostring resonators in each of the investigated resonator network designs. The position column refers to the placement of the resonator in the network, as introduced in Sec. 9.2. No significant influence of the network type or resonator placement on the measured quality factors can be observed.

high flexibility in the design process regarding the placement of resonators, eliminating the need for corrections to the string geometries.

11.1.2 Nonlinear Response Regime

In order to investigate the response of nanostring resonators to external drive forces, the spectral analyzer is replaced by a VNA, which allows us to apply a coherent radio frequency signal to the piezo-actuator and record the resulting scattering parameter (see Sec. 10.2). Amplitude spectra of the driven mechanical motion for drive voltages[3] from $U_{\mathrm{VNA}} = 280\,\mu\mathrm{V_{rms}}$ to $1000\,\mu\mathrm{V_{rms}}$ are recorded and shown in Fig. 11.2. Note that the shown displacement amplitudes were converted from the measured signal voltage using a calibration to the thermal motion amplitude as previously detailed in Sec. 11.1.1. The investigated resonator is located on position B in an *Inline*-type network. Following the theoretical prediction, the resonator enters a non-linear response regime (see Sec. 8.3), exhibiting the expected increase in effective resonance frequency as it enters the bistable region characteristic of a forced Duffing oscillator.

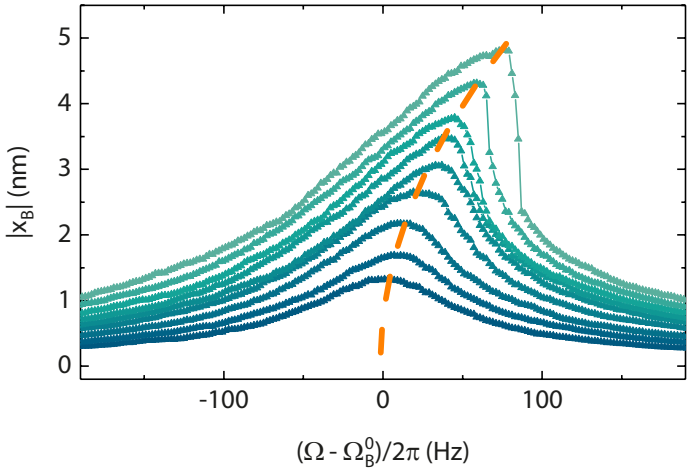

Figure 11.2: Driven mechanical motion spectra of a single nanostring resonator on position B of an *Inline* resonator network for increasing VNA output voltages from $U_{\mathrm{VNA}} = 280\,\mu\mathrm{V_{rms}}$ to $1000\,\mu\mathrm{V_{rms}}$. For high voltages (brighter colors), shifting resonance frequencies and an emerging bistability can be observed, typical for Duffing oscillators. The orange line is a *backbone curve* fit of the maximum displacement amplitudes according to Eq. 8.41, allowing for extraction of the resonators' Duffing parameter α.

The spectra can be fitted according to Eq. 8.41, forming a so-called *backbone curve*, relating the maximum displacement amplitude to the shifted, effective resonance frequency of the resonator. From the fit, we extract the Duffing parameter $\alpha = 3.166 \cdot 10^{27}\,\mathrm{m^{-2}s^{-2}}$ and use it to calculate the material's Young's modulus to $E = 274\,\mathrm{GPa}$. A comparison with literature finds that this value resides much closer to those reported for homogeneous thin films [1] than those experimentally observed with Si_3N_4 string resonators [118, 147, 148] in the past. Remarkably, the

[3] All RF drive voltages given in this thesis correspond to output values of the signal sources, including any subsequent amplification. No statement can be made about potential losses on the path to the piezo-actuator.

tensile stress, calculated from the resonance frequency and Young's modulus following Eq. 8.5 to $\sigma_0 = 736\,\mathrm{MPa}$ aligns very well with published results from the same experiments. Consequently, we attribute the higher observed value to differences in the sample geometry and the fabrication process, possibly lowering the impact of the effects found to reduce the Young's modulus in other publications.

11.1.3 Auxillary Drive Eigenfrequency Tuning

It has been shown that the geometric non-linearity, causing nanostring resonators to behave as Duffing oscillators for high drive powers, can be exploited to selectively tune the eigenfrequency of the resonator [105]. To this end, a strong, external drive voltage is matched in frequency to a higher harmonic of the targeted resonator and globally applied to the chip via the piezo-actuator. The higher harmonic mode is driven into the Duffing regime, where its amplitude depends on the drive frequency, and additional effective stress is induced in the string, altering the resonance frequency of every mode exhibited by the string (see Sec. 8.3.2).

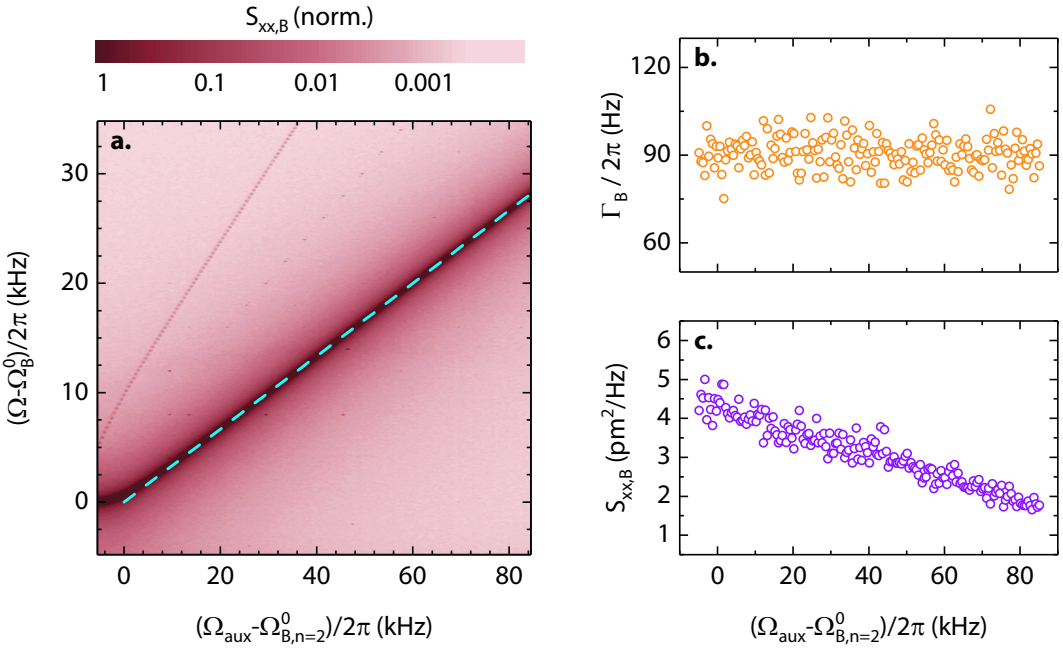

Figure 11.3: **a.** Thermal motion spectrum of nanostring resonator B in a *Tri (Series A)* network as a function of the auxiliary drive frequency Ω_{aux} applied to the piezo-actuator with $U_{\mathrm{aux}} = 3.5\,\mathrm{V_{rms}}$. The expected change in the resonance frequency Ω_{B} according to Eq. 8.47 is drawn as dashed, cyan line. Two low-intensity features are visible in the measurement at frequencies above the investigated resonance peak. They are likely caused by an unintended output of the auxiliary RF source at $\Omega_{\mathrm{aux}}/2$. **b.** Linewidth and **c.** amplitude of the main resonance peak as function of the applied drive frequency. The values are extracted from Lorentzian fits to the individual spectra shown in **a.** No adverse effect of the tuning process on the linewidth is observed. The decrease of the peak amplitude is discussed in the main text.

Fig. 11.3 shows measurement data of a selective eigenfrequency tuning protocol, targeting nanostring B of a *Tri (Series A)* resonator network. In **a.**, thermal motion spectra are presented as a function of the auxiliary drive frequency Ω_{aux} which is first initialized slightly below the second harmonic mode frequency $\Omega^0_{\mathrm{B,n=2}}$ and is subsequently swept upwards by roughly 80 kHz. The voltage of the auxiliary signal is $U_{\mathrm{aux}} = 3.5\,\mathrm{V_{rms}}$, driving the second harmonic mode of the nanostring deep in the non-linear response regime. As a result, the resonance frequency of the fundamental mode (dark color) can be clearly seen following the increase in applied drive frequency and perfectly matches the theoretical prediction given by Eq. 8.47 and highlighted by the cyan dashed line. At frequencies slightly above the main resonance peak, two low-intensity features are visible in the measurement, apparently being tuned by the drive signal. We attribute them to an unintended output of the auxiliary RF source, which is known to generate signals at half its configured output frequency, i.e. $\Omega_{\mathrm{aux}}/2$, due to technical reasons. In Fig. 11.3b-c, the development of the thermal motion spectra's linewidth and amplitude is shown over the course of the tuning sequence, extracted from Lorentzian fits (Eq. A.3) to the data presented in **a.** While the observed linewidth shows minor fluctuations - an effect that can be attributed to a combination of thermal instabilities and uncertainties of the fit - it becomes clear that the eigenfrequency tuning operation does not adversely affect the linewidth of the targeted mode. This, of course, is important to ascertain for any potential application of the tuning protocol relying on constantly high quality factors for operation. The peak amplitude, on the other hand, appears to linearly decrease over the course of the measurement. It seems possible that the presence of high amplitude oscillations of the second harmonic mode (whose squared displacement depends linearly on the frequency) impairs the sensitivity of the optical detection to the fundamental mode, which is not excited by an external drive, thus exhibiting much lower amplitudes. However, the origin of this effect would need to be investigated further in order to confirm or rule out a dependency on the tuning mechanism.

11.2 Characterization of Nanostring Resonator Networks

After having successfully characterized the behavior and properties of individual Si_3N_4 nanostrings, we extend the discussion to multi-resonator networks. In particular, we demonstrate the ability to individually and independently address and tune multiple resonators in a network using the previously introduced eigenfrequency tuning protocol. Subsequently, we employ the discussed tuning mechanism to demonstrate the appearance of hybridized states when multiple strings are brought into resonance and prove the existence of strong inter-resonator coupling by analyzing avoided crossings. The different resonator network designs will be characterized regarding their inter-resonator coupling rates, comparing the experimental results with theoretical predictions made at the design-stage. Finally, the appearance of *dark-modes* in a strongly coupled *Tri* resonator network is investigated and reproduced using theoretical models.

11.2.1 Independent Tuning

Applications of mechanical multi-resonator networks in the field of information processing or storage (cf. e.g. Refs. [107–109]) are inherently reliant on protocols to perform targeted transfer

of phonons in between multiple resonators. To this end, the capability to control the resonance frequency of individual resonators without affecting other parts of the network is a crucial requirement. While tuning techniques based on dielectric gradient forces have been widely adopted (cf. e.g. [106, 113, 114]), they require local control gates to address individual resonators. In the following, we want to demonstrate that the previously introduced eigenfrequency tuning protocol based on the non-linearity of higher harmonic modes (see Secs. 8.3.2 and 11.1.3) is able to fulfill this requirement via global application of a drive voltage to the piezo-actuator. This completely eliminates the need for local control gates, promising increased scalability on the way to larger multi-resonator networks.

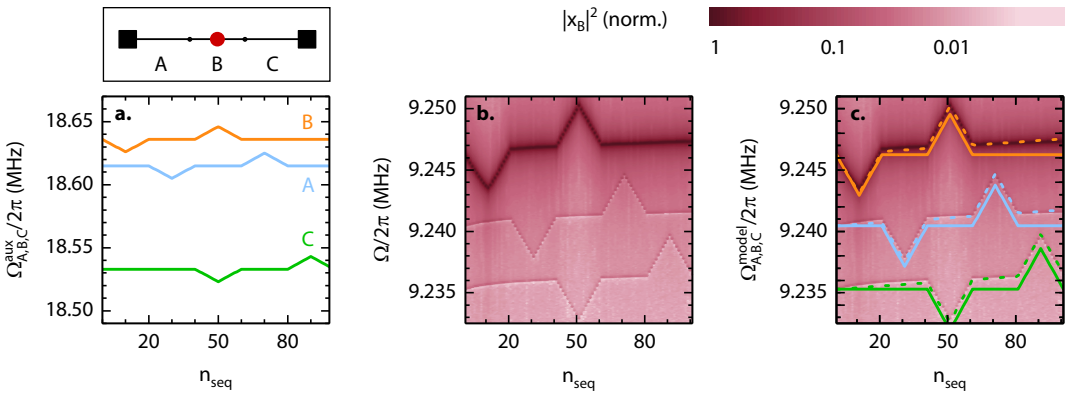

Figure 11.4: a. A multi-resonator tuning sequence. The frequencies $\Omega^{\text{aux}}_{\text{A,B,C}}$ of three auxiliary drive signals are shown over n_{seq}, the index of the sequence's sweep-points. Each signal, generated by an independent source with $U_{\text{aux}} = 3.5\,\text{V}_{\text{rms}}$, performs a separate eigenfrequency tuning operation targeted at a single resonator in the investigated network. **b.** Driven mechanical motion spectrum of resonator B of an *Inline*-type network over the course of the tuning sequence, measured with a VNA output voltage of $U_{\text{VNA}} \approx 0.7\,\mu\text{V}_{\text{rms}}$. **c.** The measurement data shown in **b.**, superimposed with two models predicting the development of the resonators' eigenfrequencies due to the tuning sequence. The solid lines represent the model according to Eq. 8.47, while the dashed lines are obtained by addition of a linear correction term to the former model, intended to compensate the self-heating of the piezo-actuator. Note that all resonators have been initialized to higher frequencies prior to the shown measurement in order to make downwards tuning possible. The illustration above **a.** clarifies the resonator naming scheme and the laser spot position (red).

In order to demonstrate the capabilities of the eigenfrequency tuning technique, we design a complex auxiliary drive sequence shown in Fig. 11.4a. Three independent drive signals with the frequencies $\Omega^{\text{aux}}_{\text{A,B,C}}$ and voltages $U^{\text{aux}}_{\text{A,B,C}} = 3.5\,\text{V}_{\text{rms}}$ are combined and applied to the piezo-actuator, with each of the signals intended to perform a separate tuning operation on one of the strings in the *Inline* network investigated in this experiment. As such, each frequency $\Omega^{\text{aux}}_{\text{A,B,C}}$ is matched to the second harmonic mode of one targeted resonator (i.e. $\Omega^{\text{aux}}_{\text{A}} = \Omega^{0}_{\text{A,n=2}}$). As previously discussed in Secs. 8.3.2 and 11.1.3, a strong auxiliary signal causes the higher harmonic mode it drives to enter a non-linear response regime, where its amplitude depends on the drive frequency. The high oscillation amplitudes lead to an effective elongation of the string which induces additional stress in the material, altering the resonance frequency of the string's

fundamental mode depending on the auxiliary frequency. Notably, the three drive signals are applied simultaneously to the piezo-actuator in this experiment, demonstrating that the required superposition of the three forces is achievable.

It is important to note that prior to the measurement (not shown in the figure), the three drive frequencies have been swept upwards, increasing the eigenfrequencies of all resonators by several kHz, effectively initializing them to their new levels $\Omega^{\mathrm{init}}_{\mathrm{A,B,C}} > \Omega^{0}_{\mathrm{A,B,C}}$. This is necessary since the eigenfrequency tuning mechanism is based on the addition of effective stress to the material, therefore a decrease of the resonance frequency below its undisturbed level is not possible (i.e. $\sigma_{\mathrm{eff,tuning}} > 0$). However, a controlled downtuning of the eigenfrequencies of previously raised frequencies using the same tuning protocol is feasible, as demonstrated here.

After initialization, the auxiliary frequencies are decreased one after another by 10 kHz below their initial levels $\Omega^{\mathrm{init}}_{\mathrm{A,B,C}}$ and then subsequently swept to higher frequencies of $\Omega^{\mathrm{init}}_{\mathrm{A,B,C}}/(2\pi) + 10\,\mathrm{kHz}$. We observe the influence of the driving sequence on the fundamental modes by recording a driven mechanical motion spectrum for each sweep-point n_{seq} while the laser spot is focused on nanostring B. The resulting spectra are presented in Fig. 11.4b and show three distinct features (darker colors). The strongest feature corresponds to the fundamental mode of the nanostring spatially selected by the laser, while the less intense features result from an inter-resonator coupling across the network, making the resonance frequencies of both coupled resonators observable in the spectrum of the third. This is already an indication of a finite inter-resonator coupling in the investigated nanostring network. Clearly, it can be seen that the resonance frequencies of all three resonators in the network can be controlled by their respective drive frequencies. In addition, the fundamental mode frequencies $\Omega_{\mathrm{A,B,C}}$ are visibly not sensitive to the changes in the frequencies of the other modes (here in the limit of far detuning), suggesting a purely selective tuning of the modes via their respective drive tones. To validate this visual interpretation, we perform a model calculation according to Eq. 8.47, predicting the shifting of eigenfrequencies of the three resonators based on the applied drive signals. Results from the calculation are shown in Fig. 11.4c. It should be pointed out that for the calculation, Eq. 8.47 has been applied to every resonator individually, only taking into account its own resonance frequency and the single drive signal targeted at its second harmonic mode.

Comparing the model predictions (solid lines) and the position of the resonance features in the spectrum, a deviation from the calculation does stand out. While the tuning operations themselves, the triangular shaped up- and downtuning of the frequency, are accurately represented, we observe a gradual upwards drift for all experimental resonance frequencies, that is not explained by theory. As previously discussed in Sec. 10.4, we can confidently attribute this drift to self-heating effects within the piezo-actuator, caused by the three comparatively high powered drive signals. Since the measurement shown in Fig. 11.4 took 30 minutes to complete and empirical observations during the measurements for this thesis show the heating influence on nanostring resonance frequencies to behave relatively linear for long measurements, we attempt to apply a correction to the theoretical predictions in Fig. 11.4c in the form of a linear heating term added to the tuning model (dashed lines). With the heating correction term applied, the

theoretical model visually appears to accurately reproduce the experimental data experimental data. To further examine the validity of the model, we extract the resonance frequencies from the experimental data shown in Fig. 11.4b by fitting the peaks of every individual amplitude spectra using a complex Lorentzian function. The results along with the two model calculations are presented in Fig. 11.5.

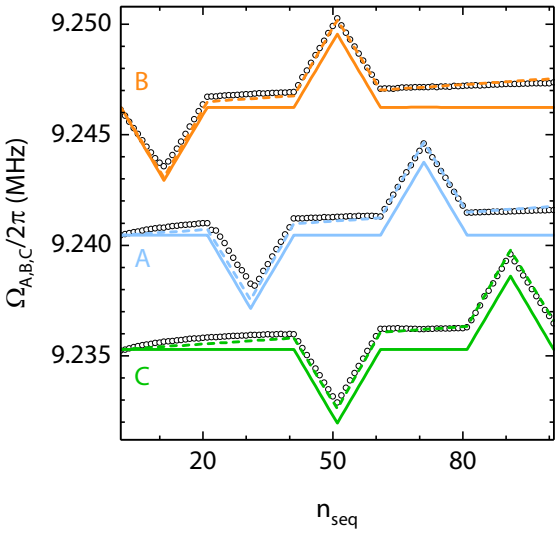

Figure 11.5: Extracted fundamental mode resonance frequencies $\Omega_{A,B,C}$ (black circles) of the three nanostrings A,B and C over the course of the auxiliary drive sequence presented in Fig. 11.4. The frequencies have been extracted by applying complex Lorentzian fits to the individual peaks found in the mechanical motion spectra shown in Fig. 11.4b. The solid lines represent a model calculation of the fundamental mode frequencies in response to the applied drive tones (see Fig. 11.4a) according to Eq. 8.47. The dashed lines are obtained by addition of a linear correction term to the former model, intended to compensate the self-heating of the piezo-actuator. The model calculations are performed individually for each mode, with the color of the line indicating the corresponding nanostring. We observe deviations of both models in the beginning of the measurement, i.e. $n_{seq} < 40$, corresponding to the first 10 minutes of measurement time. However, the heat-corrected model shows increasingly good agreement towards the end of the measurement.

Examining the extracted data along with the two model calculations, we observe a deviation from the linear heating model in the beginning of the measurement sequence, i.e. for $n_{seq} < 40$, which corresponds to the first 10 minutes of the measurement. In this region, the experimentally observed resonance frequencies increase more rapidly than predicted by the model. However, the slope of the frequency increase flattens and takes a more linear shape as the measurement progresses and eventually shows good agreement with the prediction. Based on these observations, it seems plausible that the heating effects in fact follow a more complex behavior, especially in the beginning of the measurement. Furthermore, one would expect the heating to eventually saturate towards a thermal equilibrium. However, since we still observe a finite slope for the resonance frequencies at the end of the measurement, the 30 minute duration of this experiment does not appear to be sufficient to reach an equilibrium state. In order to

quantify this behavior, the sample temperature or a related quantity would have to be observed. In thermal motion measurements for example, the amplitude of the recorded spectra could allow to draw conclusions on the temperature. However, the impact of the temperature-dependent thermal motion, which usually resides in the picometer regime (see Fig. 11.1), is negligible in comparison to the nanometer amplitudes observed in driven displacement spectra (see Fig. 11.2) as recorded here. In the long term, as discussed in Sec. 10.4, outfitting the detection setup with a way to monitor the temperature during the measurement would allow a more thorough investigation of the heating effects. Importantly, aside from the previously discussed effects, we see no indication in the extracted experimental data pointing towards any unpredicted, adverse influence of the simultaneous tuning operations.

However, due to the global application of drive signals an inherent challenge for the tuning protocol presents itself in the form of mode-mode cross-talk, i.e overlap in the drive frequency range of different resonators due to *frequency crowding* [149], which can lead to the unintentional tuning of multiple resonators with one drive signal. To circumvent this problem, the higher harmonic frequencies of the resonators that are part of a network have to lie sufficiently far apart. This goal can be accomplished partly by thoughtfully choosing the geometric parameters of the resonators, but also requires post-selection of fabricated networks, as has been done for all samples shown in this thesis. A more detailed look at the challenges of frequency crowding along with an example can be found in App. A.6.

In conclusion, the eigenfrequency tuning technique presented in this thesis is capable of independently addressing multiple resonators in a resonator network without relying on local control gates and has the potential to be a useful tool for applications in targeted excitation transfer experiments, which will be explored in Sec. 11.3.

11.2.2 Inter-Resonator Coupling

In this section, we employ the previously established tuning mechanism in order to quantify the inter-resonator coupling rates of the investigated multi-resonator networks. To this end, we tune pairs of two nanostring resonators in resonance, where the inter-resonator coupling leads to a hybridized state. From the spatial distribution of this state, information can be extracted about the magnitude of the coupling (see Sec. 8.1.2 and e.g. Refs. [102, 110]).

Tri Resonator Networks (Series A)

First, we probe mechanical motion spectra of resonator A of a *Tri (Series A)* nanostring network over the course of an eigenfrequency tuning sequence and present the data in Fig. 11.6a. The tuning sequence employs two drive signals at $\Omega^{\mathrm{aux}}_{\mathrm{A,B}}$ with $U^{\mathrm{aux}}_{\mathrm{A,B}} \approx 7\,\mathrm{V_{rms}}$, targeting resonator A and B respectively, and tuning each possible pair of resonators in the network in resonance, inducing the formation of hybridized states and avoided crossings. In turn, we observe three individual avoided crossings between B and C at $n_{\mathrm{seq}} \approx 31$, A and C at $n_{\mathrm{seq}} \approx 50$, A and B at $n_{\mathrm{seq}} \approx 58$, each containing information about one of the three inter-resonator coupling rates. Figure 11.6b displays a more highly resolved measurement in the area around the third avoided

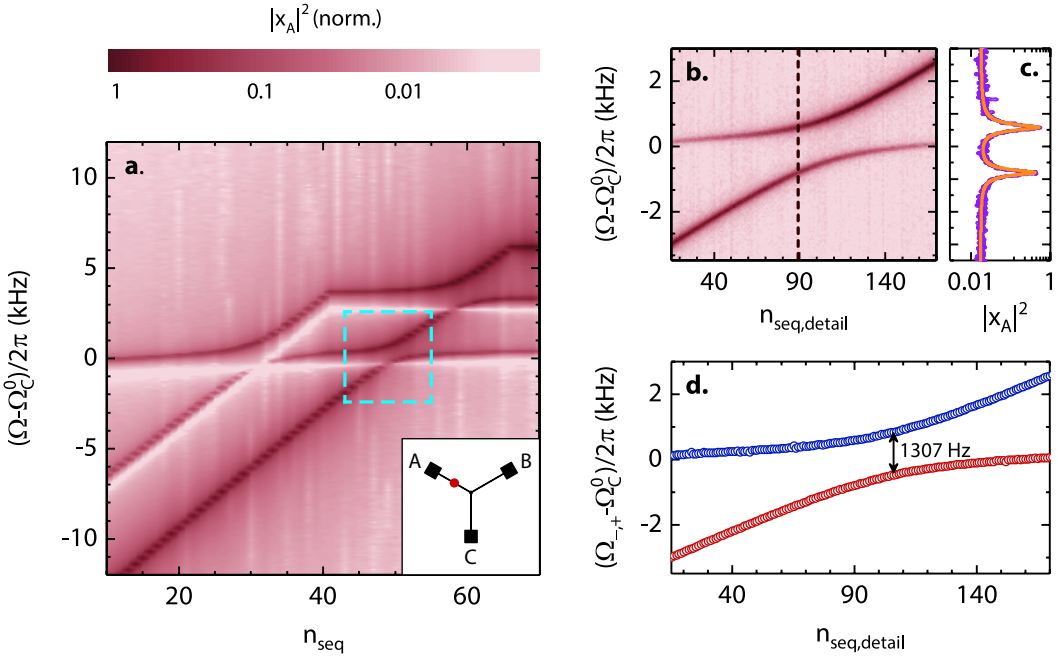

Figure 11.6: **a.** Driven mechanical motion spectrum of resonator A in a *Tri (Series A)* nanostring network over the course of an eigenfrequency tuning sequence, indexed by sweep-points n_{seq}. The sequence consists of two independent drive signals with $U_{\mathrm{aux}} \approx 7\,\mathrm{V_{rms}}$ and is designed to induce avoided crossings between all of the involved resonators pair-by-pair. The inset shows the network layout and the laser spot position (red). As expected, three individual avoided crossings are visually discernible. **b.** A more detailed measurement of the avoided crossing between resonators A and C (dashed cyan area) **c.** A single spectrum from the data shown in panel b. for $n_{\mathrm{seq,detail}} = 89$ (dashed black line). The solid orange line is a double Lorentzian fit to the data, used to determine the resonance frequencies of both involved resonators. **d.** Fitted resonance frequencies of the lower (red) and upper (blue) branch of the avoided crossing shown in **b.**, extracted from the individual spectra as demonstrated in **c.** The minimal mode-splitting is found at $n_{\mathrm{seq,detail}} = 106$ to be $g_{\mathrm{AC}}/2\pi = 1307\,\mathrm{Hz}$.

crossing (dashed cyan). In order to extract the coupling rates, avoided crossing behavior between the modes is quantitatively analyzed. This process is most accurately accomplished by fitting the recorded displacement spectra with two Lorentzian lineshapes to determine both resonance frequencies of the modes. Fig. 11.6c visualizes this process for the data presented in panel b for $n_{\mathrm{seq,detail}} = 89$ (black dashed line). Hereby, we find two resonance frequencies Ω_+ and Ω_-, referring to the upper and lower branch of the avoided crossing respectively.[4] Repeating this process for every spectrum in the datasets allows us to extract the dispersion of resonator A's and C's resonance frequencies along the avoided crossing (see Fig. 11.6d). Finally, the mode-splitting can be extracted by finding the minimum difference between the two resonance frequencies which

[4] It should be noted that employing a double Lorentzian fit model (i.e. the simple addition of two Lorentzian functions) is only valid as long as the peaks are well seperated with respect to their linewidth (i.e. $\Omega_+ - \Omega_- > \Gamma_{+,-}$). Fig. 11.6c shows the condition is clearly fulfilled in this case.

parameter	value
$g_{\mathrm{AC}}/2\pi$	1307 Hz
$g_{\mathrm{AB}}/2\pi$	1281 Hz
$g_{\mathrm{BC}}/2\pi$	1230 Hz

Table 11.2: Summary of the experimentally determined inter-resonator coupling rates in the *Tri (Series A)* network investigated in this section.

is found at $n_{\mathrm{seq,detail}} = 106$ to be

$$g_{\mathrm{AC}}/2\pi = \min|\Omega_+ - \Omega_-|/2\pi = 1307\,\mathrm{Hz}.$$

Analogous investigations of the avoided crossing between resonators B and C as well as A and B have been performed and can be found in App. A.7.1. We summarize the extracted coupling rates in Tab. 11.2. The expectation that a symmetric geometry of *Tri (Series A)* networks, in particular with a symmetrically shaped shared clamp, results in an equal coupling rate between all of the involved resonators is hereby strongly supported. All inter-resonator coupling rates are within a range of 80 Hz. From the coupling rates, the coupling factors κ_{ij} can be calculated using the effective mass of the resonators $m_{\mathrm{eff}} = 1.053\,\mathrm{pg}$ and Eq. 8.10. Subsequently we assemble the complete stiffness matrix for the investigated network as used in Eq. 8.15

$$\mathbf{K}_{\mathrm{Tri,SA}} = \begin{pmatrix} -3.535 & -7.0\cdot10^{-4} & -7.1\cdot10^{-4} \\ -7.0\cdot10^{-4} & -3.553 & -6.7\cdot10^{-4} \\ -7.1\cdot10^{-4} & -6.7\cdot10^{-4} & -3.561 \end{pmatrix} \mathrm{kg/s^2}. \tag{11.1}$$

Notably, all of the values fall in line with the previously observed inter-resonator coupling rate of two purely mechanically coupled nanostrings [105]. Moreover, due to the small damping rates of the investigated nanostring resonators $\Gamma_{\mathrm{A,B,C}} \approx 80\,\mathrm{Hz}$, the observed coupling rates easily fulfill $g_{\mathrm{AB,AC,BC}} \gg \Gamma_{\mathrm{A,B,C}}$, placing the network deeply in the strong coupling regime, a key requirement for the coherent and controlled transfer of excitations in a network that will be investigated later on.

Tri Resonator Networks (Series B)

Figure 11.7a shows a driven mechanical motion spectrum of nanostring A of a *Tri (Series B)* nanostring network[5] over the course of a performed eigenfrequency tuning sequence. In this case, only resonator A is tuned upwards by a single drive signal with $U_{\mathrm{aux}} \approx 4\,\mathrm{V_{rms}}$, intended to cause avoided crossings with both other resonators in the network.

Avoided crossings can clearly be observed at $n_{\mathrm{seq}} \approx 30$ between resonators A and B as well as around $n_{\mathrm{seq}} \approx 145$ between resonators A and C. It is immediately noticeable that the latter

[5] Please take note of the ordering of the nanostring's resonance frequencies for the investigated *Series B* network: $\Omega^0_{\mathrm{B}} > \Omega^0_{\mathrm{C}} > \Omega^0_{\mathrm{A}}$.

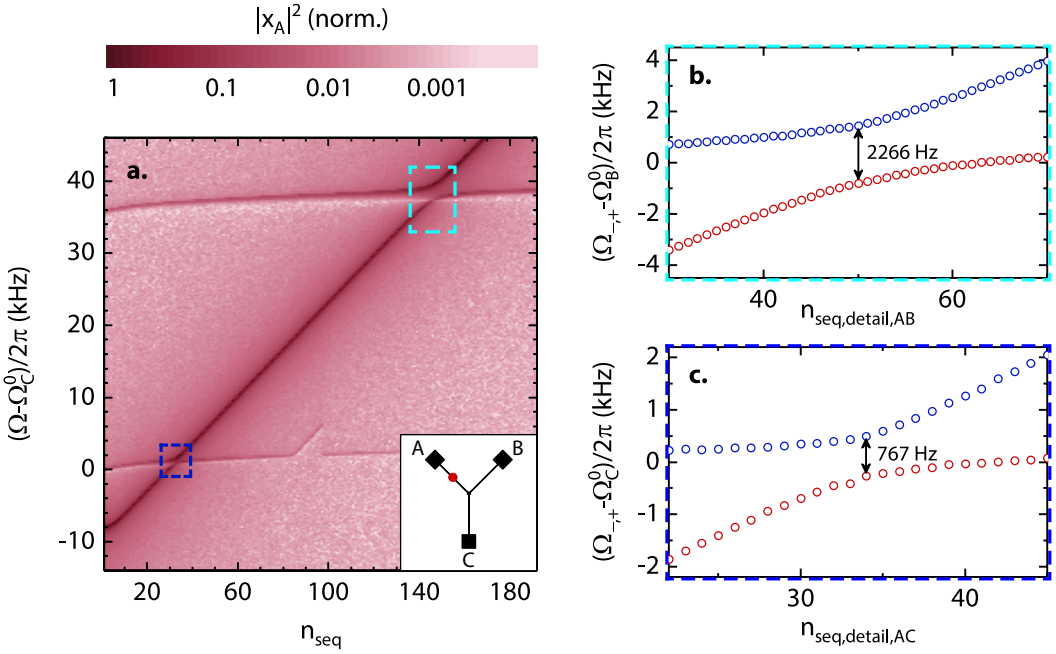

Figure 11.7: **a.** Driven mechanical motion spectrum of resonator A in a *Tri (Series B)* nanostring network over the course of an eigenfrequency tuning sequence, indexed by sweep-points n_{seq}. The sequence consists of one drive signal with $U_{\mathrm{aux}} \approx 4\,\mathrm{V_{rms}}$, tuning resonator A upwards and leading to avoided crossings with the two remaining nanostrings in the network. The inset shows the network layout and the laser spot position (red). Both expected avoided crossings are clearly visible, but show a significantly different extent of mode-splitting. An instance of unintended tuning due to frequency crowding is visible around $n_{\mathrm{seq}} \approx 85 - 100$ (see main text). **b-c.** Development of resonance frequencies for the upper (blue) and lower (red) branch of the avoided crossings of two resonators, extracted from double Lorentzian fits to individual mechanical motion spectra. **b.** presents frequencies fitted to a more detailed measurement of the dashed cyan area and extracts a coupling rate of $g_{\mathrm{AB}}/2\pi = 2266\,\mathrm{Hz}$. **c.** presents frequencies fitted to a more detailed measurement of the dashed blue area and extracts a coupling rate of $g_{\mathrm{AC}}/2\pi = 767\,\mathrm{Hz}$.

crossing exhibits a significantly larger mode-splitting than the former, pointing to an asymmetric coupling behavior in the network. To quantify this observation, we extract numerical values for the extent of the mode-splitting from the measurement data. In Fig. 11.7b-c, the resonance frequencies of the upper and lower branches of the avoided crossing areas have been extracted using double Lorentzian fits to individual spectra taken from more detailed measurements. Once again seeking the minimum mode separation, we receive

$$g_{\mathrm{AC}}/2\pi = 767\,\mathrm{Hz} \text{ and}$$
$$g_{\mathrm{AB}}/2\pi = 2266\,\mathrm{Hz},$$

confirming the visual observation of significant differences in the coupling rate.

Unfortunately, due to the influence of frequency-crowding (see Sec. 11.2.1), independent tuning

of resonator C in resonance with resonator B is not possible for this sample. Moreover, the same effect leads to a brief unintended tuning of resonator C by the drive signal targeting resonator A, which can be seen in Fig. 11.7a around $n_{\mathrm{seq}} \approx 85 - 100$. This circumstance prevents us from extracting the third coupling rate g_{BC}. However, the successfully extracted values do confirm an influence of the resonator placement on the resulting coupling rates: As expected, resonators A and B, only separated by a 90° angle in the *Series B* design, exhibit a significantly larger inter-resonator coupling in comparison to resonators A and B, being placed in a 135° angle. Given the symmetry of the network geometry about the plane spanned by resonator C, it is highly plausible that the unobserved coupling rate g_{BC} closely resembles g_{AC}.

In conclusion, the *Series B* resonator network, described by its stiffness matrix calculated as above[6] to

$$\mathbf{K}_{\mathrm{Tri,SB}} = \begin{pmatrix} -1.653 & -5.8 \cdot 10^{-4} & -1.9 \cdot 10^{-4} \\ -5.8 \cdot 10^{-4} & -1.669 & \kappa_{\mathrm{BC}} \\ -1.9 \cdot 10^{-4} & \kappa_{\mathrm{BC}} & -1.656 \end{pmatrix} \mathrm{kg/s^2}, \tag{11.2}$$

has been shown to exhibit strong inter-resonator coupling and furthermore proves the large influence that the geometric design properties, in particular the placement of the resonators, have on the resulting coupling rates. By employing this knowledge in the design stage, resonator networks can be specifically designed to exhibit different coupling rates in between groups of resonators.

Inline Resonator Networks

Moving on to the final resonator network design, Fig. 11.8a shows measured mechanical motion spectra of nanostring B in an *Inline* resonator network[7] exposed to an eigenfrequency tuning sequence. Similar to the first presented sequence, two independent tuning signals with $U_{\mathrm{aux}} \approx 10\,\mathrm{V_{rms}}$ targeted at higher harmonics of resonators A and C are employed to induce pair-wise crossings of the resonance frequencies for all of the nanostrings in the network. We observe visible avoided crossings between resonators A and B as well as C and B at $n_{\mathrm{seq}} \approx 35$ and $n_{\mathrm{seq}} \approx 58$ respectively. However, for the leftmost crossing, no obvious mode-splitting is visible when bringing resonators A and C on resonance. Towards the end of the sequence, another instance of frequency crowding can be observed, unintentionally increasing the resonance frequency of resonator B. However, in this case the effect only appears outside the region of interest for the experiment.

Proceeding as above, we fit the resonance frequencies for the separate branches of the avoided crossings, extracting coupling rates of

$$g_{\mathrm{AB}}/2\pi = 260\,\mathrm{Hz} \text{ and}$$
$$g_{\mathrm{BC}}/2\pi = 207\,\mathrm{Hz}$$

[6] Unlike all other samples investigated in this thesis, this *Tri (Series B)* network consists of nanostrings with a width of 140 nm. This results in a different effective mass used for calculation: $m_{\mathrm{eff}}^{\mathrm{Tri,SB}} = 4.9 \cdot 10^{-16}\,\mathrm{kg}$.

[7] Please note the order of resonance frequencies for the investigated *Inline* network: $\Omega_{\mathrm{B}}^0 > \Omega_{\mathrm{C}}^0 > \Omega_{\mathrm{A}}^0$.

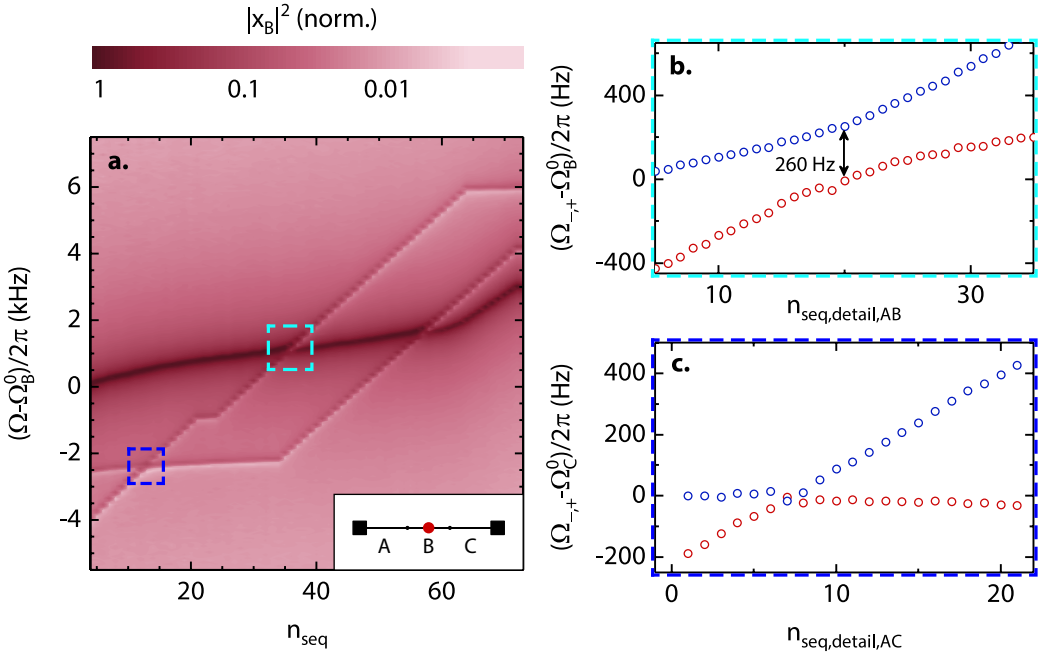

Figure 11.8: a. Driven mechanical motion spectrum of resonator B in a *Inline* nanostring network over the course of an eigenfrequency tuning sequence, indexed by sweep-points n_{seq}. The sequence consists of two independent drive signals with $U_{\mathrm{aux}} \approx 10\,\mathrm{V_{rms}}$ designed to induce crossings of all resonators' eigenfrequencies in the network pair by pair. The inset shows the network layout and the laser spot position (red). We observe two avoided crossings, but no obvious mode-splitting is visible at the leftmost crossing. **b-c.** Development of resonance frequencies for the upper (blue) and lower (red) branch of the avoided crossings of two resonators, extracted from double Lorentzian fits to individual mechanical motion spectra. **b.** presents frequencies fitted to a more detailed measurement of the dashed cyan area and extracts a coupling rate of $g_{\mathrm{AB}}/2\pi = 260\,\mathrm{Hz}$. **c.** presents frequencies fitted to a more detailed measurement of the dashed blue area. No finite mode-splitting can be extracted from the fitted crossing of resonators A and C.

from Fig. 11.8b and Fig. A.6, respectively. However, even with the fits of a more detailed measurement, no trace of mode-splitting can be found in Fig. 11.8c, confirming a coupling rate smaller than the resolution of the measurement. Using this data, we assemble the *Inline* network's experimentally observed stiffness matrix, as introduced previously, to

$$\mathbf{K}_{\mathrm{Inline}} = \begin{pmatrix} -3.529 & -1.4\cdot10^{-4} & 0 \\ -1.4\cdot10^{-4} & -3.551 & -1.1\cdot10^{-4} \\ 0 & -1.1\cdot10^{-4} & -3.532 \end{pmatrix} \mathrm{kg/s^2}, \tag{11.3}$$

matching the theoretical predictions formulated in Sec. 9.2.3. It stands out that the observed coupling rates are considerably lower than those observed for the other investigated network designs, but our previous observations regarding the influence of resonator placement on coupling rates can attribute the reduction to the larger angle (180°) in between the linked resonators. However, with $\frac{g}{\Gamma} \approx 4$ the values are approaching the lower limit of the strong coupling regime, a fact that might impair the performance of excitation transfer protocols.

11.2.3 Mechanical Dark Modes

Modes that can not absorb or emit excitations and thus are not visible in measurements are commonly called *dark-modes*. Such modes have been extensively studied in the field of optomechanics [150–152]. Moreover, in a recent experiment, mechanical dark-modes were observed in strongly three-mode coupled micromechanical systems [106]. Mechanical *dark-modes* have been described as the mechanical analogue to electromagnetically induced transparency [153, 154] and coherent population trapping [155]. In order to understand the appearance of this interesting phenomenon in our system, we dedicate the following section to the investigation and modeling of the observed features.

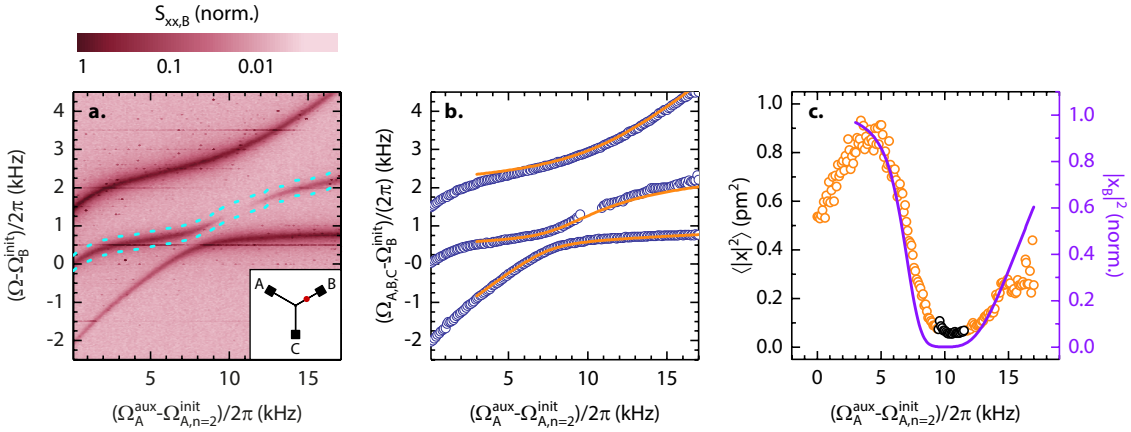

Figure 11.9: **a.** Thermal motion spectrum of resonator A in a *Tri (Series A)* nanostring network as a function of the auxiliary drive frequency $\Omega_{\mathrm{A}}^{\mathrm{aux}}$. With the tuning sequence, resonator A is tuned in resonance with resonators B and C, which have been initialized to be on resonance (not shown), forming a *dark-mode*, noticeable by the temporarily vanishing central branch (found between the dashed cyan lines). The inset shows the network layout and the laser spot position (red). **b.** The blue circles show the resonance frequencies of the three hybridized modes $\Omega_{\mathrm{A,B,C}}$, extracted by fitting the spectra shown in panel **a.** with three Lorentzian line shapes. The orange lines represent a model calculation of the same hybridized mode frequencies (see main text). **c.** Experimentally observed spectral density (orange circles) integrated over the area between the dashed cyan lines in panel **a.** Black circles signify spectra without a visible peak, i.e. noise spectral density. The purple line represents a model calculation for the normalized displacement of resonator B, $|x_{\mathrm{B}}|^2$ (right scale), evaluated at the resonance frequencies along the center branch of the hybridized mode. The calculation reproduces the vanishing displacement observed on resonator B once the central mode goes *dark*.

Building on the reported observation in strongly three-mode coupled systems, we attempt to prompt the appearance of dark-modes in a *Tri (Series A)* nanostring network by tuning all three resonators in the network in resonance. To this end, we design an eigenfrequency tuning sequence that brings two of the nanostrings in resonance (in this case resonators B and C) until the mode-splitting becomes visible, and subsequently increase the eigenfrequency of the remaining resonator (A) until it would cross the frequencies of the hybridized states. Experimental data recorded over the course of this sequence is presented in Fig. 11.9a. It shows the thermal motion spectra of resonator B as a function of the auxiliary drive frequency.

Note that the initialization of the other resonators to the hybridized state is not shown in the plot.

With the simultaneous interaction of three coupled resonators close to resonance, we observe a much more complex hybridization of states, compared to the previously investigated avoided crossings, that can no longer be described by the approximation of two independent crossings (see Sec. 8.1.4). This fact becomes apparent due to the two separate mode-splittings of visibly different size, although the inter-resonator coupling has been shown to be roughly equal for all of the involved resonators in this network. More importantly, the central branch (between the dashed cyan lines) vanishes temporarily from $(\Omega_{\mathrm{A}}^{\mathrm{aux}} - \Omega_{\mathrm{A,n=2}}^{\mathrm{init}})/2\pi \approx 8\,\mathrm{kHz}$ to 13 kHz, apparently forming one of the dark-modes sought to be observed in this experiment. In order to quantitatively analyze the measurement, we extract the resonance frequencies of the three hybridized modes over the course of the measurement by fitting three individual Lorentzian lineshapes to the spectra shown in Fig. 11.9a. The extracted mode frequencies are shown as blue circles in Fig. 11.9b. Note that no frequencies could be extracted from the central branch for $(\Omega_{\mathrm{A}}^{\mathrm{aux}} - \Omega_{\mathrm{A,n=2}}^{\mathrm{init}})/2\pi = 9\,\mathrm{kHz}$ to 11 kHz, since no peaks are discernible in the corresponding spectra. We now perform a calculation of the hybridized mode frequencies $\Omega_{\mathrm{A,B,C}}$ over the course of the experiment. This is accomplished by solving Eq. 8.15 with the stiffness matrix of the network[8] derived in Eq. 11.1, under consideration of the auxiliary drive $\Omega_{\mathrm{A}}^{\mathrm{aux}}$ applied in the experiment. More information about the calculation can be found in App. A.8. The calculated mode frequencies are shown as solid orange lines in panel **b.** Note that we choose to limit the model calculation to $(\Omega_{\mathrm{A}}^{\mathrm{aux}} - \Omega_{\mathrm{A,n=2}}^{\mathrm{init}})/2\pi > 3\,\mathrm{kHz}$ in order to avoid the strongly non-linear heating effects that appear at the beginning of measurements (see discussion in Sec. 11.2.1). As discussed in the same context, we also incorporate a linear correction term into the model to compensate the remaining, more linear heating effects during the remainder of the measurement. Comparing the model calculation to the extracted data in Fig. 11.9b, we observe a remarkably good quantitative agreement and only slight deviations in the central branch frequencies towards the end of the measurement. The latter can be most likely attributed to the finite precision with which resonators B and C can be tuned on resonance during the initialization prior to the experiment.

Having successfully replicated the dispersion of the hybridized modes during the measurement, in the following we want to focus on a quantitative investigation of the *dark-mode* itself. To this end, we evaluate the displacement amplitude of this dark mode along the center branch (dashed cyan area), as shown in Fig. 11.9c. The data points correspond to the integrated spectral density between the dashed cyan lines, resulting in an average displacement amplitude $\langle |x_{\mathrm{B}}|^2 \rangle$ as a function of the auxiliary drive. Spectra where no resonance peak is discernible by eye have been marked in black, indicating the data-range where the mode goes *dark* and only spectral density of the noise-floor is measured. Clearly, the visual observation of a vanishing signal is also confirmed in the analysis of the data as the measured displacement temporarily drops below $0.1\,\mathrm{pm}^2$ around $(\Omega_{\mathrm{A}}^{\mathrm{aux}} - \Omega_{\mathrm{A,n=2}}^{\mathrm{init}})/2\pi \approx 10\,\mathrm{kHz}$. Based on the previously derived

[8] In this measurement we are examining the exact same network that was used to extract the inter-resonator coupling rates in Fig. 11.6 and Eq. 11.1. Therefore, we use the experimentally determined coupling rates for the calculation.

model for the dispersion of the hybridized modes, we now perform a calculation of the expected displacement amplitude. In particular, we evaluate the system of three coupled equations of motion of the nanostring network (Eqs. 8.24-8.26). Numerically solving[9] the system at the previously calculated resonance frequencies of the hybridized mode allows us to calculate an expected amplitude coefficient proportional to the displacement $|x_B|^2$ of nanostring B for any point along the central branch. The result of the calculation is plotted as purple line in Fig. 11.9c on a suitable scale to match the non-normalized experimental data. The model shows excellent agreement with the experimental data, correctly predicting the vanishing displacement for $(\Omega_A^{aux} - \Omega_{A,n=2}^{init})/2\pi \approx 8\,\text{kHz}$ to 12 kHz. The discrepancy towards the end of the measurement, which predicts a slightly larger increase in amplitudes, is likely the consequence of the previously discussed inaccuracies in the calculated frequencies of the hybridized modes, as seen in panel **b.** Notably, the fact that the model predicts amplitudes even lower than those experimentally observed is expected, given that most data points in proximity to the minimum represent the integrated noise floor of the experiment (black dots) instead of physical features. In fact, in the theoretical model, the displacement drops to less than 0.2% of its maximum value, which further corroborates the interpretation that a true, physical *dark-mode* is exhibited by the network. Consequently, we are confident that the employed models accurately and quantitatively describe the physical phenomenon observed in this experiment.

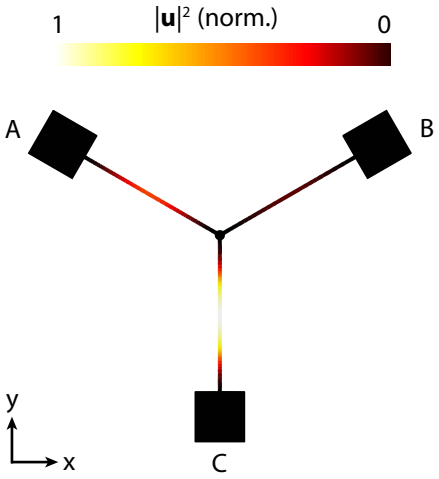

Figure 11.10: FEM simulation of the displacement field $\vec{u}$ of the investigated resonator network, assuming absolutely identical nanostrings with $\tilde{\Omega}_A = \tilde{\Omega}_B = \tilde{\Omega}_C$. We observe a vanishing displacement of nanostring B, providing a physical interpretation how the *dark-mode* is distributed over the network.

Finally, we perform a FEM simulation[10] of the investigated *Tri (Series A)* network in order to gain insight into the physical distribution of the *dark-mode* across the network. A visual representation of the simulated displacement field $\vec{u}$ for one of the possible eigenfrequency solutions[11] is presented in Fig. 11.10. The simulation assumes absolutely identical nanostrings with matching undisturbed resonance frequencies $\tilde{\Omega}_A = \tilde{\Omega}_B = \tilde{\Omega}_C$, which corresponds exactly

[9] For more information regarding the numeric calculation of the resonator amplitude, please refer to App. A.9.
[10] The simulation was performed using the finite element solver *COMSOL Multiphysics* [80]
[11] Due to the perfect rotational symmetry of the model structure, in fact, three solutions for the fundamental mode are found, only differing in rotations of 120° in the x-y-plane.

to the desired state of the network after the tuning sequence brings all of the nanostrings in resonance. Examining the simulated displacement field (color), we can clearly identifiy the strongly suppressed displacement amplitudes of nanostring B in comparison to the remaining strings, effectively forming a *dark-mode*.

In summary, we successfully observed the formation of mechanical dark-modes, a phononic analogue to coherent population trapping, in a strongly coupled three-nanostring resonator network. Subsequently, we replicated the experimental observations quantitatively with a simple theoretical model and visualized how the corresponding mode shape is distributed over the network using FEM simulations.

11.3 Transition Dynamics of Resonator Networks

In 1932, Landau [127] and Zener [128] analytically described the tunneling behavior of quantum-mechanical excitations between two states in a quantum two-level system during the passage through an avoided crossing (see Sec. 8.2.1). However, it was later shown that the exchange of excitations in coupled mechanical systems can be accurately described by the same dynamics [99, 129, 130]. A key requirement for establishing nanomechanical resonator networks as suitable systems for phonon-based information processing or storage is the ability to perform consistent, targeted transfer of phonons between coupled nanostring resonators [104, 131], we dedicate this section to demonstrate this ability in our multi-resonator networks by performing a classical Landau-Zener-type experiment [103] and comparing the results to the theoretical prediction. Subsequently, we attempt to exact more sophisticated control on the observed excitation transfer using the selective eigenfrequency tuning technique, laying the groundwork for targeted phonon transfer to arbitrary resonators in a multi-resonator network.

11.3.1 Excitation Transfer Measurement Protocol

All experiments in this section have been performed with the time-domain measurement setup introduced in Sec. 10.3. In the following, we will describe the measurement protocol presented in Fig. 11.11, which has been employed for the Landau-Zener-type excitation transfer experiments: At first, a short excitation pulse ($t_\mathrm{p} = 400\,\mu\mathrm{s}$, amplitude U_p) with the frequency $\Omega_\mathrm{p} = \Omega_\mathrm{A}^0$ [12], is generated by a pulsed RF source. After a waiting time $t_0 = 1\,\mathrm{ms}$, the AWG begins emitting its previously programmed auxiliary drive sequence with an amplitude of U_AWG[13], smoothly transitioning its output signal from Ω_aux^0 to $\Omega_\mathrm{aux}^0 + \Delta\Omega_\mathrm{aux}$ at a determined ramp rate $\zeta = \frac{\Delta\Omega_\mathrm{aux}}{\tau}$, thereby increasing the eigenfrequency of the excited resonator and causing it to pass through avoided crossings with both other resonators in the network. Over the course of the entire sequence, the digitizer card acquires the detector's photo-voltage signal with a sampling rate of $200 \cdot 10^6$ samples/s, gathering time resolved information about the displacement of the observed

[12] For simplicity, the excitation pulse is assumed to match the frequency of resonator A, Ω_A^0. Generally, the resonator with the lowest eigenfrequency will be initialized, allowing it to be tuned upwards by the auxiliary drive sequence, crossing the eigenfrequencies of both other resonators in the network.

[13] Different pulse amplitudes U_p and auxiliary drive voltages U_AWG have been employed for different measurements. Exact values are found in the figure captions.

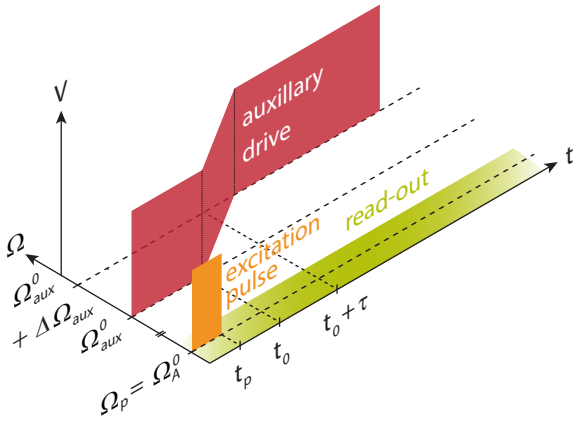

Figure 11.11: Measurement protocol for a Landau-Zener-type excitation transfer experiment. A detailed description can be found in the main text. The figure is adapted from Ref. [105].

nanostring resonator. In post-processing the time-domain data is digitally downconverted, downsampled and lowpass-filtered to a cutoff-frequency of 25 kHz. Due to the short timescales the experiment operates on, the synchronization of the individual components is of utmost importance for its success. For this purpose, a second channel of the AWG is programmed to send a trigger pulse to the RF source and the digitizer card at the start of the measurement, simultaneously launching the excitation pulse and the acquisition of data. The measurement is then repeated for varying ramp times ($\tau = 0.2$ ms to 12 ms) and laser spot positions on different resonators in order to investigate the influence of the ramp rate on inter-resonator excitation transfer.

11.3.2 Landau-Zener Transitions in Tri Resonator Networks (Series A)

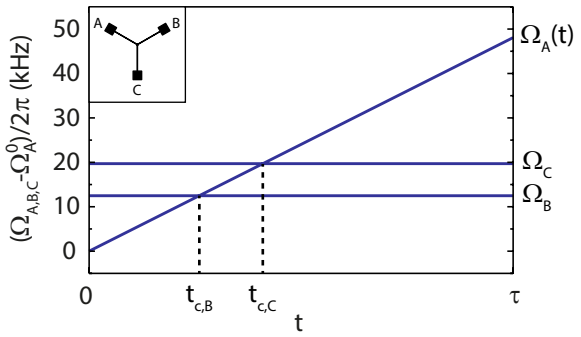

Figure 11.12: Level scheme of the nanostring network investigated in this section as a function of the measurement time t. Shown are the resonance frequencies $\Omega_{A,B,C}$ of the three corresponding resonators (see inset). Ω_A is tuned upwards, eventually crossing the frequencies Ω_B and Ω_C for times $t_{c,B}$ and $t_{c,B}$ respectively. For finite inter-resonator coupling, avoided crossings will form and allow the transfer of excitation between resonators. For clarity, we neglect the coupling in this illustration and do not consider the hybridization of modes.

We now perform a Landau-Zener transition sequence, as detailed in Sec. 11.3.1, on a *Tri (Series A)* nanostring network. In the measurement, we record the time-resolved development of the

displacement of nanostrings A, B and C as a function of the ramp rate ζ. In order to evaluate experimental data of a Landau-Zener-type measurement, it is crucial to understand the dispersion of the eigenfrequencies over the course of the performed sequence. To this end, we illustrate the *level scheme*, i.e. the eigenfrequencies of the investigated nanostring network, as a function of the measurement time t in Fig. 11.12. During the measurement, the eigenfrequency $\Omega_\mathrm{A}(t)$ resonator A is increased using the established tuning technique. The frequencies of the remaining resonators are unaffected by this, so that eventually $\Omega_\mathrm{A}(t)$ will become resonant with Ω_B and Ω_C at points in time $t_\mathrm{c,B}$ and $t_\mathrm{c,C}$ respectively (see illustration). Due to the finite inter-resonator coupling in the network, the eigenfrequencies will instead hybridize and pass through an avoided crossing, where the transfer of energy between the corresponding resonators becomes possible (not shown in the figure). Keeping this in mind, we now investigate the measurement results presented in Fig. 11.13a-c.

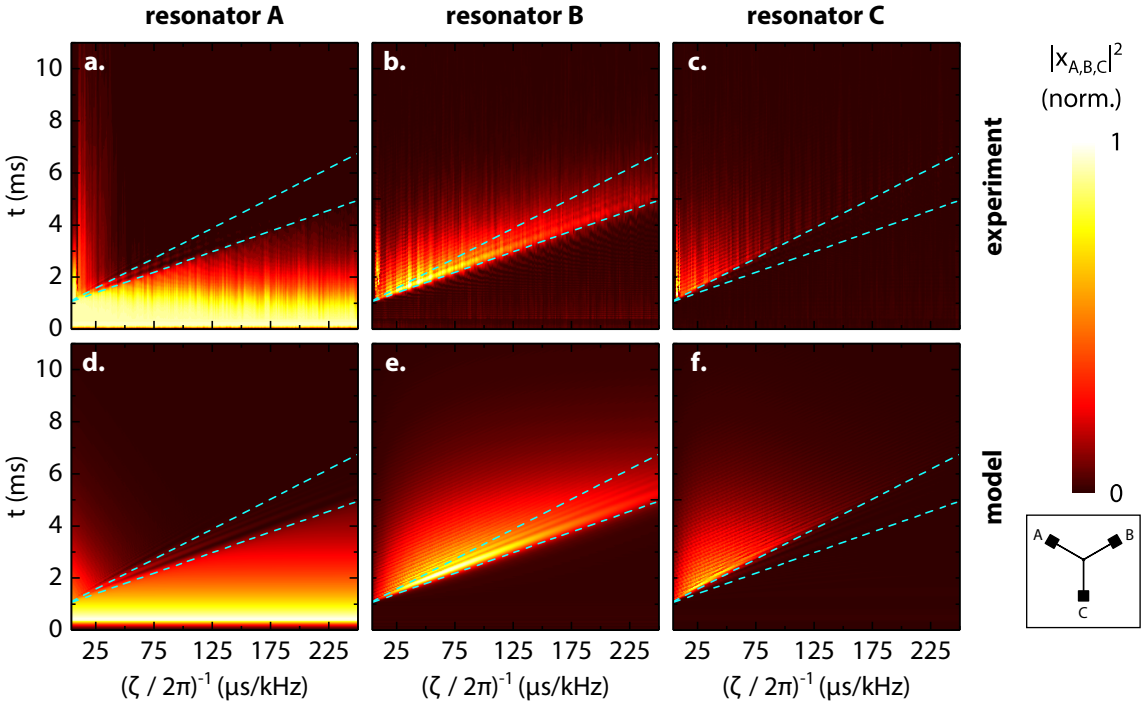

Figure 11.13: a-c. Experimentally observed squared displacement amplitude of the fundamental mode of resonator A, B and C, respectively, in a *Tri (Series A)* network (shown in the lower right) as a function of auxiliary frequency ramp rate ζ and time t. The signal voltages used for this measurement are $U_\mathrm{p} = 70\,\mathrm{mV_{rms}}$ and $U_\mathrm{AWG} \approx 4.5\,\mathrm{V_{rms}}$. **d-f.** Model calculation for the squared displacement amplitude of resonators A, B and C, respectively, based on numerically solving the three time-dependent, coupled equations of motion presented in Sec. 8.2.2. **a-f.** The dashed cyan lines indicate calculated crossing times for which Ω_A is resonant with Ω_B (lower line) and Ω_C (upper line). We observe high quantitative agreement between experimental data and model predictions.

We begin the discussion of the experimental data by considering the case of slow ramp rates, i.e $(\zeta/2\pi)^{-1} > 100\,\mu\mathrm{s/kHz}$. By examining the development of the displacement amplitudes (color) in the vicinity of the calculated crossing times (dashed cyan lines), a distinct transfer of energy between the resonators due to the inter-resonator coupling can be seen. For example, the

displacement measured on resonator A (see panel **a.**) practically vanishes as soon as t exceeds the predicted time of the first crossing, i.e. the point in time for which $\Omega_\mathrm{A}(t) = \Omega_\mathrm{B}$. At the same time, an increased signal can be observed in panel **b.**, corresponding to a displacement of resonator B. This can be interpreted as an adiabatic transfer of energy from resonator A to resonators B. The transfer is performed at the time of passage through the avoided crossing in accordance with the Landau-Zener model (see Sec. 8.2.1), which predicts the adiabatic passage for slowly changing frequencies. The fact that a majority of the energy of resonator A is transferred becomes especially apparent when considering panel **c.** The displacement of resonator C stays close to zero even after resonator A crosses its frequency (upper dashed line) with the same slow rate. Clearly, resonator A barely retains any energy after the previous avoided crossing with resonator B.
For faster ramp rates of $(\zeta/2\pi)^{-1} \approx 50\,\mu\mathrm{s/kHz}$ on the other hand, we observe a significant signal in panel **a.** for t larger than both crossing times, and it can subsequently be seen decaying exponentially. Therefore, energy remains stored in resonator A even after passing through the avoided crossings with resonators B and C, pointing towards the diabatic passage behavior that the model predicts for large ramp rates. However, since we also observe signals in panels **b.** and **c.**, energy is still transferred to resonators B and C. We can conclude that the system has not yet fully arrived at diabatic behavior and still resides in a transition region. Moving to extremely high ramp rates over $(\zeta/2\pi)^{-1} \approx 10\,\mu\mathrm{s/kHz}$, we eventually reach a regime in which the eigenfrequency tuning mechanism breaks down and Ω_A can no longer be tuned upwards to cross the other resonator's eigenfrequencies. Subsequently, we observe a simple exponential decay of the energy stored in resonator A and no transfer of energy to the other strings. This breakdown is attributed to the bandwidth of the higher order mode, limiting the Duffing oscillator's ability to perform high amplitude oscillations long enough for the frequency shift to take effect (cf. Ref. [105]). Since no crossings can be provoked without the tuning of the resonators frequency, this presents an upper limit for the investigated ramp rates. Consequently, in order to gain access to even higher ramp rates and fully explore the diabatic transition regime, the bandwidth of the auxiliary mode employed for tuning has to be reduced, e.g. by special mode engineering [156, 157].
By numerically solving[14] the time-dependent, coupled equations of motion as derived in Sec. 8.2.2, we can subsequently model the transition behavior of our three-resonator network without the need for any free fit parameters, as demonstrated in Fig. 11.13d-f. Aside from the high-rate limit of the tuning mechanism that is not considered in the mathematical model, the calculation is able to quantitatively reproduce all of the experimentally observed features, including the small, interference-like patterns, that become visible around the crossings (see e.g. the area between the crossings in panel **b.**) and can be explained by Rabi-like population oscillations in the network.

In conclusion, the employed sequence is capable of performing coherent transfer of excitations from one nanostring in a *Tri* resonator network to another and even a partial transfer to both mechanically coupled nanostrings, depending on the chosen frequency ramp rate.

[14] A sketch of the numerical calculation algorithm is found in App. A.10

11.3.3 Landau-Zener Transitions in Inline Resonator Networks

Next, we proceed by performing an identical, classical Landau-Zener experiment on an *Inline* nanostring network. Recalling that the resonators A and C are not coupled in this network design, we choose the investigated network to fulfill $\Omega_B^0 < \Omega_A^0 < \Omega_C^0$, since this will allow us the investigation of two successive avoided crossings in one tuning sequence. To clarify the dynamics of the measurement, we present the level scheme of the investigated network in Fig. 11.14. In

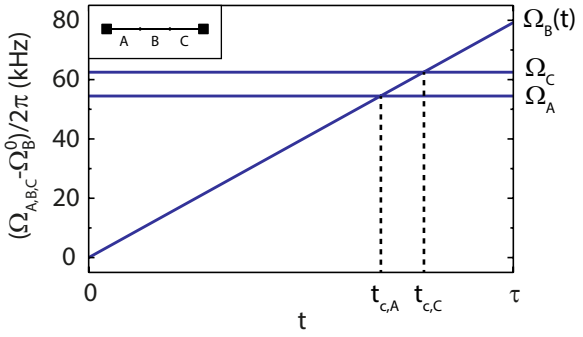

Figure 11.14: Level scheme of the *Inline* nanostring network investigated in the following section as a function of the measurement time t. Shown are the resonance frequencies $\Omega_{A,B,C}$ of the three corresponding resonators (see inset). Ω_B is tuned upwards, eventually crossing the frequencies Ω_A and Ω_C for times $t_{c,A}$ and $t_{c,C}$ respectively. For finite inter-resonator coupling, avoided crossings will form and allow the transfer of excitation between resonators. For clarity, we neglect the coupling in this illustration and do not consider the hybridization of modes.

this case resonator B is excited by the initialization pulse and tuned upwards by the tuning mechanism so that Ω_B will eventually become resonant with Ω_A and subsequently Ω_C. The resulting measurement data, tracking the nanostrings' displacement over the course of the Landau-Zener sequence for different ramp rates ζ, is presented in Fig. 11.13a-c.
We proceed as above and first investigate the case of slow ramping rates, i.e. $(\zeta/2\pi)^{-1} > 30\,\mu$s/kHz. Examining panel **b.**, which shows the measured displacement of resonators A, we can clearly identify the appearance of **a.** measurement signal as soon as the t exceeds $t_{c,A}$ (first dashed line), i.e. the calculated time of the avoided crossing between resonators B and A. Similar observations can be made in panel c, i.e. the displacement of resonator C, where a signal becomes visible only above the second dashed line, indicating the relevant crossing. This confirms that a transfer of excitations at the avoided crossings is performed. However, upon examination of the measured displacement of resonator B (panel **a.**), we find no visually discernible loss of energy in the area of the predicted crossing times, even for extremely slow ramp rates (i.e. $(\zeta/2\pi)^{-1} > 130\,\mu$s/kHz. Instead the signal shows a simple exponential decay. We attribute this to the significantly weaker inter-resonator coupling rate that was experimentally determined in this type of network (see Sec. 11.2.2). Due to the lower coupling strength, the energy transferred from resonator B to the resonators A and C at the avoided crossing appears to be small enough for its absence to not be visually discernibly in the colorcode. Nonetheless, we proceed to investigate the characteristic features of Landau-Zener experiments. For ramp rates $(\zeta/2\pi)^{-1} < 30\,\mu$s/kHz, we can identify features that point towards an increasingly diabatic passage. In particular, the displacement in panel **b.** can be seen to drop below the

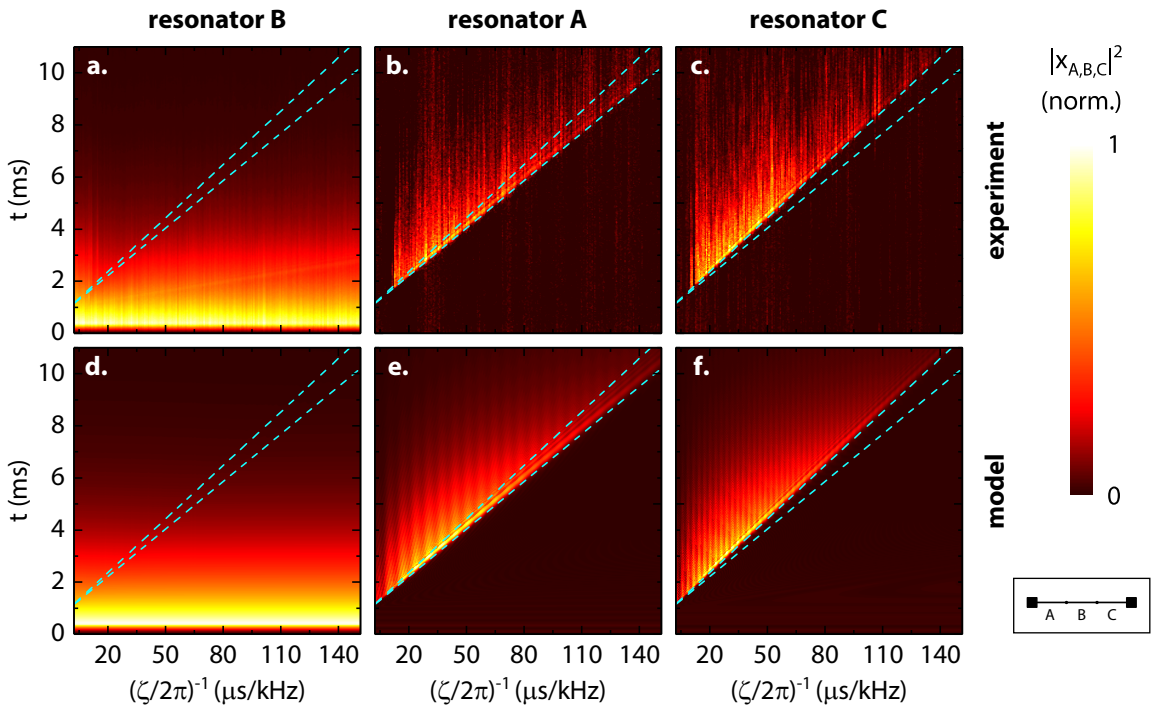

Figure 11.15: **a-c.** Experimentally observed squared displacement amplitude of the fundamental mode of resonator B, A and C, respectively, in a *Inline* network (shown in the lower right) as a function of auxiliary frequency ramp rate ζ and time t. The signal voltages used for this measurement are $U_\mathrm{p} = 125\,\mathrm{mV_{rms}}$ and $U_\mathrm{AWG} \approx 7\,\mathrm{V_{rms}}$. **d-f.** Model calculation for the squared displacement amplitude of resonators B, A and C, respectively, based on numerically solving the three time-dependent, coupled equations of motion presented in Sec. 8.2.2. **a-f.** The dashed cyan lines indicate calculated crossing times for which Ω_B is resonant with Ω_A (lower line) and Ω_C (upper line). Due to the small inter-resonator coupling rates, the amount of transferred energy is comparatively low, leading to noisy measurements that do not resolve smaller features. Still, we observe good agreement between experimental data and model predictions.

detection threshold earlier as we move to faster ramp rates. In particular, take note of the disappearance of the red color at around 7 ms for $(\zeta/2\pi)^{-1} = 20\,\mu\mathrm{s/kHz}$, while for slightly higher rates the decay can be visually tracked over the full measurement duration. For ramp rates $(\zeta/2\pi)^{-1} < 10\,\mu\mathrm{s/kHz}$, the signal vanishes entirely from panels **b.** and **c.**, signaling that we once again encountered the limit of the eigenfrequency tuning technique and no more crossings are induced. Notably, the breakdown appears more prominently in this measurement. This can be explained by the larger frequency range (80 kHz compared to 50 kHz in the previous measurement) which Ω_B needs to traverse in order to reach the eigenfrequencies of the other resonators. Therefore, using the same ramp times τ, we accessed higher ramp rates ζ in this measurement. Lastly, the comparison of the experimental data with the theoretical model (see Sec. 8.2.2 and App. A.10) presented in Fig. 11.13d-f shows reasonably good agreement. However, the small amplitudes observed on nanostrings A and C suffer from a low signal-to-noise ratio and can only partially resolve the small, oscillatory features predicted by the model.

In summary, even though the low inter-resonator coupling rate does not allow for truly adiabatic

transport of excitations in this particular sample, Landau-Zener transition dynamics between all coupled nanostrings in the *Inline* network have been successfully demonstrated. It seems highly plausible that with comparatively simple changes to the geometry of the network (e.g. smaller shared support area) the inter-resonator coupling rates could be enhanced, bringing the network deeper into the strong coupling regime and towards similar performance to the investigated *Tri* network design, regarding the coherent transfer of excitations.

It should be noted that an interesting research application for the *Inline* resonator design would be the investigation of mechanical analogues to more complex adiabatic passage phenomena. In particular, stimulated Raman adiabatic passage (STIRAP) [158] and coherent tunneling adiabatic passage (CTAP) [159, 160] are concerned with population transfer between two uncoupled states by coupling them via an intermediate state. A natural mechanical analogue would be the transfer of phonons from resonator A to resonator C in *Inline* nanostring networks. Unfortunately, in the sample shown in this section, frequency crowding prevented the necessary tuning operations to bring resonators A and C on resonance, rendering an investigation of this topic challenging. However, with a suitable sample, nanostring networks might be viable candidates to explore the possibility of a phononic analogue to STIRAP.

11.3.4 Controlling Transition Dynamics in Resonator Networks

Having successfully demonstrated coherent excitation transfer in multi-resonator networks, we want to conclude the examination of transition dynamics by performing a proof-of-principle experiment, showcasing the possibility for the transfer protocol to be improved towards truly targeted transfer of phonons. In particular, we show the stability of the protocol against additional eigenfrequency tuning operations, allowing for flexible configuration of the avoided crossings in

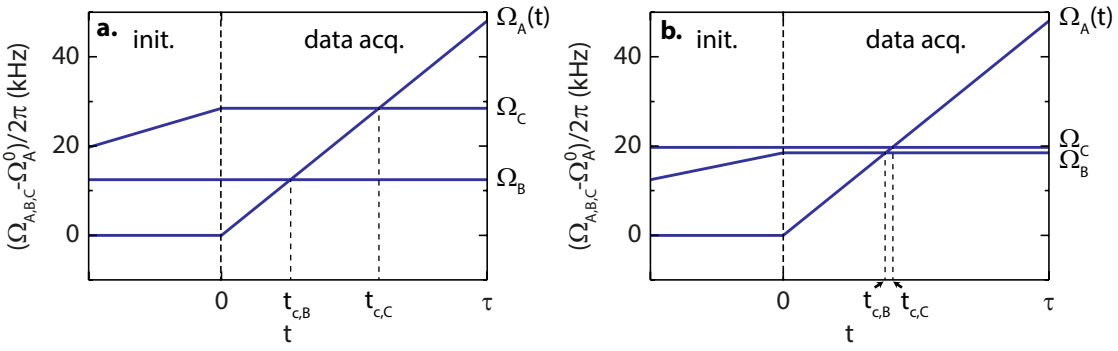

Figure 11.16: Level schemes of the investigated *Tri (Series A)* network over the course of two different Landau-Zener measurements. **a.** Level scheme for the *off resonance* case. Prior to $t = 0$ an initialization operation (init.) is performed to increase Ω_C. In the measurement (data acq.) Ω_A is tuned upwards and the crossing times $t_{c,B}$ and $t_{c,C}$ are well separated. **b.** Level scheme for the *on resonance* case. In a initialization sequence (init.) prior to $t = 0$, Ω_B is increased to a level close to Ω_C, where the two modes already hybridize (not shown). In the measurement (data acq.) Ω_A is tuned upwards and passes through Ω_B and Ω_C at very similar times $t_{c,B} \approx t_{c,C}$. **a-b.** In both illustrations, inter-resonator coupling and the hybridization of modes is neglected.

the network. To this end, we perform to slightly different Landau-Zener type measurements on the exact same network that has been investigated in Sec. 11.3.2. The performed Landau-Zener sequences are completely identical, but an additional initialization operation is performed prior to the acquisition of data, altering the eigenfrequencies of certain resonators in the network. The corresponding level schemes are illustrated in Fig. 11.16. In panel **a.**, we show the level scheme for the *off resonance* measurement run. In the initialization operation, an additional auxiliary drive signal is employed to tune Ω_C upwards leaving the resonators B and C far off resonance. Therefore, in the main measurement, the two crossings passed by Ω_A are widely separated in time and frequency. Conversely, the level scheme for the *on resonance* measurement run is shown in panel **b.** In the initialization sequence prior to the measurement, Ω_B is increased by an auxiliary drive such that $\Omega_B \approx \Omega_C$ and the two modes begin to hybridize (not shown in the illustration). In the main measurement, Ω_A then passes through both frequencies almost simultaneously. It should be pointed out that, after initialization, the employed auxiliary signal needs to be remain enabled and constant throughout the main measurement, as the resonance frequencies would otherwise revert back to their initial values.

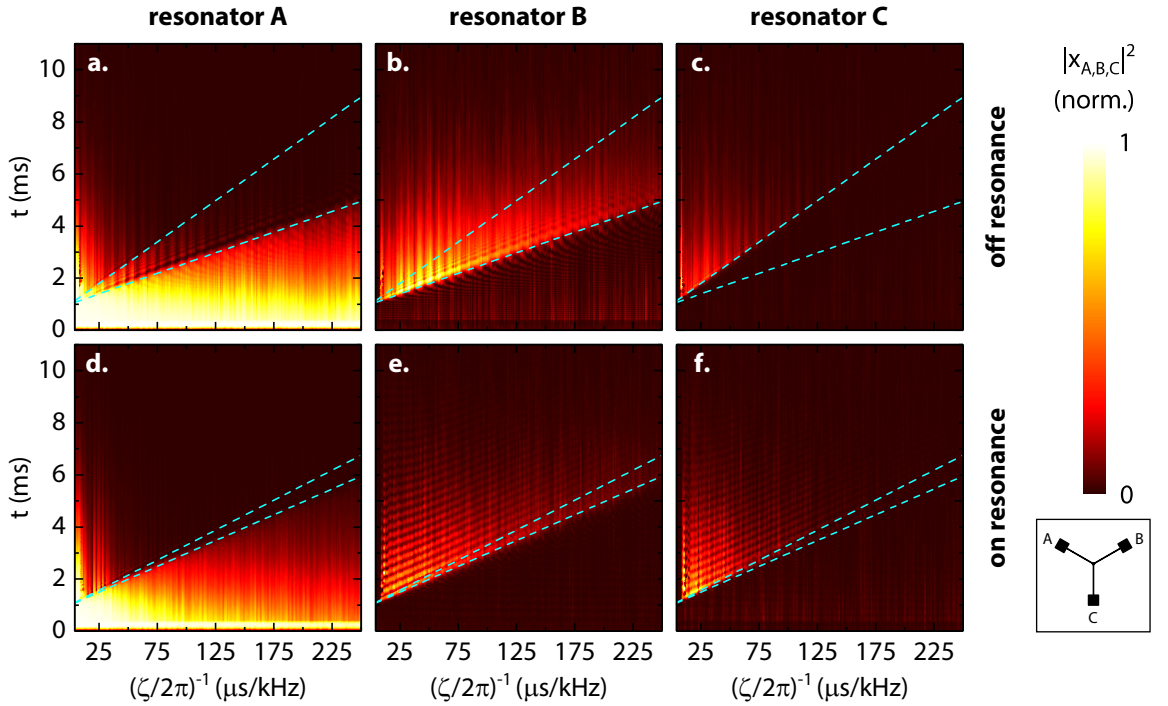

Figure 11.17: Experimentally observed squared displacement amplitude of the fundamental mode of resonators A, B and C as a function of auxiliary frequency ramp rate ζ and time t for two different experimental runs. Prior to each measurement, certain resonance frequencies have been initialized to new levels by an auxiliary drive with $U_{\mathrm{aux}} \approx 5\,\mathrm{V_{rms}}$ (see Fig. 11.16). **a-c.** shows data of a off-resonant measurement, for which Ω_B and Ω_C were tuned far apart. **d-f.** shows data of a *on resonance* measurement, for which Ω_B and Ω_C have been initialized to be close to resonance. **a-f.** All measurements are performed in the same *Tri (Series A)* network previously investigated in Sec. 11.3.2 with an identical Landau-Zener sequence and the same signal voltages $U_{\mathrm{p}} = 70\,\mathrm{mV_{rms}}$ and $U_{\mathrm{AWG}} \approx 4.5\,\mathrm{V_{rms}}$. The dashed cyan lines indicate calculated crossing times for which Ω_A is resonant with Ω_B (lower line) and Ω_C (upper line).

The experimental results for both measurements are presented in Fig. 11.17. Comparing the acquired data between the two different measurement, it can be seen that the position of the avoided crossings is significantly influenced by the initialization operations. For example, in the off resonant case shown in panel **a.**, we clearly find the influence of two distinct crossings along with a transfer of energy, as the displacement of resonator A significantly decreases at each of the calculated crossing times (dashed lines). In the *on resonance* measurement data of the same resonator (panel **d.**) on the other hand, the influence effect of the individual crossings can no longer be visually separated. Instead we find the signal to vanish almost completely as soon the first crossing is reached. This indicates an almost simultaneous transfer of a majority of the energy in resonator A to both of the crossed resonators. Notably, characteristic features of Landau-Zener measurements are still found in both measurements, i.e. the adiabatic or diabatic passage through the crossings depending on the ramp rate. The expected dependency is clearly visible in panels **a.** and **d.** However, since these features were already discussed in Sec. 11.13 based on a measurement of the exact same network, we will not perform an in-depth analysis at this point. It should be noted that the main goal of this proof-of-principle experiment was successfully accomplished. We demonstrated that the eigenfrequency tuning mechanism can not only be used to perform coherent transfer of excitations via Landau-Zener sequences, but can also be used to initialize the system in a desired state prior to the measurement. Notably, this opens up the possibility of targeted excitation transfer between arbitrary resonators in the network. For example, the most challenging process in the investigated network is a direct transport of energy from resonator A to resonator C without affecting resonator B. By tuning the eigenfrequency of resonator B, Ω_B, to exceed Ω_C, this can be accomplished by a simple adiabatic ramp of Ω_A. Unfortunately this particular sequence could not be performed in the investigated sample due to frequency crowding.

Note that an equivalent protocol to accomplish an adiabatic excitation transfer from resonator A to C would be to first increase Ω_A very rapidly to (diabatically) transition Ω_B and subsequently perform a slower, adiabatic transition across Ω_C, thus transferring the excitation to resonator C while leaving resonator B undisturbed. However, as discussed previously, this would require a reduction of the auxiliary mode bandwith in order to gain access to the fast frequency ramp rates necessary for truly diabatic transitions.

We conclude that the demonstrated control of resonance frequencies during execution of the Landau-Zener protocol is a valuable step towards the goal of universal, targeted excitation transfer in mechanical resonator networks, which remains, at the time, primarily limited by frequency-crowding effects.

Chapter 12

Summary

Throughout the second part of this thesis, we investigated and characterized the interaction of multiple high-Q nanostring resonators which are mechanically coupled to form a multi-resonator network. We designed three distinct resonator network geometries and adapted the established fabrication process to reliably produce the structures from thin, tensile stressed Si_3N_4 films.

In optical interferometry measurements, we characterized individual nanostrings within different network geometries regarding their quality factors and material parameters. The resulting parameters proved consistent with literature values and confirmed the excellent quality factors expected of Si_3N_4 nanostring resonators. Subsequently, we evaluated the capabilities of the recently introduced, mechanical eigenfrequency tuning technique based on the geometric non-linearity of nanostrings. We demonstrated simultaneous and individual control of the eigenfrequencies of up to three resonators in the same network without requiring local control gates. In the next step, the inter-resonator coupling rates between individual nanostrings in the same multi-resonator network were quantified. Strong coupling was observed in all of the investigated samples and a significant influence of the network geometry on the coupling rates was found. Consequently, several geometric parameters were identified which can be used to manipulate specific inter-resonator coupling rates at the design stage.

In addition, we investigated the formation of mechanical dark-modes in a system of three strongly coupled nanostring resonators. Mechanical dark-modes represent an interesting quantum-classical analogue to electromagnetically induced transparency and coherent population trapping. We successfully prompted the formation of a mechanical dark mode and quantitatively analyzed the experimentally observed behavior. The vanishing displacement of one of the nanostrings and the dispersion of the underlying hybridized modes could be accurately replicated by a mathematical model derived directly from the classical equations of motion. Subsequently, the physical distribution of the dark-mode across the resonator network was visualized by FEM simulations. Finally, we explored transition dynamics within nanostring resonator networks by performing Landau-Zener-type experiments. We successfully demonstrated the controlled transfer of excitations between coupled nanostring resonators and presented a mathematical model that quantitatively describes the dynamics of mechanical Landau-Zener transitions. In

addition, we performed a proof-of-principle experiment opening the possibility to extend the employed transfer protocol towards truly targeted transfer of phonons in larger multi-resonator networks.
In conclusion, we have realized three different designs of nanostring resonator networks and demonstrated strong inter-resonator coupling, all-mechanical eigenfrequency control of individual resonators and the coherent transfer of phonons within the network.

Conclusion and Outlook

Concluding the thesis is a brief summary of the results achieved within and an outlook on the next steps and long-term perspectives:
We successfully established a fabrication process for the magneto-mechanical hybrid systems designed in the first part of the thesis. Unfortunately, due to an unstable sample material and the breakdown of an important measurement setup, no in-depth evaluation could be performed regarding the suitability of the new platform for the investigation of magnon-phonon coupling. Consequently, in a next step, the sample material should be replaced with a thicker Si_3N_4 or Si layer. The resulting samples can then be examined in micro-focused BLS spectroscopy measurements, testing the existence of a complete phononic band gap and the localization of GHz-frequency phonons. Notably, the magnon-modes exhibited by the samples fabricated for this thesis were found to be significantly affected by the finite size of the phonon-engineered structures. Therefore, for the design of any future hybrid systems, it will be crucial to perform coordinated simulations of phononic and magnonic modes, using micromagnetical simulations [73, 95] in combination with the techniques for phonon engineering described in this thesis. It should then be possible to tune magnon modes on resonance with the localized phonon mode and study the effects of resonant magnon-phonon coupling. Given favorable results, a next step could be to cool down the system to mK temperatures and investigate the interaction in the quantum limit.
In the long term, it would further be conceivable to move towards more complex magnetic material systems in order to gain even more control over the magnon modes, a process that has been already demonstrated for periodic lattices of magnetic materials, forming *magnonic crystals* [161–164]. It has to be seen whether the concept can be combined with phononic crystals. However, should it be possible to simultaneously localize magnon- and phonon modes to the same crystal structure, this would represent a new class of *magnetomechanical crystals*, promising a similarly wide range of applications as their optomechanical counterparts.

The nanomechanical multi-resonator networks fabricated in the second part of the thesis were shown to fulfill all three of the requirements formulated at the beginning of this work: We demonstrated strong coupling rates, an all-mechanical eigenfrequency tuning technique, and a protocol to perform controlled transfer of excitations. Moreover, every one of these experimentally observed features could be quantitatively described by a mathematical model. As such, the

fabricated networks fulfill three essential requirements for applications towards the mechanical simulation of fundamental quantum mechanics [101, 104] as well as phonon-based quantum information processing [107–109] and storage [110–112]. In a next step, special attention should be given to the issue of frequency crowding, which currently poses limits on the ability to perform truly targeted transfer of excitations between all resonators in larger networks. If the design and fabrication process of nanostrings can be improved to produce more predictable resonance frequencies, networks could be more reliably fabricated to exhibit a desired distribution of modes. Subsequently, more complex phonon transfer protocols could be realized as alluded in the final proof-of-principle experiment. In particular, due to its geometry, the *Inline* network appears to be an intuitive candidate for experiments towards a phononic analogue to stimulated Raman adiabatic passage (STIRAP) [158] and coherent tunneling adiabatic passage (CTAP) [159, 160]. Another interesting long-term perspective is to investigate nanomechanical resonators or resonator-networks close to their quantum mechanical ground state [110]. With resonance frequencies in the MHz regime, this can not be solely achieved by a cooldown of the system to mK temperatures. The ground state cooling of MHz modes was realized by coupling of mechanical resonators to a microwave- or optical cavity [26]. However, the high oscillation amplitudes of harmonic modes essential for the eigenfrequency tuning technique can potentially pose additional challenges when moving towards lower temperatures. Before experiments in the quantum limit can be approached, it will be crucial to determine whether mode-mode coupling between the fundamental and the higher harmonic modes could counteract attempts to cool the fundamental mode to its ground state.

Appendix A

Appendix

A.1 Derivative Divide

In Chapter 5, we display and fit the transmission spectra of FMR measurements in the form of its *derivative divide* as introduced in Ref. [88]. The corresponding expression is

$$\partial_D S_{21} = -i\omega A' \frac{\chi(\omega + \Delta\omega_{\mathrm{mod}}) - \chi(\omega - \Delta\omega_{\mathrm{mod}})}{2\Delta\omega_{\mathrm{mod}}} \tag{A.1}$$

with the angular probe frequency $\omega = 2\pi f$, an amplitude factor A' and a variable step size $\Delta\omega_{\mathrm{mod}}$ for the numeric computation. Furthermore, χ is the magnetic susceptibility

$$\chi(\omega, H_0) = \frac{\gamma\mu_0|M|(\gamma\mu_0 H_0 - i\Delta\omega)}{(\omega_{\mathrm{res}}(H_0))^2 - \omega^2 - i\omega\Delta\omega} \tag{A.2}$$

using $H_0 = \left|\vec{\mathbf{H_0}}\right|$ as static magnetic field and the gyromagnetic ratio γ. This allows us to extract the angular resonance frequency ω_{res} and the linewidth $\Delta\omega$. It should be noted that the simple dependence of χ on H_0 holds only for neglected magnetic anisotropy. For more information please refer directly to Ref. [88].

A.2 Complex Lorentzian Fit Model

Theoretically, the response spectrum of a nanostring resonator, i.e. its squared displacement amplitude $|x_0|^2(\Omega)$ in response to the angular frequency Ω is given by a Lorentzian lineshape of according to Eq. 8.3. In experiments however, one regularly observes deviations from theory, e.g. an asymmetric lineshape, which can be caused by impedance mismatches or other effects in the readout electronics. Many of these effects can be compensated by employing a slightly altered lineshape to fit the data.
In particular, we assume a complex background ic_1 added to the measured signal, resulting in a modified Lorentzian lineshape of

$$S^{\mathrm{meas}}(\Omega) = a\left|ic_1 + \frac{\Gamma}{i(\Omega - \Omega_{\mathrm{m}}) + \Gamma_{\mathrm{m}}/2}\right|^2 + c_2. \tag{A.3}$$

Here $S^{\text{meas}} \propto |x_0|^2$ is the measurement signal proportional to the squared displacement of the string, Ω_{m} and Γ_{m} the extracted resonance frequency and linewidth respectively. Further a is an amplitude factor and c_2 a correction term for a real background.

Throughout this thesis we use Eq. A.3 for all fits of nanostring resonance frequencies. Note that the fitting model is based on a similar treatment for microwave transmission measurements found in Ref. [118].

A.3 Linear Chain of Masses

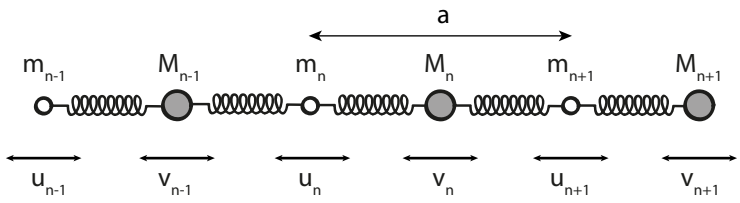

Figure A.1: A linear chain of alternating masses m and M which are connected by springs with a fixed, identical spring constant κ. We denote the displacement of atoms m_n by u_n and the displacement of atoms M_n by v_n. The equilibrium distance between two identical masses is a.

Here, we derive the dispersion relation of a linear chain of alternating masses m and M on springs, as illustrated in Fig. A.1. In this simple model, we only consider the motion along the chain, i.e. in one dimension and assume that all masses are coupled by identical springs with a fixed spring constant κ. We further assume only nearest-neighbour coupling. With the expressions for the displacement of the masses from the illustration, we can write the equations of motions of the masses m_n and M_n [48]

$$\begin{aligned} m\ddot{u}_n &= \kappa(v_n - u_n) + \kappa(v_{n-1} - u_n) \\ M\ddot{v}_n &= \kappa(u_n - v_n) + \kappa(u_{n+1} - v_n) \end{aligned} \tag{A.4}$$

reducing to

$$\begin{aligned} m\ddot{u}_n &= \kappa(v_n + v_{n-1} - 2u_n) \\ M\ddot{v}_n &= \kappa(u_{n+1} + u_n - 2v_n). \end{aligned} \tag{A.5}$$

We use the periodicity of the chain and assume plane wave solutions of the form $u_n = ue^{i(nk_x a - \omega t)}$ and $v_n = ve^{i(vk_x a - \omega t)}$, resulting in

$$\begin{aligned} -\omega^2 mu &= \kappa v(1 + e^{-ik_x a}) - 2\kappa u \\ -\omega^2 Mv &= \kappa u(e^{ik_x a} + 1) - 2\kappa v. \end{aligned} \tag{A.6}$$

We can rewrite the expressions into the determinant form of an eigenvalue equation

$$\begin{vmatrix} 2\kappa - m\omega^2 & -\kappa(1 + e^{ik_x a}) \\ -\kappa(1 + e^{ik_x a}) & 2\kappa - M\omega^2 \end{vmatrix} = 0 \tag{A.7}$$

which becomes

$$mM\omega^4 - 2\kappa(m+M)\omega^2 + 2\kappa^2(1 - cos(k_x a)) = 0. \tag{A.8}$$

Solving Eq. A.8 for ω^2 results in two solutions

$$\omega_{\pm}^2(k_x) = \frac{\kappa}{mM}\left[m + M \pm \sqrt{(m+M)^2 - 4mMsin^2 qa}\right]. \tag{A.9}$$

Notably, for $m \neq M$ the two solutions for the dispersion $\omega_+^2(k_x)$ and $\omega_-^2(k_x)$ split up, forming two separated bands in the phononic bandstructure, which are drawn in Fig. 2.1.

A.4 Fabrication Processes

A.4.1 Zipper Resonator

The following is a detailed fabrication sequence for a Si_3N_4/Co double-layer zipper resonator surrounded by a Si_3N_4/Co phononic shield. The essential steps are summarized and illustrated in Sec. 4.1.

1. Clean new Si/SiO_2/Si_3N_4 chip by ultrasonic bath in technical acetone for 2 minutes, rinse in acetone and IPA, dry with N_2, briefly bake at 200°C.
2. Coat chip with positive EBL resist PMMA/MA(33%). Spin-coat for 60s at 4000RPM. Bake at 170°C for 2 minutes.
3. Define markers for alignment of subsequent steps by EBL process. 10x10μm^2 squares (mpsquare) work. Exposure dose 6.5 C/m^2.
4. Develop 2 minutes in AR 600-56 under constant motion, rinse 2x in IPA, dry with N_2.
5. Evaporate Ti(4nm)/Au(24nm) onto sample.
6. Lift off resist layer along with excess evaporated material in warm (70°C) acetone. After 20-30 minutes, remove dissolved material and transfer sample to new beaker. Repeat until resist layer is gone, rinse in acetone and IPA, dry with N_2.
7. Coat chip with positive EBL resist PMMA/MA(33%). See step 2.
8. Define zipper layout by EBL process. Exposure dose 4.55 C/m^2. Use slowest, most accurate database!
9. Develop resist as in step 4.
10. Evaporate Cobalt (20nm) layer onto sample.
11. Lift off resist layer, see step 6. If the Cobalt proves hard to remove, use dedicated remover (e.g. mr-rem700) instead of acetone and increase time between switching of beakers ($>$ 30 min).
12. Coat chip with positive EBL resist PMMA/MA(33%). See step 2.

13. Define negative shape of phononic shield, including the zipper, as etch mask by EBL process. Exposure dose 5.2 C/m^2 for shield, 4.55 C/m^2 for zipper. Use slowest, most accurate database!

14. Develop resist as in step 4.

15. Load sample to RIE and run job TL_NanomechanicsAnisotropic (SF6=20, Ar=10, RF Power=100W, ICP=30W, pressure=15, time=2min20s).

16. Wet etch sample in buffered hydrofluoric acid (BHF) solution (3%) at room temperature. At least 5 minutes are necessary for a freely suspended structure. Terminate in H_2O, transfer through several ethanol baths and keep sample submerged.

17. Dry sample in CPD. 25 cycles, slowest gas exchange rate.

A.4.2 Double-Layer Phononic Shields

The following is a detailed fabrication sequence for a Si_3N_4/Co double-layer phononic shield structure. The essential steps are summarized and illustrated in Sec. 4.2.

1. Clean new $Si/SiO_2/Si_3N_4$ chip by ultrasonic bath in technical acetone for 2 minutes, rinse in acetone and IPA, dry with N_2, briefly bake at 200°C.

2. Coat chip with negative EBL resist ma-N 2403. Spin-coat for 60s at 4000RPM. Bake at 90°C for 1 minute.

3. Define negative phononic shield structure by EBL process. Exposure dose 1.54 C/m^2. If Cobalt on the remainder of the chip is not wanted, expose complete chip in second EBL step.

4. Develop in ma-D 525: Wait 30s, briefly shake sample, wait another 30s (total: 1min).

5. Evaporate Cobalt layer of desired thickness plus $\approx$ 30 nm to compensate loss during wet etching. BHF attacks Co at roughly 30 nm per 5 minutes.

6. Lift off resist layer along with excess evaporated material in warm (70°C) acetone. After 20-30 minutes, remove dissolved material and transfer sample to new beaker. Repeat until resist layer is gone, rinse in acetone and IPA, dry with N_2. If the Cobalt proves hard to remove, use dedicated remover (e.g. mr-rem700) instead of acetone and increase time between switching of beakers ($>$ 30 min).

7. Load sample to RIE and run TL_NanomechanicsAnisotropic (SF6=20, Ar=10, RF Power=100W, ICP=30W, pressure=15, time=2min20s).

8. Wet etch sample in BHF solution (3%) at room temperature. 5-6 minutes are necessary for a freely suspended structure. Terminate in H_2O, transfer through several ethanol baths and keep sample submerged.

9. Dry sample in CPD. 25 cycles, slowest gas exchange rate. 40°C.

A.5 Interferometry Setup

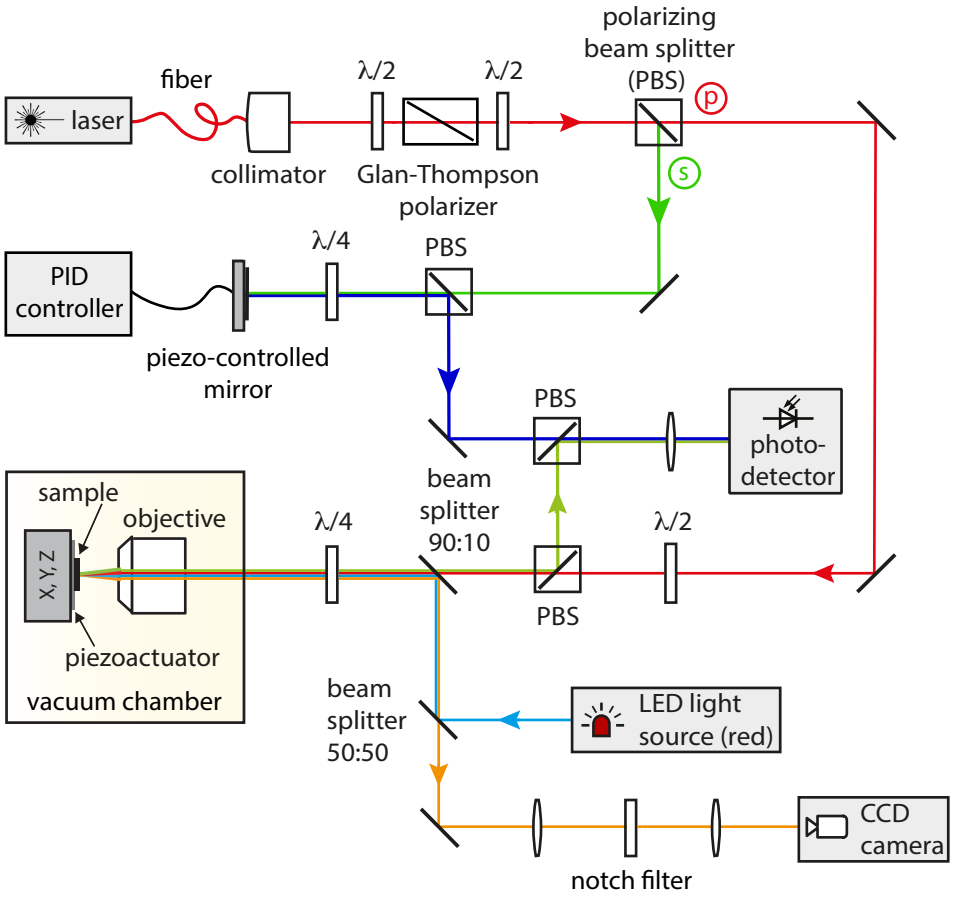

Figure A.2: Illustration of the homodyne, optical interferometry setup used for measuring a nanostring resonator's oscillatory motion.

Figure A.2 shows a complete illustration of the homodyne, optical interferometry setup used for the measurement of nanostring displacement in this thesis. A full description of the setup and the detection principle can be found in Ref. [146].

A.6 Frequency Crowding

Due to the global application of drive signals in the *eigenfrequency tuning technique* (see Sec. 8.3.2), the protocol can be adversely affected by mode-mode cross-talk, i.e the overlap in the drive frequency range of different resonators, also called *frequency crowding* [149]. Cross-Talk can lead to the unintentional tuning of multiple resonators with one drive signal. This problem can be avoided as long as the higher harmonics of the network's resonators are sufficiently separated in frequency. In the following we want to present an example of a three-nanostring network that fulfills these conditions and is thus unaffected by frequency crowding. Note that a similar discussion of this example system can be found in the supplementary material to Ref. [105]. The level scheme of the network is illustrated in Fig. A.3. It consists of three nanostrings

with the fundamental mode frequencies $\Omega_{\mathrm{A}} < \Omega_{\mathrm{B}} < \Omega_{\mathrm{C}}$ and the second harmonic frequencies $\Omega_{\mathrm{C,n=2}} < \Omega_{\mathrm{A,n=2}} < \Omega_{\mathrm{B,n=2}}$.

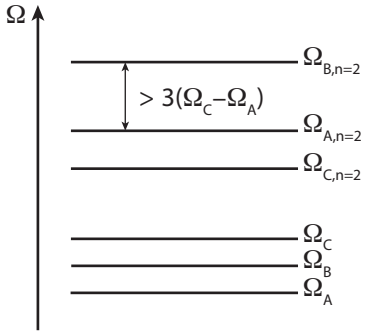

Figure A.3: Exemplary level scheme of an ideally designed three-nanostring network, highlighting the importance of sufficient spacing of the higher harmonics to avoid unintended tuning effects. The figure is redrawn based on Ref. [105].

In order to perform excitation transfer between resonators A and C, their fundamental modes have to be tuned on resonance. Recalling Sec. 8.3.2 and in particular Eq. 8.47, it becomes clear that an auxiliary drive would have to be swept from $\Omega_{\mathrm{A,n=2}}$ to $\Omega_{\mathrm{A,n=2}} + 3(\Omega_{\mathrm{A}} - \Omega_{\mathrm{C}})$ in order to increase Ω_{A} up to the level of Ω_{C}. Therefore, any higher order mode above $\Omega_{\mathrm{A,n=2}}$ (in this case $\Omega_{\mathrm{B,n=2}}$) has to adhere to $\Omega_{\mathrm{B,n=2}} - \Omega_{\mathrm{A,n=2}} > 3(\Omega_{\mathrm{A}} - \Omega_{\mathrm{C}})$, otherwise Ω_{B} will be tuned by the same drive signal. With these conditions fulfilled, Ω_{A} can be tuned in resonance with Ω_{B} as well as Ω_{C}. Due to correct ordering of frequencies, Ω_{B} is also freely tunable towards Ω_{C}, allowing for every possible interaction in the network. Note that, even though these requirements can be considered at the design stage, the fabrication process leads to a degree of variance in the resonance frequencies and post-selection of fabricated resonator networks is required.

A.7 Additional Inter-Resonator Coupling Data

In this section, we present additional data that was used to extract the inter-resonator coupling rates from the mode-splitting of hybridized modes in coupled resonator systems. The corresponding measurements, along with a description of the fitting process can be found in Sec. 11.2.2, while the theory of avoided crossings is discussed in Sec. 8.1.2.

A.7.1 Tri (Series A) Network

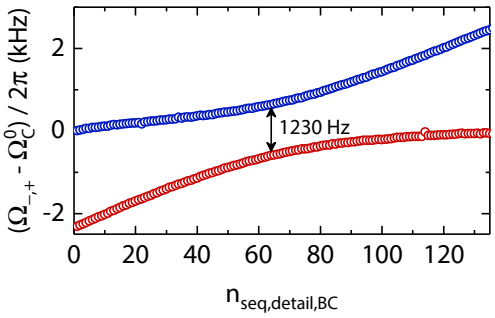

Figure A.4: Fitted resonance frequencies of the lower (red) and upper (blue) branch of the first avoided crossing shown in Fig. 11.6 at $n_{seq} \approx 31$, involving resonators B and C. The data is extracted from the individual spectra as described in Sec. 11.2.2. The minimal mode-splitting is found at $n_{seq,detail,BC} = 64$ to be $g_{AC}/2\pi = 1230\,\text{Hz}$.

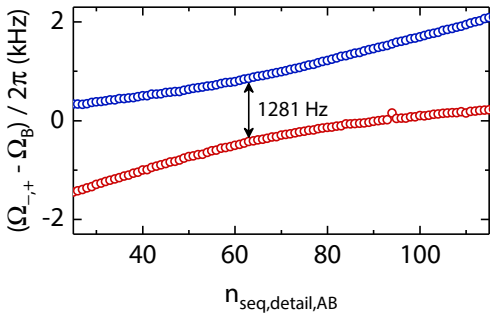

Figure A.5: Fitted resonance frequencies of the lower (red) and upper (blue) branch of the third avoided crossing shown in Fig. 11.6 at $n_{seq} \approx 58$, involving resonators A and B. The data is extracted from the individual spectra as described in Sec. 11.2.2. The minimal mode-splitting is found at $n_{seq,detail,AB} = 63$ to be $g_{AC}/2\pi = 1281\,\text{Hz}$.

A.7.2 Inline Network

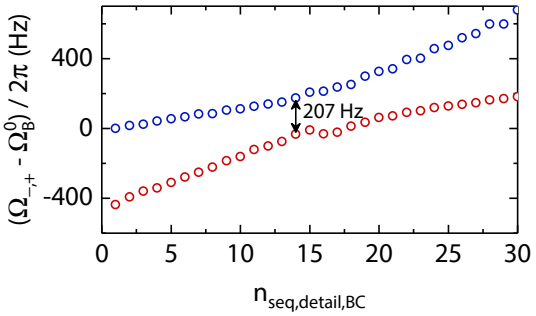

Figure A.6: Fitted resonance frequencies of the lower (red) and upper (blue) branch of the third avoided crossing shown in Fig. 11.8 at $n_{seq} \approx 58$, involving resonators B and C. The data is extracted from the individual spectra as described in Sec. 11.2.2. The minimal mode-splitting is found at $n_{seq,detail,BC} = 14$ to be $g_{AC}/2\pi = 207\,\text{Hz}$.

A.8 Drive-Dependent Hybridized Modes

Here, we will briefly demonstrate how the hybridized eigenfrequencies of a coupled three-nanostring network can be calculated in dependence to an applied auxiliary drive signal.

We recall Eq. 8.15:

$$-\Omega^2\mathbf{M}\vec{\mathbf{x}}_0 = \mathbf{K}\vec{\mathbf{x}}_0, \tag{A.10}$$

with the stiffness and mass matrices $\mathbf{K}$ and $\mathbf{M}$ as in Eq. 8.14. As we are considering a three-nanostring network, $\mathbf{K}$ and $\mathbf{M}$ are 3x3 matrices. We invert the positive definite matrix $\mathbf{M}$ and write the eigenvalue equation as

$$\Omega^2\vec{\mathbf{x}}_0 = \begin{pmatrix} \tilde{\Omega}_\mathrm{A}^2 & -k_\mathrm{AB}/m_\mathrm{A} & -k_\mathrm{AC}/m_\mathrm{A} \\ -k_\mathrm{AB}/m_\mathrm{B} & \tilde{\Omega}_\mathrm{B}^2 & -k_\mathrm{BC}/m_\mathrm{B} \\ -k_\mathrm{AC}/m_\mathrm{C} & -k_\mathrm{BC}/m_\mathrm{C} & \tilde{\Omega}_\mathrm{C}^2 \end{pmatrix} \vec{\mathbf{x}}_0 \tag{A.11}$$

using the undisturbed resonance frequencies $\tilde{\Omega}_i = \sqrt{k_{ii}/m_i}$ and masses m_i of the resonators $i \in$ (A,B,C). Using the experimentally determined stiffness matrix (e.g. Eq. 11.1), this generalized eigenvalue problem can already be numerically solved.
However, we now need to consider the effect of an eigenfrequency tuning sequence (see Sec. 8.3.2) with an auxiliary drive signal $\Omega_\mathrm{A}^\mathrm{aux}$. Without loss of generality we assume the eigenfrequency of resonator A to be tuned, its eigenfrequency $\tilde{\Omega}_\mathrm{A}$ is thus altered from its initial value $\tilde{\Omega}_\mathrm{A}^0$ according to Eq. 8.47. In particular

$$\tilde{\Omega}_\mathrm{A}(\Omega_\mathrm{A}^\mathrm{aux}) = \tilde{\Omega}_\mathrm{A}^0 + \frac{2}{3}\frac{\Omega_\mathrm{A}^\mathrm{aux} - \Omega_\mathrm{A,n=2}}{\Omega_\mathrm{A,n=2}}\tilde{\Omega}_\mathrm{A}^0, \tag{A.12}$$

assuming that the tuning sequence is performed with the second harmonic mode $\Omega_\mathrm{A,n=2}$.
Finally, Eq. A.11 can be solved numerically (e.g. via the **Eigenvalues** method in Mathematica) for arbitrary drive signals $\Omega_\mathrm{A}^\mathrm{aux}$. The eigenvalues of the equation are the squares of the three hybridized mode frequencies, i.e. $\Omega_\mathrm{A,B,C}^2$.

Note that additional tuning sequences can be incorporated analogously, e.g. by including a second variable frequency $\tilde{\Omega}_\mathrm{B}(\Omega_\mathrm{B}^\mathrm{aux})$. Furthermore, the calculation can be easily extended towards any number of coupled resonators.

A.9 Numerically Calculated Mode Displacement

Here, we present the mathematical model and a sketch of the numeric calculation algorithm used to calculate the displacement of any or all nanostrings in a coupled resonator network in response to an arbitrary drive frequency. Model calculations performed in this manner are shown in Fig. 11.9.

We begin with the equations of motion for the three coupled resonators shown in Eqs. 8.24-8.26:

$$\begin{aligned} m_\mathrm{A}\ddot{x}_\mathrm{A} + m_\mathrm{A}\Gamma_\mathrm{A}\dot{x}_\mathrm{A} + \kappa_\mathrm{AA}x_\mathrm{A} &= \kappa_\mathrm{AB}(x_\mathrm{B} - x_\mathrm{A}) + \kappa_\mathrm{AC}(x_\mathrm{C} - x_\mathrm{A}) + F_\mathrm{drive} \\ m_\mathrm{B}\ddot{x}_\mathrm{B} + m_\mathrm{B}\Gamma_\mathrm{B}\dot{x}_\mathrm{B} + \kappa_\mathrm{BB}x_\mathrm{B} &= \kappa_\mathrm{AB}(x_\mathrm{A} - x_\mathrm{B}) + \kappa_\mathrm{BC}(x_\mathrm{C} - x_\mathrm{B}) + F_\mathrm{drive} \\ m_\mathrm{C}\ddot{x}_\mathrm{C} + m_\mathrm{C}\Gamma_\mathrm{C}\dot{x}_\mathrm{C} + \kappa_\mathrm{CC}x_\mathrm{C} &= \kappa_\mathrm{AC}(x_\mathrm{A} - x_\mathrm{C}) + \kappa_\mathrm{BC}(x_\mathrm{B} - x_\mathrm{C}) + F_\mathrm{drive} \end{aligned} \tag{A.13}$$

We are searching for the response of a specific string (w.l.o.g. nanostring A) to a externally applied driving force $F_\mathrm{drive}(t) = F_0 \exp(i\Omega_\mathrm{p} t)$, where Ω_p can be arbitrarily chosen. As we are dealing with almost identical nanostrings, we will set $\Gamma_\mathrm{A} = \Gamma_\mathrm{B} = \Gamma_\mathrm{C} \equiv \Gamma$ and $m_\mathrm{A} = m_\mathrm{B} = m_\mathrm{C} \equiv m$.

Using an ansatz of the form $x_m(t) = x_0 c_m(t) \exp(i\Omega_\mathrm{p} t)$ (m = A,B,C) we find solutions for the amplitude coefficients $c_m(t)$ with $|c_\mathrm{A}|^2 + |c_\mathrm{B}|^2 + |c_\mathrm{C}|^2 = 1$. As in Sec. 8.2.2, we neglect the second derivatives $\ddot{c}_m(t)$ and obtain

$$\begin{aligned} (2i\Omega_\mathrm{p} + \Gamma)\dot{c}_\mathrm{A} + (\tilde{\Omega}_\mathrm{A}2 - \Omega_\mathrm{p}^2 + i\Omega_\mathrm{p}\Gamma)c_\mathrm{A} &= \frac{\kappa_\mathrm{AB}}{m}c_\mathrm{B} + \frac{\kappa_\mathrm{AC}}{m}c_\mathrm{C} + \frac{F_0}{mx_0} \\ (2i\Omega_\mathrm{p} + \Gamma)\dot{c}_\mathrm{B} + (\tilde{\Omega}_\mathrm{B}2 - \Omega_\mathrm{p}^2 + i\Omega_\mathrm{p}\Gamma)c_\mathrm{B} &= \frac{\kappa_\mathrm{AB}}{m}c_\mathrm{A} + \frac{\kappa_\mathrm{BC}}{m}c_\mathrm{C} + \frac{F_0}{mx_0} \\ (2i\Omega_\mathrm{p} + \Gamma)\dot{c}_\mathrm{C} + (\tilde{\Omega}_\mathrm{C}2 - \Omega_\mathrm{p}^2 + i\Omega_\mathrm{p}\Gamma)c_\mathrm{C} &= \frac{\kappa_\mathrm{AC}}{m}c_\mathrm{A} + \frac{\kappa_\mathrm{BC}}{m}c_\mathrm{B} + \frac{F_0}{mx_0}, \end{aligned} \tag{A.14}$$

where we used the undisturbed resonance frequencies $\tilde{\Omega}_i = \sqrt{k_{ii}/m_i}$ of the resonators $i \in$ (A,B,C). The system of coupled differential equations in Eq. A.14 can now be numerically solved (e.g. by Mathematica's **NDSolve**) for $c_\mathrm{A}(t)$ using the initial values $c_\mathrm{A}(0) = c_\mathrm{B}(0) = c_\mathrm{C}(0) = 0$. Subsequently we can integrate the coefficient over a duration T to obtain a value proportional to the displacement. In particular

$$|x_\mathrm{A}^\mathrm{num}|^2 = \int_0^T |c_\mathrm{A}(t)|^2 dt \propto |x_\mathrm{A}|^2. \tag{A.15}$$

Since the amplitude of the drive force F_0 is independent of time, T should be chosen as short as possible in order save computation time. However, the timescale of the oscillations need to be kept small with respect to the simulation time, i.e. $T \gg 2\pi/\Omega_\mathrm{p}$.

In the case discussed in Sec. 11.2.3, the displacement of a nanostring is evaluated along one of the hybridized modes of the system, i.e. we choose Ω_p as the hybridized eigenfrequency. The hybridized frequencies change over the course of the measurement due to an auxiliary drive Ω^aux and can be calculated as described in App. A.8. We define a pseudo-function $\Omega_i^\mathrm{hyb}(\Omega^\mathrm{aux})$ that retrieves the i-th hybridized mode for a given auxiliary drive.

Finally, we sketch the numeric calculation of the amplitude of nanostring A, $|x_\mathrm{A}^\mathrm{num}|^2$ along the first hybridized mode ($i = 1$) in Fig. A.7 as pseudo-code,
As a result one obtains one value $|x_\mathrm{A}^\mathrm{num}|^2$ for each sweep-point of the measurement, proportional to the displacement $|x_\mathrm{A}|^2$ that the resonator exhibits along the investigated hybridized mode branch.

while $\Omega^{\mathrm{aux}} < \Omega^{\mathrm{aux}}_{\mathrm{max}}$ **do** ▷ tuning sequence
  $\Omega_{\mathrm{p}} \leftarrow \Omega_1^{\mathrm{hyb}}(\Omega^{\mathrm{aux}})$ ▷ calc. hyb. freq. for drive
  $x_{\mathrm{A}}^{\mathrm{num}} \leftarrow$**NDSolve[EOMs]** ▷ Solve eqs. of motion
  return $|x_{\mathrm{A}}^{\mathrm{num}}|^2$ ▷ solution at curr. drive
  $\Omega^{\mathrm{aux}} \leftarrow (\Omega^{\mathrm{aux}} + \Delta\Omega^{\mathrm{aux}})$ ▷ tuning step
end while

Figure A.7: Pseudo-code for the numerical calculation of the displacement amplitude $|x_{\mathrm{A}}^{\mathrm{num}}|^2$ for an arbitrary tuning sequence with a drive frequency ranging from Ω^{aux} to $\Omega^{\mathrm{aux}}_{\mathrm{max}}$. Note that the **NDSolve** command refers to a numerical solution of the system of equations shown in A.14, as described in the text. Further, the **return** command signifies only the output or storage of the calculated value, not a termination of the program.

A.10 Landau-Zener Transitions

Here we will provide a sketch of the numerical calculation algorithm to model Landau-Zener transitions in multi-nanostring networks. The theory of Landau-Zener transitions is described in Sec. 8.2.1 and the measurement protocol is presented in Sec. 11.3.1.

The model calculation is based on the solution of the differential equations 8.31-8.33, which we derived in Sec. 8.2.2. We recall that the Landau-Zener protocol is driven by an auxiliary drive that leads to a time dependent resonator frequency $\Omega_{\mathrm{A}}(t)$, which develops according to Eq. 8.27 with a ramp rate of $\zeta = \Delta\Omega_{\mathrm{A}} + \tau$. The duration of each Landau-Zener sequence, i.e. the window of data acquisition is $t = 0 \ldots t_{\mathrm{end}}$. Accordingly, Δt is the time interval at which the model is evaluated. Sequences are then repeated for varying ramp rates from τ_{start} to τ_{end} with $\Delta\tau$ being the step-size between investigated ramp rates. The goal is the calculation of the amplitude coefficients $|c_{\mathrm{A,B,C}}(t)|^2 \propto |x_{\mathrm{A,B,C}}(t)|^2$, which are proportional to the observable displacement. Lastly we define $\Omega_{\mathrm{A}}^{\tau}(t)$ as the current frequency of resonator A, evaluated according to Eq. 8.27 at t for a ramp rate τ.

Note that for the solution of the differential equations The differential equations can be solved numerically by e.g. the **NDSolve** method of Mathematica, which we will use in the following. In particular, we solve Eqs. 8.31-8.33 for $c_{\mathrm{A,B,C}}(t)$ using the initial values $c_{\mathrm{A}}(0) = c_{\mathrm{B}}(0) = c_{\mathrm{C}}(0) = 0$ and performing the calculation up to $t = t_{\mathrm{end}}$. Having defined all necessary expressions, we present the algorithm for the calculation as pseudo-code in Fig. A.8.

The resulting model calculations are shown in Sec. 11.3 and provide good agreement with experimental results.

$\tau \leftarrow \tau_{\text{start}}$
while $\tau < \tau_{\text{end}}$ **do** ▷ sweep ramp rate
  $t \leftarrow 0$
  $c^{\tau}_{\text{A,B,C}} \leftarrow$ **NDSolve**[EOMs] ▷ Solve eqs. of motion
  while $t < t_{\text{end}}$ **do** ▷ sweep meas. time
    $\Omega_{\text{A}} = \Omega^{\tau}_{\text{A}}(t)$
    return $|c_{\text{A,B,C}}(t)|^2$ ▷ solution at curr. time and rate
    $t \leftarrow (t + \Delta t)$ ▷ next time-step
  end while
  $\tau \leftarrow (\tau + \Delta\tau)$ ▷ next sequence
end while

Figure A.8: Pseudo-code for the numerical calculation of the amplitude coefficients $|c_{\text{A,B,C}}|^2$ for a Landau-Zener transition sequence with duration $t = 0 \dots t_{\text{end}}$, evaluated for ramp rates from τ_{start} to τ_{end}. Note that the **NDSolve** command refers to a numerical solution of the system Eqs. 8.31-8.33, as described in the text. Further, the **return** command signifies only the output or storage of the calculated value, not a termination of the program.

A.11 Additional Images

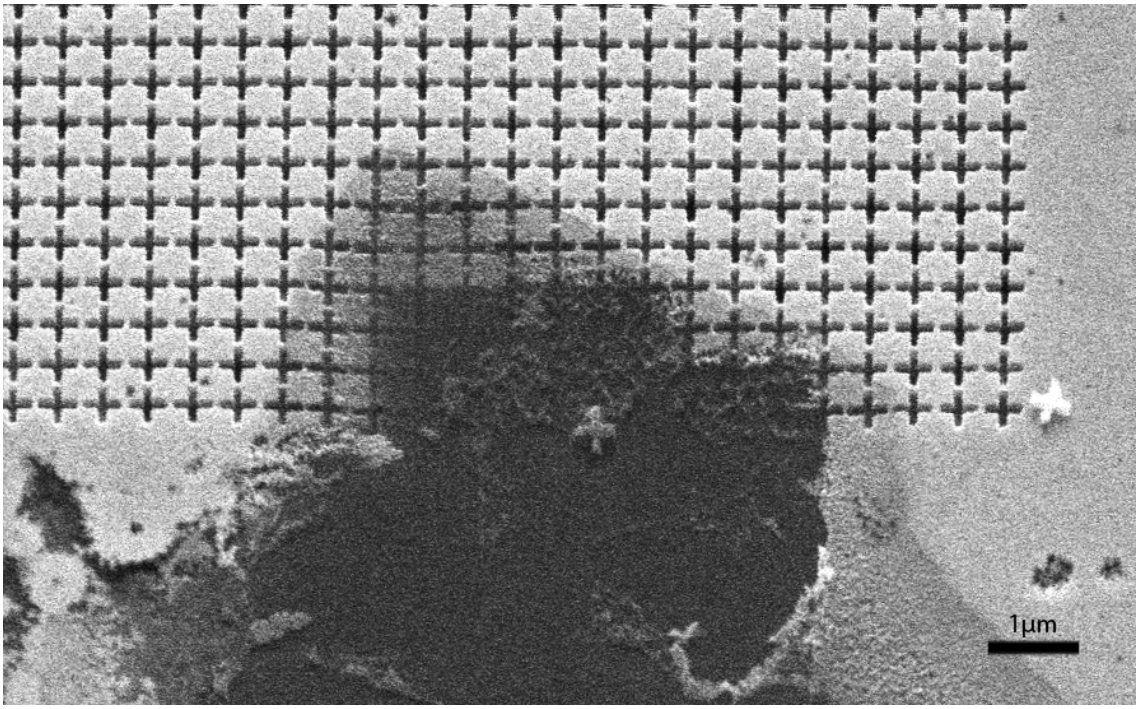

Figure A.9: Angled (55°) Scanning Electron Microscopy (SEM) image of a Si_3N_4/Co double-layer phononic shield structure after wet etching in buffered hydrofluoric acid (BHF). The image shows a different shield structure on the same chip as the ones shown in Fig. 4.5. Due to unknown reasons the structure was damaged. Parts of it consequently collapsed, indicating that it was fully released from the substrate.

Bibliography

[1] M. Gad-el Hak, *The MEMS handbook* (CRC Press, 2002).

[2] J. B. Angell, S. C. Terry, and P. W. Barth, "Silicon Micromechanical Devices," Sci. Am. **248**, 44–55 (1983).

[3] M. Perlmutter and L. Robin, "High-performance, low cost inertial MEMS: A market in motion!" in *Proc. 2012 IEEE/ION Position, Locat. Navig. Symp.* (IEEE, 2012) pp. 225–229.

[4] R. Bogue, "Recent developments in MEMS sensors: A review of applications, markets and technologies," Sens. Rev. **33**, 300–304 (2013).

[5] D. Eddy and D. Sparks, "Application of MEMS technology in automotive sensors and actuators," Proc. IEEE **86**, 1747–1755 (1998).

[6] J. Marek, "MEMS for automotive and consumer electronics," in *2010 IEEE Int. Solid-State Circuits Conf. -* (IEEE, 2010) pp. 9–17.

[7] J. Gubbi, R. Buyya, S. Marusic, and M. Palaniswami, "Internet of Things (IoT): A vision, architectural elements, and future directions," Futur. Gener. Comput. Syst. **29**, 1645–1660 (2013).

[8] D. Rugar and P. Hansma, "Atomic Force Microscopy," Phys. Today **43**, 23–30 (1990).

[9] S. N. Magonov and M.-H. Whangbo, *Surface analysis with STM and AFM : experimental and theoretical aspects of image analysis* (VCH, Weinheim, 1996) p. 323.

[10] E. M. Puchner and H. E. Gaub, "Force and function: probing proteins with AFM-based force spectroscopy." Curr. Opin. Struct. Biol. **19**, 605–14 (2009).

[11] S. Hong, M. S. Grinolds, P. Maletinsky, R. L. Walsworth, M. D. Lukin, and A. Yacoby, "Coherent, Mechanical Control of a Single Electronic Spin," Nano Lett. **12**, 3920–3924 (2012).

[12] Y. T. Yang, C. Callegari, X. L. Feng, K. L. Ekinci, and M. L. Roukes, "Zeptogram-Scale Nanomechanical Mass Sensing," Nano Lett. **6**, 583–586 (2006).

[13] B. Lassagne, D. Garcia-Sanchez, A. Aguasca, and A. Bachtold, "Ultrasensitive Mass Sensing with a Nanotube Electromechanical Resonator," Nano Lett. **8**, 3735–3738 (2008).

[14] J. Chaste, A. Eichler, J. Moser, G. Ceballos, R. Rurali, and A. Bachtold, "A nanomechanical mass sensor with yoctogram resolution," Nat. Nanotechnol. **7**, 301–304 (2012).

[15] K. Eom, H. S. Park, D. S. Yoon, and T. Kwon, "Nanomechanical resonators and their applications in biological/chemical detection: Nanomechanics principles," Phys. Rep. **503**, 115–163 (2011).

[16] B. Arash, J.-W. Jiang, and T. Rabczuk, "A review on nanomechanical resonators and their applications in sensors and molecular transportation," Appl. Phys. Rev. **2**, 021301 (2015).

[17] M. Aspelmeyer, T. J. Kippenberg, and F. Marquardt, "Cavity optomechanics," Rev. Mod. Phys. **86**, 1391–1452 (2014).

[18] V. B. Braginsky and F. Y. Khalili, *Quantum measurement*, edited by K. S. Thorne (Cambridge University Press, 1995) p. 191.

[19] B. P. and others Abbott, "Observation of Gravitational Waves from a Binary Black Hole Merger," Phys. Rev. Lett. **116**, 061102 (2016).

[20] J. T. Hill, A. H. Safavi-Naeini, J. Chan, and O. Painter, "Coherent optical wavelength conversion via cavity optomechanics," Nat. Commun. **3**, 1196 (2012).

[21] J. Chan, T. P. M. Alegre, A. H. Safavi-Naeini, J. T. Hill, A. Krause, S. Gröblacher, M. Aspelmeyer, and O. Painter, "Laser cooling of a nanomechanical oscillator into its quantum ground state," Nature **478**, 89–92 (2011).

[22] C. A. Regal, J. D. Teufel, and K. W. Lehnert, "Measuring nanomechanical motion with a microwave cavity interferometer," Nat. Phys. **4**, 555–560 (2008).

[23] J. D. Teufel, D. Li, M. S. Allman, K. Cicak, A. J. Sirois, J. D. Whittaker, and R. W. Simmonds, "Circuit cavity electromechanics in the strong-coupling regime," Nature **471**, 204–208 (2011).

[24] M. D. LaHaye, J. Suh, P. M. Echternach, K. C. Schwab, and M. L. Roukes, "Nanomechanical measurements of a superconducting qubit," Nature **459**, 960–964 (2009).

[25] J.-M. Pirkkalainen, S. U. Cho, J. Li, G. S. Paraoanu, P. J. Hakonen, and M. A. Sillanpää, "Hybrid circuit cavity quantum electrodynamics with a micromechanical resonator," Nature **494**, 211–215 (2013).

[26] J. M. Pirkkalainen, E. Damskägg, M. Brandt, F. Massel, and M. A. Sillanpää, "Squeezing of Quantum Noise of Motion in a Micromechanical Resonator," Phys. Rev. Lett. **115**, 1–5 (2015).

[27] E. E. Wollman, C. U. Lei, A. J. Weinstein, J. Suh, A. Kronwald, F. Marquardt, A. A. Clerk, and K. C. Schwab, "Quantum squeezing of motion in a mechanical resonator." Science **349**, 952–5 (2015).

[28] T. A. Palomaki, J. D. Teufel, R. W. Simmonds, and K. W. Lehnert, "Entangling mechanical motion with microwave fields," Science **342**, 710–713 (2013).

[29] C. F. Ockeloen-Korppi, E. Damskägg, J.-M. Pirkkalainen, M. Asjad, A. A. Clerk, F. Massel, M. J. Woolley, and M. A. Sillanpää, "Stabilized entanglement of massive mechanical oscillators," Nature **556**, 478–482 (2018).

[30] B. Lenk, H. Ulrichs, F. Garbs, and M. Münzenberg, "The building blocks of magnonics," Phys. Rep. **507**, 107–136 (2011).

[31] H. Huebl, C. W. Zollitsch, J. Lotze, F. Hocke, M. Greifenstein, A. Marx, R. Gross, and S. T. Goennenwein, "High cooperativity in coupled microwave resonator ferrimagnetic insulator hybrids," Phys. Rev. Lett. **111**, 1–5 (2013).

[32] X. Zhang, C. L. Zou, L. Jiang, and H. X. Tang, "Strongly coupled magnons and cavity microwave photons," Phys. Rev. Lett. **113**, 1–5 (2014).

[33] Y. Tabuchi, S. Ishino, T. Ishikawa, R. Yamazaki, K. Usami, and Y. Nakamura, "Hybridizing ferromagnetic magnons and microwave photons in the quantum limit," Phys. Rev. Lett. **113**, 1–5 (2014).

[34] A. Osada, R. Hisatomi, A. Noguchi, Y. Tabuchi, R. Yamazaki, K. Usami, M. Sadgrove, R. Yalla, M. Nomura, and Y. Nakamura, "Cavity Optomagnonics with Spin-Orbit Coupled Photons," Phys. Rev. Lett. **116**, 1–5 (2016).

[35] X. Zhang, N. Zhu, C. L. Zou, and H. X. Tang, "Optomagnonic Whispering Gallery Microresonators," Phys. Rev. Lett. **117**, 1–5 (2016).

[36] R. Hisatomi, A. Osada, Y. Tabuchi, T. Ishikawa, A. Noguchi, R. Yamazaki, K. Usami, and Y. Nakamura, "Bidirectional conversion between microwave and light via ferromagnetic magnons," Phys. Rev. B **93**, 1–13 (2016).

[37] X. Zhang, C.-L. Zou, L. Jiang, and H. X. Tang, "Cavity magnomechanics," Sci. Adv. **2**, e1501286–e1501286 (2016).

[38] M. Eichenfield, J. Chan, R. M. Camacho, K. J. Vahala, and O. Painter, "Optomechanical crystals," Nature **462**, 78–82 (2009).

[39] S. Chikazumi, C. D. C. D. Graham, and S. Chikazumi, *Physics of ferromagnetism* (Oxford University Press, Oxford, 1997) p. 655.

[40] N. A. Spaldin and M. Fiebig, "The Renaissance of Magnetoelectric Multiferroics," Science **309**, 391–392 (2005).

[41] Z. Liu, X. Zhang, Y. Mao, Y. Y. Zhu, Z. Yang, C. T. Chan, and P. Sheng, "Locally Resonant Sonic Materials," Science **289**, 1734–1736 (2000).

[42] R. H. Olsson III and I. El-Kady, "Microfabricated phononic crystal devices and applications," Meas. Sci. Technol. **20**, 012002 (2009).

[43] J. Chan, M. Eichenfield, R. Camacho, and O. Painter, "Optical and mechanical design of a "zipper" photonic crystal optomechanical cavity," Opt. Express **17**, 3802 (2009).

[44] K. E. Grutter, M. Davanco, and K. Srinivasan, "Si3N4 nanobeam optomechanical crystals," IEEE J. Sel. Top. Quantum Electron. **21**, 61–71 (2015).

[45] O. Yalcin, *Ferromagnetic Resonance - Theory and Applications* (InTech, London, 2013).

[46] H. F. Tiersten, "Coupled Magnetomechanical Equations for Magnetically Saturated Insulators," J. Math. Phys. **5**, 1298–1318 (1964).

[47] T. Kobayashi, R. C. Barker, J. L. Bleustein, and A. Yelon, "Ferromagnetoelastic resonance in thin films. I. Formal treatment," Phys. Rev. B **7**, 3273–3285 (1973).

[48] R. Gross and A. Marx, *Festkörperphysik*, De Gruyter Studium (De Gruyter, Oldenbourg, 2018).

[49] J. D. Joannopoulos, S. G. Johnson, J. N. Winn, and R. D. Meade, *Photonic crystals : molding the flow of light* (Princeton University Press, 1995) p. 137.

[50] S. G. Johnson and J. D. Joannopoulos, *Photonic crystals : the road from theory to practice* (Kluwer Academic Publishers, 2002) p. 156.

[51] B. Liang, X. S. Guo, J. Tu, D. Zhang, and J. C. Cheng, "An acoustic rectifier," Nat. Mater. **9**, 989–992 (2010).

[52] S. Yang, J. H. Page, Z. Liu, M. L. Cowan, C. T. Chan, and P. Sheng, "Focusing of sound in a 3D phononic crystal," Phys. Rev. Lett. **93**, 024301–1 (2004).

[53] G. Jia and Z. Shi, "A new seismic isolation system and its feasibility study," Earthq. Eng. Eng. Vib. **9**, 75–82 (2010).

[54] C. Kittel, *Introduction to solid state physics* (Wiley, New York, 2005) p. 680.

[55] B. A. Auld, *Acoustic fields and waves in solids*, A Wiley-Interscience publication (Wiley, New York, 1973).

[56] Y. Tanaka, Y. Tomoyasu, and S.-i. Tamura, "Band structure of acoustic waves in phononic lattices: Two-dimensional composites with large acoustic mismatch," Phys. Rev. B **62**, 7387–7392 (2000).

[57] R. E. Camley, B. Djafari-Rouhani, L. Dobrzynski, and A. A. Maradudin, "Transverse elastic waves in periodically layered infinite and semi-infinite media," Phys. Rev. B **27**, 7318–7329 (1983).

[58] M. S. Kushwaha, P. Halevi, L. Dobrzynski, and B. Djafari-Rouhani, "Acoustic band structure of periodic elastic composites," Phys. Rev. Lett. **71**, 2022–2025 (1993).

[59] Z.-G. Huang, *Acoust. Waves - From Microdevices to Helioseismology*, edited by M. G. Beghi (InTech, London, 2011) Chap. 1, pp. 4–20.

[60] A. H. Safavi-Naeini and O. Painter, "Design of Optomechanical Cavities and Waveguides on a Simultaneous Bandgap Phononic-Photonic Crystal Slab," Opt. Express **18**, 14926 (2010).

[61] T. Gorishnyy, C. K. Ullal, M. Maldovan, G. Fytas, and E. L. Thomas, "Hypersonic Phononic Crystals," Phys. Rev. Lett. **94**, 115501 (2005).

[62] S. Benchabane, A. Khelif, J.-Y. Rauch, L. Robert, and V. Laude, "Evidence for complete surface wave band gap in a piezoelectric phononic crystal," Phys. Rev. E **73**, 065601 (2006).

[63] T. P. M. Alegre, A. Safavi-Naeini, M. Winger, and O. Painter, "Quasi-two-dimensional optomechanical crystals with a complete phononic bandgap," Opt. Express **19**, 5658 (2011).

[64] J. Chan, A. H. Safavi-Naeini, J. T. Hill, S. Meenehan, and O. Painter, "Optimized optomechanical crystal cavity with acoustic radiation shield," Appl. Phys. Lett. **101**, 081115 (2012).

[65] A. W. Rushforth, E. De Ranieri, J. Zemen, J. Wunderlich, K. W. Edmonds, C. S. King, E. Ahmad, R. P. Campion, C. T. Foxon, B. L. Gallagher, K. Výborný, J. Kučera, and T. Jungwirth, "Voltage control of magnetocrystalline anisotropy in ferromagnetic-semiconductor-piezoelectric hybrid structures," Phys. Rev. B **78**, 085314 (2008).

[66] M. Weiler, A. Brandlmaier, S. Geprägs, M. Althammer, M. Opel, C. Bihler, H. Huebl, M. S. Brandt, R. Gross, and S. T. B. Goennenwein, "Voltage controlled inversion of magnetic anisotropy in a ferromagnetic thin film at room temperature," New J. Phys. **11**, 013021 (2009).

[67] M. Löhndorf, T. Duenas, M. Tewes, E. Quandt, M. Rührig, and J. Wecker, "Highly sensitive strain sensors based on magnetic tunneling junctions," Appl. Phys. Lett. **81**, 313–315 (2002).

[68] M. Weiler, L. Dreher, C. Heeg, H. Huebl, R. Gross, M. S. Brandt, and S. T. B. Goennenwein, "Elastically Driven Ferromagnetic Resonance in Nickel Thin Films," Phys. Rev. Lett. **106**, 117601 (2011).

[69] K. Uchida, H. Adachi, T. An, T. Ota, M. Toda, B. Hillebrands, S. Maekawa, and E. Saitoh, "Long-range spin Seebeck effect and acoustic spin pumping," Nat. Mater. **10**, 737–741 (2011).

[70] M. Weiler, H. Huebl, F. S. Goerg, F. D. Czeschka, R. Gross, and S. T. B. Goennenwein, "Spin Pumping with Coherent Elastic Waves," Phys. Rev. Lett. **108**, 176601 (2012).

[71] S. C. Masmanidis, H. X. Tang, E. B. Myers, M. Li, K. De Greve, G. Vermeulen, W. Van Roy, and M. L. Roukes, "Nanomechanical Measurement of Magnetostriction and Magnetic Anisotropy in (Ga,Mn)As," Phys. Rev. Lett. **95**, 187206 (2005).

[72] M. Pernpeintner, R. B. Holländer, M. J. Seitner, E. M. Weig, R. Gross, S. T. B. Goennenwein, and H. Huebl, "A versatile platform for magnetostriction measurements in thin films," J. Appl. Phys. **119**, 093901 (2016).

[73] J. Fidler and T. Schrefl, "Micromagnetic modelling - the current state of the art," J. Phys. D. Appl. Phys. **33**, R135–R156 (2000).

[74] L. Landau and E. M. Lifshitz, "On the Theory of the Dispersion of Magnetic Permeability in Ferromagnetic Bodies," Phys. Z. Sowjet. **8**, 153–169 (1935).

[75] T. Gilbert, "A Phenomenological Theory of Damping in Ferromagnetic Materials," IEEE Trans. Magn. **40**, 3443–3449 (2004).

[76] M. Weiler, *Magnon-Phonon interactions in ferromagnetic thin films*, Ph.D. thesis, Walther-Meißner-Institut and Technische Universität München (2012).

[77] C. Kittel, "On the theory of ferromagnetic resonance absorption," Phys. Rev. **73**, 155–161 (1948).

[78] D. Polder, "On the theory of ferromagnetic resonance," London, Edinburgh, Dublin Philos. Mag. J. Sci. **40**, 99–115 (1949).

[79] A. G. A. G. Gurevich and G. A. G. A. Melkov, *Magnetization oscillations and waves* (CRC Press, 1996) p. 445.

[80] *COMSOL Multiphysics® v. 5.3.* (COMSOL AB, Stockholm, Sweden, 2017).

[81] M. Eichenfield, J. Chan, A. H. Safavi-Naeini, K. J. Vahala, and O. Painter, "Modeling dispersive coupling and losses of localized optical and mechanical modes in optomechanical crystals," Opt. Express **17**, 20078 (2009).

[82] P. B. Deotare, M. W. McCutcheon, I. W. Frank, M. Khan, and M. Lončar, "High quality factor photonic crystal nanobeam cavities," Appl. Phys. Lett. **94**, 121106 (2009).

[83] J. Chan, *Laser cooling of an optomechanical crystal resonator to its quantum ground state of motion*, Ph.D. thesis, California Institute of Technology (2012).

[84] M. A. Mohammad, M. Muhammad, S. K. Dew, and M. Stepanova, "Fundamentals of Electron Beam Exposure and Development," in *Nanofabrication* (Springer Vienna, Vienna, 2012) Chap. 2, pp. 11–41.

[85] L. Liensberger, "Spin-Orbit Torques and Magnetization Dynamics in Non-collinear Magnets," Masters Thesis (2017).

[86] V. P. Denysenkov and A. M. Grishin, "Broadband ferromagnetic resonance spectrometer," Rev. Sci. Instrum. **74**, 3400–3405 (2003).

[87] S. S. Kalarickal, P. Krivosik, M. Wu, C. E. Patton, M. L. Schneider, P. Kabos, T. J. Silva, and J. P. Nibarger, "Ferromagnetic resonance linewidth in metallic thin films: Comparison of measurement methods," J. Appl. Phys. **99**, 093909 (2006).

[88] H. Maier-Flaig, S. T. Goennenwein, R. Ohshima, M. Shiraishi, R. Gross, H. Huebl, and M. Weiler, "Note: Derivative divide, a method for the analysis of broadband ferromagnetic resonance in the frequency domain," Rev. Sci. Instrum. **89**, 1–3 (2018).

[89] J. M. Shaw, H. T. Nembach, T. J. Silva, and C. T. Boone, "Precise determination of the spectroscopic g-factor by use of broadband ferromagnetic resonance spectroscopy," J. Appl. Phys. **114**, 243906 (2013).

[90] I. S. Maksymov and M. Kostylev, "Broadband stripline ferromagnetic resonance spectroscopy of ferromagnetic films, multilayers and nanostructures," Phys. E Low-dimensional Syst. Nanostructures **69**, 253–293 (2015).

[91] S. Klingler, V. Amin, S. Geprägs, K. Ganzhorn, H. Maier-Flaig, M. Althammer, H. Huebl, R. Gross, R. D. McMichael, M. D. Stiles, S. T. Goennenwein, and M. Weiler, "Spin-Torque Excitation of Perpendicular Standing Spin Waves in Coupled YIG/Co Heterostructures," Phys. Rev. Lett. **120**, 127201 (2018).

[92] M. A. W. Schoen, D. Thonig, M. L. Schneider, T. J. Silva, H. T. Nembach, O. Eriksson, O. Karis, and J. M. Shaw, "Ultra-low magnetic damping of a metallic ferromagnet," Nat. Phys. **12**, 839–842 (2016).

[93] C. Kittel, "On the Gyromagnetic Ratio and Spectroscopic Splitting Factor of Ferromagnetic Substances," Phys. Rev. **76**, 743–748 (1949).

[94] H. T. Nembach, J. M. Shaw, C. T. Boone, and T. J. Silva, "Mode- and Size-Dependent Landau-Lifshitz Damping in Magnetic Nanostructures: Evidence for Nonlocal Damping," Phys. Rev. Lett. **110**, 117201 (2013).

[95] A. Vansteenkiste, J. Leliaert, M. Dvornik, M. Helsen, F. Garcia-Sanchez, and B. Van Waeyenberge, "The design and verification of MuMax3," AIP Adv. **4**, 107133 (2014).

[96] T. Sebastian, K. Schultheiss, B. Obry, B. Hillebrands, and H. Schultheiss, "Micro-focused Brillouin light scattering: imaging spin waves at the nanoscale," Front. Phys. **3**, 35 (2015).

[97] G. P. Zhang, W. Hübner, G. Lefkidis, Y. Bai, and T. F. George, "Paradigm of the time-resolved magneto-optical Kerr effect for femtosecond magnetism," Nat. Phys. **5**, 499–502 (2009).

[98] D. Dragoman and M. Dragoman, *Quantum-Classical Analogies* (Springer Berlin Heidelberg, 2004) p. 347.

[99] L. Novotny, "Strong coupling, energy splitting, and level crossings: A classical perspective," Am. J. Phys. **78**, 1199–1202 (2010).

[100] K. Gajo, S. Schüz, and E. M. Weig, "Strong 4-mode coupling of nanomechanical string resonators," Appl. Phys. Lett. **111**, 133109 (2017).

[101] H. Okamoto, A. Gourgout, C. Y. Chang, K. Onomitsu, I. Mahboob, E. Y. Chang, and H. Yamaguchi, "Coherent phonon manipulation in coupled mechanical resonators," Nat. Phys. **9**, 480–484 (2013).

[102] T. Faust, J. Rieger, M. J. Seitner, J. P. Kotthaus, and E. M. Weig, "Coherent control of a classical nanomechanical two-level system," Nat. Phys. **9**, 485–488 (2013).

[103] T. Faust, J. Rieger, M. J. Seitner, P. Krenn, J. P. Kotthaus, and E. M. Weig, "Nonadiabatic Dynamics of Two Strongly Coupled Nanomechanical Resonator Modes," Phys. Rev. Lett. **109**, 037205 (2012).

[104] M. J. Seitner, H. Ribeiro, J. Kölbl, T. Faust, J. P. Kotthaus, and E. M. Weig, "Classical Stückelberg interferometry of a nanomechanical two-mode system," Phys. Rev. B **94**, 245406 (2016).

[105] M. Pernpeintner, P. Schmidt, D. Schwienbacher, R. Gross, and H. Huebl, "Frequency Control and Coherent Excitation Transfer in a Nanostring-resonator Network," Phys. Rev. Appl. **10**, 34007 (2018).

[106] H. Okamoto, R. Schilling, H. Schütz, V. Sudhir, D. J. Wilson, H. Yamaguchi, and T. J. Kippenberg, "A strongly coupled Λ-type micromechanical system," Appl. Phys. Lett. **108**, 153105 (2016).

[107] D. Hatanaka, I. Mahboob, K. Onomitsu, and H. Yamaguchi, "A phonon transistor in an electromechanical resonator array," Appl. Phys. Lett. **102**, 213102 (2013).

[108] S. Rips and M. J. Hartmann, "Quantum Information Processing with Nanomechanical Qubits," Phys. Rev. Lett. **110**, 120503 (2013).

[109] I. Mahboob, M. Mounaix, K. Nishiguchi, A. Fujiwara, and H. Yamaguchi, "A multimode electromechanical parametric resonator array," Sci. Rep. **4**, 4448 (2015).

[110] A. D. O'Connell, M. Hofheinz, M. Ansmann, R. C. Bialczak, M. Lenander, E. Lucero, M. Neeley, D. Sank, H. Wang, M. Weides, J. Wenner, J. M. Martinis, and A. N. Cleland, "Quantum ground state and single-phonon control of a mechanical resonator," Nature **464**, 697–703 (2010).

[111] T. A. Palomaki, J. W. Harlow, J. D. Teufel, R. W. Simmonds, and K. W. Lehnert, "Coherent state transfer between itinerant microwave fields and a mechanical oscillator," Nature **495**, 210–214 (2013).

[112] M. Pechal, P. Arrangoiz-Arriola, and A. H. Safavi-Naeini, "Superconducting circuit quantum computing with nanomechanical resonators as storage," Quantum Sci. Technol. **4**, 015006 (2018).

[113] Q. P. Unterreithmeier, E. M. Weig, and J. P. Kotthaus, "Universal transduction scheme for nanomechanical systems based on dielectric forces," Nature **458**, 1001–1004 (2009).

[114] P. N. Kambali, G. Swain, A. K. Pandey, E. Buks, and O. Gottlieb, "Coupling and tuning of modal frequencies in direct current biased microelectromechanical systems arrays," Appl. Phys. Lett. **107**, 063104 (2015).

[115] S. Timoshenko, *Vibration problems in engineering* (D. Van Nostrand Company, Inc., New York, 1937).

[116] F. J. Hocke, *Microwave circuit-electromechanics in a nanomechanical hybrid system*, Ph.D. thesis, Walther-Meißner-Institut and Technische Universität München (2013).

[117] K. D. Sattler, ed., *Handbook of nanophysics: Functional nanomaterials* (CRC Press Taylor & Francis Group, Boca Raton, 2011).

[118] M. Pernpeintner, *Nanomechanical hybrid systems*, Ph.D. thesis, Walther-Meißner-Institut and Technische Universität München (2016).

[119] S. S. Verbridge, J. M. Parpia, R. B. Reichenbach, L. M. Bellan, and H. G. Craighead, "High quality factor resonance at room temperature with nanostrings under high tensile stress," J. Appl. Phys. **99**, 124304 (2006).

[120] A. N. Cleland, *Foundations of Nanomechanics*, Advanced Texts in Physics (Springer, Berlin, Heidelberg, 2003).

[121] L. Boltzmann, "Einige allgemeine Sätze über Wärmegleichgewicht," Wiener Berichte **63**, 679 (1871).

[122] P. R. Saulson, "Thermal noise in mechanical experiments," Phys. Rev. D **42**, 2437–2445 (1990).

[123] M. L. Gorodetsky, A. Schliesser, G. Anetsberger, S. Deleglise, and T. J. Kippenberg, "Determination of the vacuum optomechanical coupling rate using frequency noise calibration," Opt. Express **18**, 23236 (2010).

[124] J. B. Marion and S. T. Thornton, *Classical dynamics of particles and systems* (Academic Press, 1965) p. 576.

[125] G. Strang, *Introduction to Linear Algebra*, 5th ed. (Wellesley-Cambridge Press, 2016) p. 574.

[126] Y. Saad, *Numerical methods for large eigenvalue problems* (Society for Industrial and Applied Mathematics, Philadelphia, 2011) p. 276.

[127] L. Landau, "Zur Theorie der Energieübertragung bei Stössen II," Phys. Z. Sowjetunion **2**, 46–51 (1932).

[128] C. Zener, "Non-Adiabatic Crossing of Energy Levels," Proc. R. Soc. A Math. Phys. Eng. Sci. **137**, 696–702 (1932).

[129] H. J. Maris and Q. Xiong, "Adiabatic and nonadiabatic processes in classical and quantum mechanics," Am. J. Phys. **56**, 1114–1117 (1988).

[130] B. W. Shore, M. V. Gromovyy, L. P. Yatsenko, and V. I. Romanenko, "Simple mechanical analogs of rapid adiabatic passage in atomic physics," Am. J. Phys. **77**, 1183–1194 (2009).

[131] H. Fu, Z.-c. Gong, T.-h. Mao, C.-p. Sun, S. Yi, Y. Li, and G.-y. Cao, "Classical analog of Stückelberg interferometry in a two-coupled-cantilever–based optomechanical system," Phys. Rev. A **94**, 043855 (2016).

[132] S. Brundobler and V. Elser, "S-matrix for generalized Landau-Zener problem," J. Phys. A. Math. Gen. **26**, 1211–1227 (1993).

[133] M. Born and V. Fock, "Beweis des Adiabatensatzes," Zeitschrift für Phys. **51**, 165–180 (1928).

[134] T. Kato, "On the Adiabatic Theorem of Quantum Mechanics," J. Phys. Soc. Japan **5**, 435–439 (1950).

[135] J. R. Rubbmark, M. M. Kash, M. G. Littman, and D. Kleppner, "Dynamical effects at avoided level crossings: A study of the Landau-Zener effect using Rydberg atoms," Phys. Rev. A **23**, 3107–3117 (1981).

[136] M. Sillanpää, T. Lehtinen, A. Paila, Y. Makhlin, and P. Hakonen, "Continuous-Time Monitoring of Landau-Zener Interference in a Cooper-Pair Box," Phys. Rev. Lett. **96**, 187002 (2006).

[137] J. R. Petta, H. Lu, and A. C. Gossard, "A Coherent Beam Splitter for Electronic Spin States," Science **327**, 669–672 (2010).

[138] G. D. Fuchs, G. Burkard, P. V. Klimov, and D. D. Awschalom, "A quantum memory intrinsic to single nitrogen–vacancy centres in diamond," Nat. Phys. **7**, 789–793 (2011).

[139] C. E. Carroll and F. T. Hioe, "Generalisation of the Landau-Zener calculation to three levels," J. Phys. A Math. Gen. **19**, 1151–1161 (1986).

[140] W. Demtröder, *Experimentalphysik 1 Mechanik und Wärme* (Springer, Berlin Heidelberg, 2015).

[141] G. Duffing, *Erzwungene Schwingungen bei veränderlicher Eigenfrequenz und ihre technische Bedeutung* (Friedr. Vieweg und Sohn, Braunschweig, 1918).

[142] A. H. Nayfeh and D. T. Mook, *Nonlinear Oscillations*, Pure and Applied Mathematics: A Wiley Series of Texts, Monographs and Tracts (Wiley, New York, 1979).

[143] G. Radons, B. Rumpf, and H. G. Schuster, *Nonlinear Dyn. Nanosyst.* (John Wiley & Sons, New York, 2010) p. 455.

[144] S. S. Verbridge, H. G. Craighead, and J. M. Parpia, "A megahertz nanomechanical resonator with room temperature quality factor over a million," Appl. Phys. Lett. **92**, 013112 (2008).

[145] K. J. Lulla, R. B. Cousins, A. Venkatesan, M. J. Patton, A. D. Armour, C. J. Mellor, and J. R. Owers-Bradley, "Nonlinear modal coupling in a high-stress doubly-clamped nanomechanical resonator," New J. Phys. **14**, 113040 (2012).

[146] A. Faltermeier, "Umbau eines Freistrahlinterferometers zur Charakterisierung nanomechanischer Saiten," Bachelor's thesis, Walther-Meißner-Institut Tech. Univ. München (2017).

[147] Q. P. Unterreithmeier, T. Faust, and J. P. Kotthaus, "Damping of Nanomechanical Resonators," Phys. Rev. Lett. **105**, 027205 (2010).

[148] Q. P. Unterreithmeier, S. Manus, and J. P. Kotthaus, "Coherent detection of nonlinear nanomechanical motion using a stroboscopic downconversion technique," Appl. Phys. Lett. **94**, 263104 (2009).

[149] R. Schutjens, F. A. Dagga, D. J. Egger, and F. K. Wilhelm, "Single-qubit gates in frequency-crowded transmon systems," Phys. Rev. A **88**, 052330 (2013).

[150] C. Dong, V. Fiore, M. C. Kuzyk, and H. Wang, "Optomechanical Dark Mode," Science **338**, 1609–1613 (2012).

[151] Y.-D. Wang and A. A. Clerk, "Using dark modes for high-fidelity optomechanical quantum state transfer," New J. Phys. **14**, 105010 (2012).

[152] L. Tian, "Adiabatic State Conversion and Pulse Transmission in Optomechanical Systems," Phys. Rev. Lett. **108**, 153604 (2012).

[153] S. E. Harris, "Electromagnetically Induced Transparency," Phys. Today **50**, 36–42 (1997).

[154] S. Weis, R. Rivière, S. Deléglise, E. Gavartin, O. Arcizet, A. Schliesser, and T. J. Kippenberg, "Optomechanically induced transparency." Science **330**, 1520–3 (2010).

[155] E. Arimondo, "Coherent Population Trapping in Laser Spectroscopy," Prog. Opt. **35**, 257–354 (1996).

[156] A. H. Ghadimi, D. J. Wilson, and T. J. Kippenberg, "Radiation and Internal Loss Engineering of High-Stress Silicon Nitride Nanobeams," Nano Lett. **17**, 3501–3505 (2017).

[157] Y. Tsaturyan, A. Barg, E. S. Polzik, and A. Schliesser, "Ultracoherent nanomechanical resonators via soft clamping and dissipation dilution," Nat. Nanotechnol. **12**, 776–783 (2017).

[158] N. V. Vitanov, A. A. Rangelov, B. W. Shore, and K. Bergmann, "Stimulated Raman adiabatic passage in physics, chemistry, and beyond," Rev. Mod. Phys. **89**, 015006 (2017).

[159] J. H. Cole, A. D. Greentree, L. C. L. Hollenberg, and S. Das Sarma, "Spatial adiabatic passage in a realistic triple well structure," Phys. Rev. B **77**, 235418 (2008).

[160] R. Rahman, R. P. Muller, J. E. Levy, M. S. Carroll, G. Klimeck, A. D. Greentree, and L. C. L. Hollenberg, "Coherent electron transport by adiabatic passage in an imperfect donor chain," Phys. Rev. B **82**, 155315 (2010).

[161] S. Nikitov, P. Tailhades, and C. Tsai, "Spin waves in periodic magnetic structures—magnonic crystals," J. Magn. Magn. Mater. **236**, 320–330 (2001).

[162] Z. K. Wang, V. L. Zhang, H. S. Lim, S. C. Ng, M. H. Kuok, S. Jain, and A. O. Adeyeye, "Observation of frequency band gaps in a one-dimensional nanostructured magnonic crystal," Appl. Phys. Lett. **94**, 083112 (2009).

[163] S. Tacchi, G. Duerr, J. W. Klos, M. Madami, S. Neusser, G. Gubbiotti, G. Carlotti, M. Krawczyk, and D. Grundler, "Forbidden Band Gaps in the Spin-Wave Spectrum of a Two-Dimensional Bicomponent Magnonic Crystal," Phys. Rev. Lett. **109**, 137202 (2012).

[164] M. Krawczyk and D. Grundler, "Review and prospects of magnonic crystals and devices with reprogrammable band structure," J. Phys. Condens. Matter **26**, 123202 (2014).

Acknowledgments

I am grateful to everyone who contributed to the completion of this thesis and who supported me during the last year. In particular, I want to thank:

Prof. Dr. Rudolf Gross, for granting me the opportunity to perform this work at the Walther-Meißner-Institut.
Dr. Hans Hübl, for supervising this thesis, introducing me to the interesting field of nanomechanics and constantly providing me with support and ideas. I am also grateful for his kind and approachable attitude during his lectures, which founded my motivation to work at the WMI.
Daniel Schwienbacher, for being a kind and supportive advisor, for sharing with me his knowledge of optics, nanomechanics and thin film fabrication, for being available whenever needed and for his advise during the writing process.
Lukas Liensberger, for his patient support regarding the FMR and BLS setups, for countless lunchs, coffee breaks and barbecues. I greatly enjoyed working with you.
Sebastian Kammerer, for his crucial assistance with the delicate wet-etching process.
Dr. Mathias Weiler, for sharing his knowledge in the field of magnetoelastics and providing valuable ideas for measurements.
Dr. Natalie Segercrantz, for sharing with me the woes of nanofabrication, for brightening countless hours of lift-off in the cleanroom with interesting conversations and for teaching me a thing or two about scientific writing.
Thomas Brenninger and Sebastian Kammerer, for maintaining the technical facilities at the WMI and keeping the inevitable downtimes to a minimum.
The (former) master students Lisa Rosenzweig, Luis Flacke, Birte Cöster, Michaela Schleuder, Michael Renger, Christian Besson, Christoph Utschick, Daniel Arweiler, Ulrike Zweck, Mingxing Xu and Mohammad T. Amawi, for creating a friendly and enjoyable atmosphere as well as plenty of memorable moments.
All the other Postdocs and PhD students at the WMI, for providing support and advice whenever needed.
Everyone at the WMI, for creating a pleasant and collegial working atmosphere.

Lastly, I want to thank my family, for the support during my studies, and my friends, for their unrelenting efforts to establish a hint of work-life-balance.